THE UNIVERSITY OF CHICAGO

IONIC AND MOLECULAR TRANSPORT IN 2D MATERIAL MEMBRANES

A DISSERTATION SUBMITTED TO
THE FACULTY OF THE PRITZKER SCHOOL OF MOLECULAR ENGINEERING
IN CANDIDACY FOR THE DEGREE OF
DOCTOR OF PHILOSOPHY

BY
ELI HOENIG

CHICAGO, ILLINOIS
DECEMBER 2023

Copyright © 2023 by Eli Hoenig

All Rights Reserved

To my parents, Cathy and Peter.

TABLE OF CONTENTS

LIST OF FIGURES

LIST OF TABLES

ACKNOWLEDGMENTS

At the center of my scientific project is Professor Chong Liu, who introduced me to materials science, who guided me through experiments, encouraged my ideas, and whose unfettered optimism and enthusiasm I will take with me. Speical thanks also goes to my thesis committee: Professor Giulia Galli, Professor Paul Nealey, and Professor Emeritus James Skinner.

My lab-mates are integral to this project. Special thanks goes to Dr. Mingzhan Wang, who is the only person to precede me in lab, and who has listened to and advised me on countless ideas, even if half-baked; to Grant Hill and Adarsh Suresh, my peers from the beginning; and to Yu Han, for spending too many hours collecting STEM data with me at such strange hours. But I am indebted to all my fellow researchers I've worked with over the past five years, including: Gangbin Yan, Siqi Zou, Dongchen Ying, Julia Radhakrishnan, Martin Ayala, Jon Shao, Dr. Guiming Peng, Dr. Steven Strong, Professor Nestor Zaluzec, Wendy Chen, Thomas Manchese and Dr. Bing Han.

Without tools, I would have no data and without data this thesis would be completely made up. Thankfully, it's not, and for that I have to thank Justin Jureller, Sarah Brown, Gerard Olack, Qiti Guo, Yimei Chen and Fengyuan Shi for maintaining the many instruments I've used in the past five years.

But so far I've just mentioned those people who have helped my science directly. Let's go a little farther out. Of course there's Bowers house; all but one (Phil!) of my good friends in Chicago reside(d) there. And these friends, I must say, are very good. So much of the richness, variation and tastiness in my life I attribute to them.

Finally there's my family: Isaac, Talia, Cathy, Peter and Rania. They are the reason I am able to do anything at all, let alone this project.

ABSTRACT

Two dimensional materials represent a new class of membranes for water-ion and ion-ion separations. With careful tuning, two-dimensional materials can form the basis of highly selective and efficient membranes for water decontamination, energy generation and even biological sensing. Nanofluidic devices made from two-dimensional materials are also excellent testing grounds for complex models of interfacial water structure and confined ionic and molecular transport; they have led to striking advances in our understanding of solid-liquid interactions. Here we present two new devices, based on the two-dimensional material molybdenum disulfide (MoS_2), that allow us to achieve Å-scale control of ionic and molecular transport. We both demonstrate that MoS_2 membranes are practical ionic and molecular sieves, as well as reveal new transport phenomena for aqueous systems under nanometer-scale confinement.

We divide our work into four chapters: in **Chapter 2**, we present a method to control the interlayer spacing of layered MoS_2 membranes. By covalently functionalizing MoS_2 monolayers with small molecular pillars, we expand the height of the interlayer gallery from effectively 0 to ~ 0.6 Å. We show how not only the size but also the chemistry of the functional group determines membrane structure. In **Chapter 3**, we show how these films can be used to sieve ions from water, and even one ion from another. Using molecular dynamics simulations, we reveal the effect of water layering on the structure of the membranes. In **Chapter 4**, we present a new procedure for the fabrication (sub)nm pores in few-layer MoS_2 membranes *in situ*. We find that the grain-boundaries in polycrystalline films are excellent nucleation points for electrochemical pore creation. Finally, in **Chapter 5**, we show how these pores act as ionic sieves, and can differentiate not only monovalent from divalent ions, but also monovalent ions from other from monovalent ions. By comparing transport measurements to molecular dynamics simulations, we show how water dynamics, along with other factors, underlie the separation mechanism.

CHAPTER 1

2D MATERIALS FOR NANOFLUIDICS: UNPRECEDENTED CONTROL OF IONIC AND MOLECULAR TRANSPORT

1.1 Introduction to 2D material membranes

The separation of one component of a mixture from all other components in the same mixture is the backbone of countless biological processes, fundamental scientific experiments and industrial processes. Often, the most efficient method of separation lies in the use of membranes [1], thin films separating the effluent from permeate or one reservoir from another. The lipid bilayer membrane, which can host various selective elements such as the potassium ion channel, is one example of such a membrane [2]. As are polyamide films for industrial-scale desalination [3], and Nafion, a proton-selective polymer used for hydrogen fuel cells [4]. The inner workings of these membranes are complex and often highly tailored to their specific application. Despite great advances in electron microscopy, x-ray diffraction and other relevant experimental techniques, new discoveries about the inner workings of selective membranes are still being uncovered and mysteries remain [5].

Two-dimensional (2D) materials, such as graphene, hexagonal boron nitride (hBN) and molybdenum disulfide (MoS_2) are a new class of materials with unique electronic and exceptional mechanical properties [6–9]. Specifically, the strength of their in-plane bonds means that a one (or a few, depending on the crystal) atom thick layer can be suspended in μm-scale free-space without tearing [10]. We are able to freely manipulate these atomically thin materials, allowing us to make structures with Å-scale features with simple tools: we can stack, twist [11], suspend, etch [12]. We can form structures with Å-scale gaps [13], or membranes with $<$1 nm pores [14]. We can even form stacks of different types of 2D materials with arbitrary rotational offsets [15].

This flexibility allows us to fabricate membranes with unprecedented precision and with

well-defined, simple features. These synthetic, all solid-state membranes are, compared to their biological or polymer counterparts, far easier to model and understand, allowing us to isolate emergent phenomena inherent to atomic and molecular transport. Furthermore, we can design membranes from the ground up with features relevant for a specific application. From a clean starting point, we can add functional groups, tune channel height or pore diameter and modify surface charge. In this thesis, we demonstrate how 2D materials can be used to both understand fundamental properties of atomic and molecular transport, as well as serve as building blocks for the fabrication of a new class of membranes.

1.2 Classes of 2D material membranes

2D materials are versatile and precise building blocks for the fabrication of nanometer-scale devices, and have enabled the fabrication of fluidic channels and membranes with unprecedented control. To date, a variety of devices have been fabricated, some of which are excellent testing grounds for fundamental studies, and others are more geared towards practical applications. These devices can be divided into four categories: nanoslits[13], nanopores[16], nanotubes[17] and layered membranes [18].

Although we list the four categories of 2D material-based nanofluidic devices below, there are generally only two types of geometries: 1D (nanotubes and nanopores) and 2D confinement (nanoslits and layered membranes), see Fig. 1.1. Although properties of fluids and dissolved species will vary based on the confining material chemistry and channel dimensions, we are able to outline, in broad strokes, particular characteristics of confined fluids within each category. We note that the terms 1D and 2D confinement are hyperbole; in the same sense that 2D materials are not truly 2D and have finite thickness; nanochannels are not 2D, and have finite height. Here, a 2D confined geometry implies that the length-scale of the confining dimension is on the order of the transporting species, and that net flux can occur only in two dimensions. A 1D confined geometry implies that the length-scale of the

two confining dimensions are on the order of the transporting species, and net flux can occur only in *one* dimension.

The characteristic property of water confined to 2D slits is *water layering and ordering*. In bulk isotropic systems, water has no preferred orientation; although there is an intricate hydrogen bonding network, the orientation of one water molecule far away (usually only ∼1 nm) from another is random. Under 2D confinement, we introduce strict boundaries, breaking the system symmetry. If, for example, the walls have a slight negative charge, the oxygen atoms face away from the edge of the channel. Due to this increased ordering, the water density obtains a defined layered structure (see Section 3.4). Under the strictest possible 2D confinement, wherein only a single water layer is formed, exotic phases of water structure should emerge, from "square ice" to hexatic and, at high pressure and temperature, even disordered superionic phases [19]. Some direct evidence for square ice exists in graphene systems[20], but this result has as yet not been reproduced. In real systems, such as layered membranes, the structure of water exerts an influence back on the confining material, an effect which is rarely included in modelling studies. In our work, we find that this feedback has a large influence on the structure of the 2D membrane, and describe in detail its effects (see Section 3.4).

The transport of ions is also uniquely effected by 2D confinement, as first documented by Esfandiar *et al.*[13]. The first order effect of 2D confinement on ion transport is a simple hydration energy dependence on ion permeation. The hydration shell of an ion entering a nanoscale channel must distort, sometimes even shedding water molecules[21]. Instead of a strict size-based cutoff, the degree of ion hindrance varies smoothly with the degree of distortion and the penalty of a given distortion. This picture is complicated by the recent discovery of ion-pairing in these nanochannels, where the transport of two oppositely charged ions are highly coupled. Further studies have found that even the preferred location within the 2D channel for a given ion (close or far from the the wall) has a dramatic effect on its

transport behavior[22, 23].

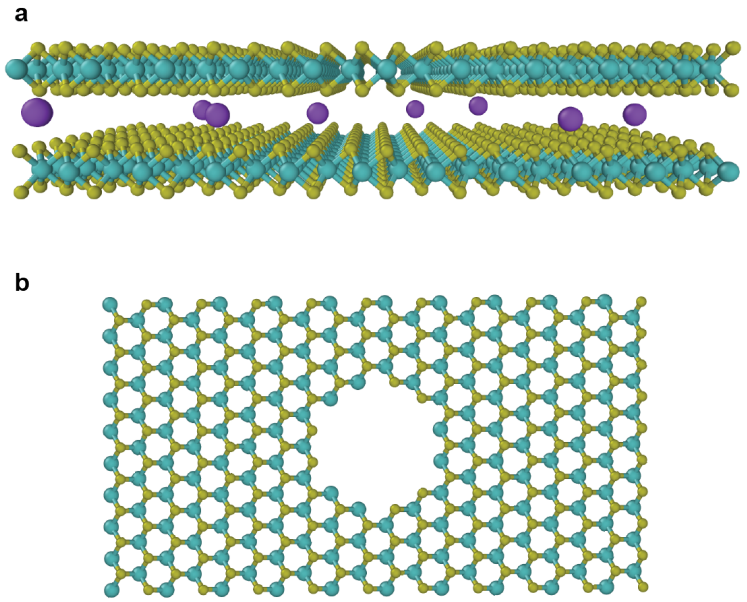

Figure 1.1: Two types of confinement with 2D materials are possible: 2D (**a**) and 1D (**b**). In these images, both materials are MoS_2, the 2D material used in this thesis.

Water confined to 1D channels displays markedly different behavior than that in 2D channels. Although we see a similar, albeit here a *radial*, layering phenomenon when the pore diameter is large enough to accommodate several water molecules (see e.g. Fig. 5.14), the additional dimension of constraint leads to unique behavior [5]. In sub-nm carbon nanotubes, for example, a single file of water forms spontaneously [24, 25]. The hydrogen bonding within this chain is longer-lasting than its bulk counter-part, leading to ultrafast burst-like transport. Various exotic phases have been observed in nanopores, but the complete picture is yet to be developed. This is partially due to a drastic dependence on channel dimensions: for example, dramatic and non-monotoic changes in melting temperatures for water confined to carbon nanotubes were observed for relatively small (1 nm to 1.5 nm) changes in diameter [26].

The structure of confined water has a dramatic effect on the transport of ions constrained to 1D channels. First, protons exhibit rapid diffusion due to an accelerated Grotthaus

mechanism in single-file water[25]. Larger ions, such as K^+ exhibit non-Nernstian transport, due to clustering of water molecules under an applied bias [27]. The channel itself also has a dramatic effect on transport: cations are nearly universally favored in inorganic 1D channels, likely due to OH^{-1} adsorption on the channel wall, although the exact mechanism of this selectivity is not yet fully understood[28]. In this thesis, we find that the *dynamics* of water also has a dramatic effect on water transport confined to a quasi-1D geometry: the rate of hydration shell exchange has a pronounced effect on ion transport, compared to the bulk case[29].

Now we describe the four types of 2D material nanofluidic devices, alluded to above. **Nanoslits** are fabricated by stacking isolated multilayer crystals one on top of another, with monolayer spacers in-between[30]. These spacers separate the bulk crystals from each other, introducing nm or even Å-scale quasi-2D gaps. With careful wetting procedures, liquids (usually aqueous electrolytes) can be introduced into these gaps. The "size effect", wherein the degree of distorion of the hydration shell on entering the nanoslit determines its flux[13], was first discovered in these channels. Other effects, such as ion pairing and memory have also been explored [23].

Nanopores in 2D membranes can be introduced *via* a variety of methods, listed in detail in Section 5.1. As pores in the <1 nm range can be fabricated in ultrathin membranes [14], they can be used not only to study ion and molecular transport behavior, but also promise excellent performance as next-generation molecular sieves.

Nanotubes are some of the earliest devices fabricated for nanofluidic applications, and have continued to serve as excellent scientific testing grounds. Exotic phenomena such as single file water transport, quantum-mechanical coupling and water-cluster mediated ion transport all occur in these systems[17, 24, 27, 31, 32]. The most common fabrication protocols for making nanotube devices involves incorporating single carbon nanotubes into lipid-bilayer membranes or at then end of glass capillaries, but larger-scale devices can also

be made with carbon nanotube membranes[33]. The ionic or molecular flux can then be monitored *via* cell fluorescence, through optical spectroscopy or, in the case of large-scale membranes, through changes in bulk conductance of the permeate.

Layered 2D material membranes are perhaps the most scalable and practical 2D material devices. The synthesis involves liquid-exfoliation of bulk crystals and self-assembly, and is detailed (for MoS_2 membranes) in Section 2.5; procedures using other materials, such as graphene oxide, are similar[34]. By introducing foreign species between the layers (in this work, we covalently functionalize MoS_2 with small organic molecules), the spacing between layers is easily tuned [35, 36]. The membranes can then be used as sensitive probes of molecular transport under confinement, or as novel desalination membranes.

1.3 Ionic and molecular transport under nanoscale confinement

The properties of a transporting species varies significantly based on the dimensions of its confining geometry. Therefore we include here an outline of the properties of ions and molecules at the range of length-scales relevant for this thesis. These scales will be referred to in future sections when we rationalize membrane design choices and make physical interpretations of transport phenomena.

The effects of confinement begin emerging at length scales less than the **Debye length**, $\lambda_D = \sqrt{\frac{\epsilon_0 \epsilon_r k_B T}{2e^2 N_A I}}$ of an electrolyte, where ϵ_0 is the permittivity of vacuum, ϵ_r is the relative permittivity, k_B is Boltzmann's constant, e is the electron charge, N_A is Avogadro's number, T is the temperature and I the ionic strength of the electrolyte. λ_D represents how far the electrostatic potential reaches into the electrolyte from a charged object, and at room temperature varies between 0.3 nm (at 1 M) and 300 nm (at $1 * 10^{-5}$ M) for monovalent salts. Therefore, for low concentrations, ions in channels as large as 500 nm feel the presence of the channel walls, and can no longer be considered "in the bulk".

For most electrolytes in the bulk or in $\mathcal{O}$(100 nm) channels, ions can be treated as

independent and isolated point charges, each interacting with a uniform solvent and, electrostatically, with channel walls. Oppositely charged ions began to interact with *each other*, however, when the distance between them is within the **Bjerrum length**, $l_B = \frac{e^2}{4\pi\epsilon_0\epsilon_r k_B T}$. In bulk water $l_B = 0.7$ nm, meaning ions rarely interact. The expression for l_B changes with the system geometry, however: it's value increases dramatically under confinement [23], making ion pairing, or ion-ion correlations, a key feature of transport in nanometer-scale slits and pores.

As we squeeze electrolytes into ever smaller channels, classical mean-field models, such as the Poisson-Nernst-Planck model detailed in Section 5.4.1, begin to break down, and the discrete nature of ions and solvent molecules become all-important. The first and second **hydration shells** of common monovalent and divalent ions have radii ranging from $0.4 - 0.54$ nm and 0.83 - 0.96, respectively [29]. When they are confined to channels of commensurate size, the finite size of hydrated ions, and even the shape and flexibility of their solvation shells, must be considered for an accurate model of transport [37].

It is not only the ions, however, that we have to model explicitly at these length scales: the solvent itself (in this thesis always water), feels the effect of channel walls. The **correlation length** of water (which itself varies under confinement) is $\sim$1 nm, meaning that one water molecule is influenced by another less than 1 nm away [38]. Water, therefore, takes on various exotic structures when confined to channels of 1 nm. Depending on the geometry of confinement and the molecular properties of the channel wall, these structures can be highly disordered to rigid "square ice"[17, 19]. Clearly, the arrangement of the solvent has a dramatic effect both on its own dynamics, as well as the transport of any dissolved species.

1.4 Modelling ion and water transport at the nanometer scale

The transport of ionic and molecular species is modelled predominantly with three methods, depending on the length and time scales of interest. As always, there is an intrinsic trade-off

between fidelity and computational cost. The coarsest grained method of simulation involves continuum, or mean-field methods using finite element simulations[39]. In these simulations, the geometry is divided into a mesh, over which the set of differential equations forming the **Poisson-Nernst-Planck (PNP)** model are solved. We present the formulation of this model in Section 5.4.1. Although, in its most basic form, the PNP model cannot capture molecular-level effects, such as from the finite size of ions or the distortion of the hydration shell, it does an excellent job capturing dynamics and equilibrium configurations at the 10-100 nm scale. Furthermore, it can be used as a baseline case with which more detailed models can be compared. Due to its relatively low complexity, it is straightforward to test a wide range of parameters and configurations for a given system, a task which is strenuous for molecular-level models.

Various extensions to the PNP model have been developed that add phenomenological terms to take into account such effects as ion-ion correlations and finite size effects [39, 40]. These extensions to the PNP model have been successful, and have predicted features of confined ion transport in, for example, layered graphene membranes [41].

Continuum models are fundamentally limited when the molecular-level details of a system cannot be easily related to bulk properties. A single hydrated ion may occupy a $<$1 nm pore, for example, changing the local electrostatic environment. The details of ion solvation, and water structure at interfaces cannot be captured even with extended PNP methodologies. In classical **Molecular dynamics (MD) simulations**, Newton's equations of motion are solved step-wise for every atom, which are explicitly defined. Atom-atom interactions are determined by a predefined, often 12-6 (Lennard-Jones), potential. Long range forces, such as electrostatic interactions, are often incorporated as well, although are slightly more difficult to model due to the exponentially increasing number of atoms that effect and are effected by the atom of interest. As such, tricks such as the particle-particle-particle mesh method are employed.

Classical MD simulations are the most common method used to model nanofluidic systems, as they are computationally simple enough to allow for the ready simulation of systems up to ∼100 nm across, but capture atom-level structure and dynamics. Seminal findings, such as the spontaneous wetting of carbon nanotubes [24], ion pairing and memory in nanoslits[23], desalination in MoS_2 nanopores [42], and dehydration-determined ion selectivity in sub-nanopores [43] were all built upon classical MD simulations. In this thesis, we rely heavily upon classical MD to describe, for example, water-layering in MoS_2 channels, and ion selectivity in few-layer MoS_2 nanopores.

For the smallest scales and in specific systems, such as those in which there is chemical bonding or reactivity, quantum-mechanical effects become paramount and classical MD simulations are no longer sufficient. Furthermore, the classical equations of motion is a gross approximation, which may breakdown for unanticipated reasons in nanofluidic systems. **Ab-initio MD** begins to solve some of these issues by treating nuclei of atoms classically, but solves the Schrodinger equation at each time step to calculate electronic forces [5]. **Density functional theory (DFT)** and other more modern quantum mechanical techniques can also capture relevant phenomena for nanofluidic systems, although the system sizes are severely constrained due to computation requirements. For example, DFT is applied in our recent work to explicate the preferential adsorption of Cu^{2+} and Pb^{2+} in MoS_2 nanochannels [44]. For a comprehensive review of the quantum-mechanical-based simulation methods, see Aluru *et al.*[5].

1.5 Free-spacing and structure of multilayer MoS_2

There is some inconsistency in the literature regarding the "free-spacing" between bulk MoS_2 layers; some studies, for example, claim that there is 3 Åof "free space"[18], others that the interlayer gallery is filled with a dense electron cloud from the sulfur atoms [45]. It is important, therefore, to pinpoint the exact structure of bulk MoS_2, and thereby determine

what type of interlayer transport is or is not possible; this will in turn determine a baseline case, with which we can compare modified crystals, such as functionalized and restacked membranes.

Several phases of MoS_2 exist: trigonal prismatic 2H (AbA BaB), octahedral 1T (AbC AbC), and trigonal primsatic 3R (AbA CaC BcB)[46] (see Fig. 1.2). 2H phase is the most common form of MoS_2, and is found in CVD-grown and naturally sourced crystals. 1T phase has received growing interest in recent years due to its electronic (metallic) and chemical (negatively charged) properties. It is easily synthesized *via* lithiation and exfoliation. 3R phase MoS_2 is more thermally stable than 1T phase MoS_2, and is grown with flux-based methods around screw dislocations [47]. The interlayer separation (center Mo to center MO distance) for all phases of MoS_2 is 6.15 Å, although the measured value can vary slightly in the literature[48].

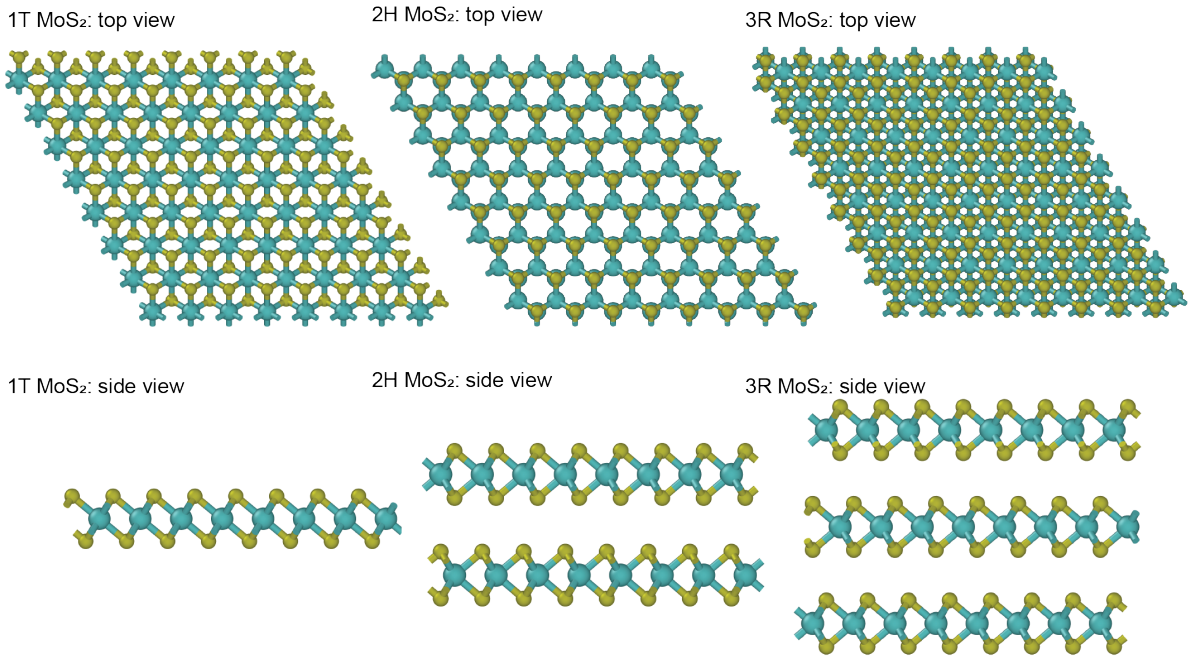

Figure 1.2: Structure of the three most common phases of MoS_2: 1T, 2H and 3R

To determine the "free spacing" we have to take into account the effective thickness of the MoS_2 sheet. The van der Waals radius of sulfur is 1.8 Å, and the center Mo-S distance

in the z-direction is 1.3 Å. The thickness of a single sheet is, therefore, 6.2 Å, nearly identical to the interlayer separation. The slight discrepancy arises from the close-packing structure of the layers (the S atoms do not stack vertically). This result is as it should be, given that there are no foreign species between layers, and the interlayer separation is *determined* by the layer thickness. When calculating "free spacing", modified membranes, e.g. those pillared with small organic molecules, we must subtract 6.15 Åfrom the interlayer separation, which is the quantity measured *via* x-ray diffraction or transmission electron microscopy.

Without severe mechanical transformations and large driving forces, no atomic, let alone molecular, species should be able permeate between layers. Recent studies have shown, however, that protons are able to enter and diffuse through the van der Waals gaps [45, 48], and quote the "free space" at 0.5 Å. This result is not applicable to the case of ions such as Li^+, as the protons bond with MoS_2 crystal, and diffuse *via* a site-hopping mechanism [49].

CHAPTER 2

CONTROLLING THE STRUCTURE OF RE-STACKED 2D MATERIAL MEMBRANES

2.1 Introduction

Restacked 2D materials, which are assemblies of individual atomically thin sheets with their basal planes lying parallel to each other, comprise a new class of nanofiltration membranes that show great promise as efficient separators of ions and small molecules from water. In a filtration device, water flows through the channels between layers of material with little obstruction, while ions and other small molecules are excluded (Fig. 2.1 a). Graphene and graphene oxide form the basis for the first molecular sieves [34, 50–57], but the breadth of constituent materials has grown in recent years to include, among others, boron nitride [58], MXenes [59, 60] and transition metal dichalcogenides (TMDs) such as WS_2 [61] and MoS_2 [62, 63]. Chemically exfoliated MoS_2 (ce-MoS_2) is a particularly viable candidate for reverse osmosis (RO) desalination, as exemplified in recent studies [18, 36, 64]. The channel width of restacked ce-MoS_2 is on the appropriate length scale for size-based exclusion of ions while facilitating high water flux; furthermore, recent studies have demonstrated that ce-MoS_2 is more structurally stable than its graphene oxide counterparts [18, 65, 66].

Recent efforts have demonstrated the viability of horizontally aligned ce-MoS_2 as an RO membrane [18, 36, 63, 64, 66]. Ries et al. and Hirunpinyopas et al. show that the surface hydrophilicity of MoS_2 membranes has a profound effect on its ion sieving properties [36, 64]. Wang et al. detail the stability of MoS_2 membranes and the relationship between the normalized water flux and applied pressure in a dead-end filtration setup [18].

The interplay of interlayer spacing and surface chemistry and their effects on water and ion transport remain unclear, however. To understand these effects, both single channels and the mesoporous structure of the channel assemblies need to be controlled precisely. The

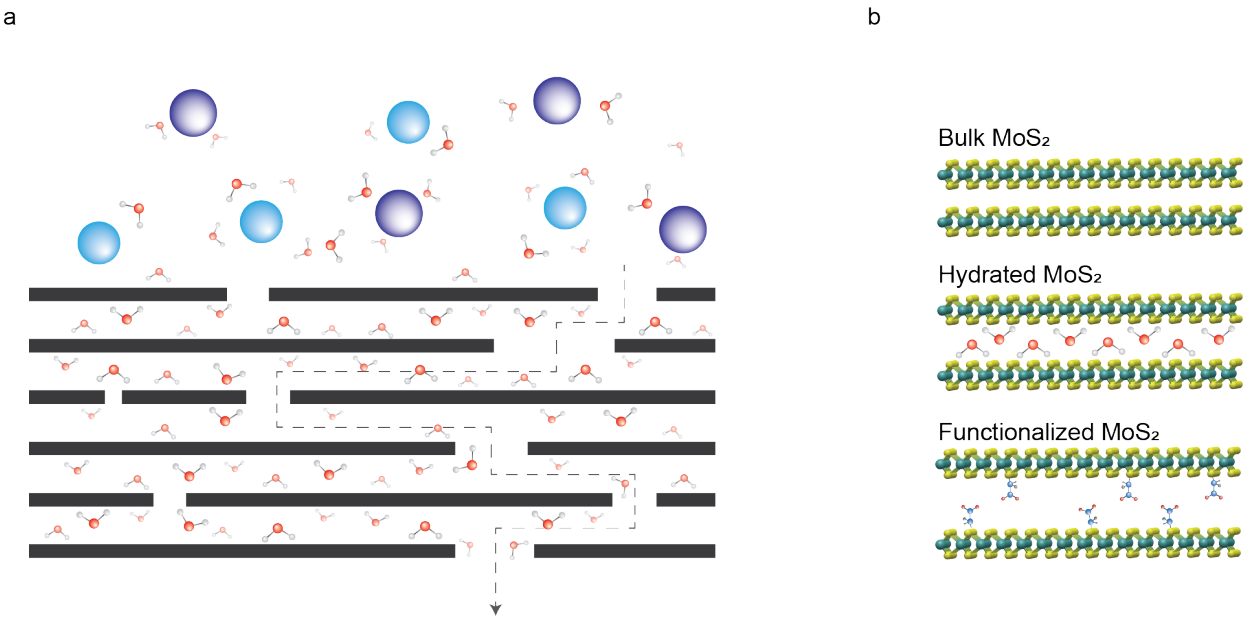

Figure 2.1: Schematic of layered membrane concept and pillaring strategies. **a**. Schematic showing restacked membrane infused with water in an electrolyte solution. Large ions and other molecules are not able to enter the film due to the small interlayer spacing, however water is able to permeate through following a tortuous path. **b**. Cartoon showing bulk, hydrated and functionalized MoS_2, with different interlayer separation that can be tailored to a specific application.

interlayer spacing of MoS_2 membranes can be controlled by varying the hydration degree of the membrane, or by introducing functional groups on the MoS_2 surface that operate as molecular pillars Fig. 2.1 b. Here, we functionalize MoS_2 with molecular spacers and, coupled with a drying and rehydration method, control the structure of MoS_2-based membranes on both the micro- and mesoporous scales. We find features on both length scales that vary with the hydration extent of the membrane and must be considered when rationalizing its filtration properties 2.2.

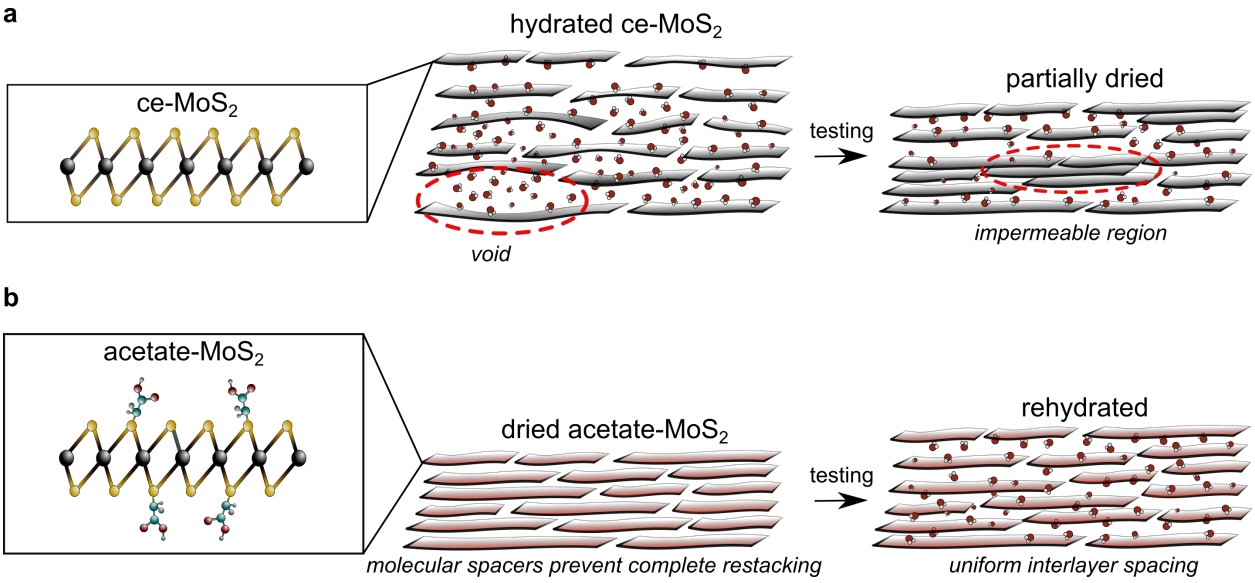

Figure 2.2: Schematic of the hydration-dependent structure of MoS_2 membranes. **a.** Initially, the hydrated ce-MoS_2 membrane is disordered with mesoporous scale voids between layers. When partially dried, the large voids close but parts of the membrane restack to the bulk, decreasing the overall porosity of the membrane (and when completely dried, the membrane is impermeable). **a.** Acetate-MoS_2 membranes dry without restacking to the impermeable bulk-like structure. This allows the membrane to rehydrate during testing, leading to consistent interlayer spacing with fewer voids or impermeable regions.

2.2 Synthesis and characterization of MoS_2 membranes: overview

An aqueous suspension, shown in Fig. 2.3 a, of ce-MoS_2 flakes is synthesized following the standard lithium-intercalation and exfoliation procedure [67–69] outlined in Section 2.5. MoS_2 flakes are characterized by atomic force microscopy (AFM) of drop cast samples

(Fig. 2.3 b) along with transmission electron microscopy (TEM), as shown in Fig. 2.3 c. The ce-MoS_2 flakes are 100 to 500 nm in lateral size and only a few nm in total thickness; these high aspect ratio mono- to few-layer flakes stack in a parallel configuration when vacuum filtered on a porous polymer substrate (mixed cellulose ester, 25 nm pore size) to form a uniform layered film (Fig. 2.3 d-e). These membranes are robust and flexible, and can withstand macroscopic bending (Fig. 2.3. The thickness can be controlled by the amount of solution filtered on the substrate but is typically 50 to 200 nm in this study. The flakes are generally 100–500 nm in lateral size and only a few nm in total thickness. Membranes are assembled via vacuum filtration on a porous polymer substrate (mixed cellulose ester, 25 nm average pore diameter) and dried for a given period to control the hydration extent.

We covalently functionalize ce-MoS_2 sheets with two small organic molecule precursors: iodoacetic acid and iodoacetamide. We follow the procedure provided in recent studies [70, 71] and outlined in Section 2.5 to graft acetic acid and acetamide molecules on MoS_2 flakes. The mechanisms underlying the covalent functionalization are outlined in Section 2.4. Importantly, the net negative surface charge of ce-MoS_2(˜0.25 electrons per Mo atom) [72] is neutralized during functionalization. Acetic acid, however, deprotonates in neutral pH and induces a net negative charge on the sheet of equal magnitude to that of ce-MoS_2; [70] the sheets remain neutral for amide-MoS_2.

The fraction of organic fragments decorating the MoS_2 surface is determined via X-ray photoelectron spectroscopy (XPS) of samples drop cast on Si wafers [36, 70, 71]. The degree of functionalization (functional group per Mo atom) is derived from the S 2p region 2.5 a as well as the C 1s region, and for amide-MoS_2 the N 1s region [67]. Using all three methods, the degree of functionalization is calculated to be 20–26 % for acetate-MoS_2 and 22–26% for amide-MoS_2 (Section 2.4). These results are well aligned with previous studies [71]. More evidence of the covalent nature of the S–C bond on functionalized MoS_2 is provided by attenuated total reflectance Fourier-transform infrared spectroscopy (FTIR)

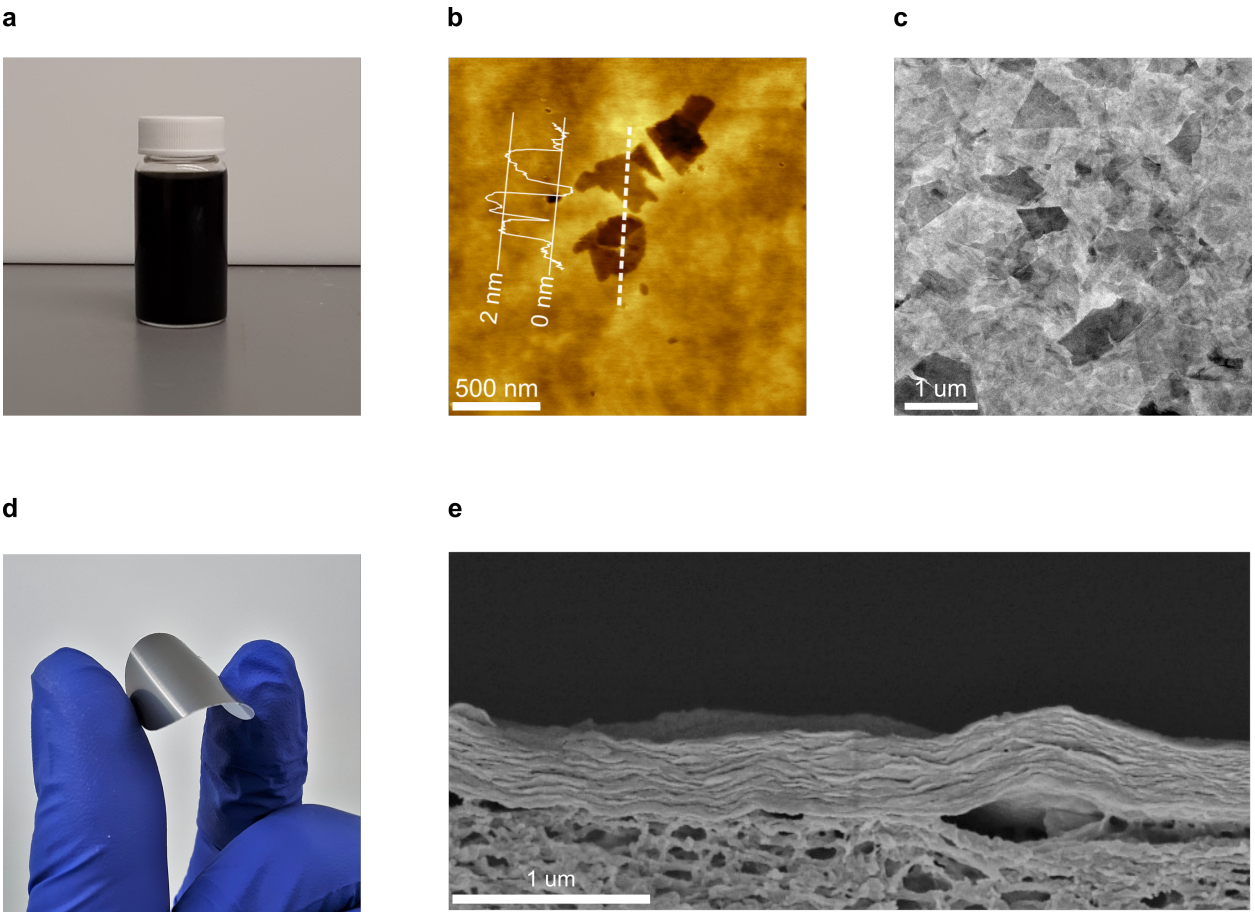

Figure 2.3: Characterization of ce-MoS_2 at various stages of synthesis. a, solution of suspended ce-MoS_2 flakes after lithium intercalation and exfoliation. Concentration is ~0.3 mg ml^{-1} **b**. AFM image of flakes drop cast on a Si wafer with height profile inset. The height profile indicates that these flakes are mono to bilayers. **c**. TEM of 10 nm thin ce-MoS_2 film, where individual flakes are identifiable. **d**. Macroscopic image of 100 nm ce-MoS_2 film. The dried film can be handled and bent without breaking. **e**. Cross-section SEM image of ce-MoS_2 membrane on a mixed cellulose ester substrate. Synthesis procedures are provided in Section 2.5.

spectra displayed in Fig. 2.5 b.

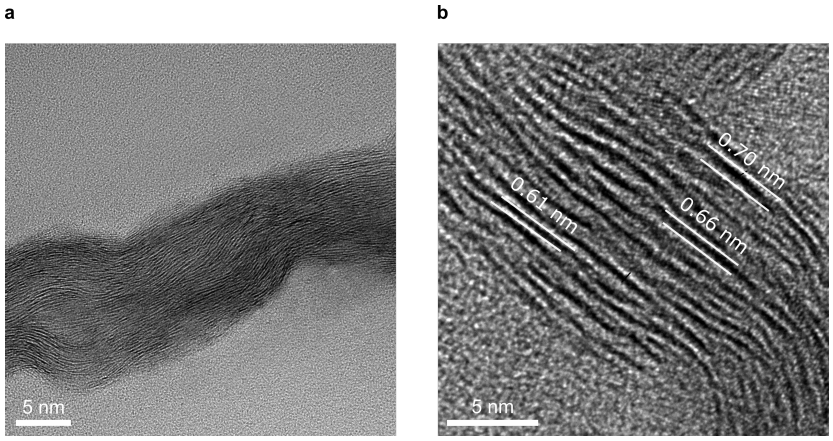

Figure 2.4: Cross-section TEM of ce-MoS_2. **a**. TEM cross-section of 20 nm thick ce-MoS_2 membrane showing clear evidence of laminar structure at the nanometer scale. **b**. TEM cross section of ce-MoS_2 membrane showing the interlayer separation roughly matching that of bulk MoS_2. The sample preparation procedure is presented in the Section 2.5.

The structure of MoS_2 membranes on the microporous scale is determined via a combination of XRD and TEM. The interlayer spacing as measured by XRD is 6.2 Å(bulk-like) for dried ce-MoS_2; as shown in Fig. 2.5 c, this value grows to 9.9 Åand 9.6 Åfor dried acetate- and amide-MoS_2, respectively. Flakes of acetate-MoS_2, characterized by TEM in Fig. 2.5 d, display similar morphology to and retain the hexagonal in-plane crystal structure of ce-MoS_2 ¬(diffraction pattern shown in inset). A result of this preservation, acetate-MoS_2 membranes have a similar layered structure to that of ce-MoS_2 membranes, only with an expanded interlayer spacing as shown in the TEM cross-section images in Fig. 2.5 e (see Methods for characterization details). When made into membranes, the flakes stack with their basal planes aligned but in random rotational orientations.

2.3 Hydration-dependent structure of MoS_2 membranes

Direct visualization of the hydrated MoS_2 membrane structure is accomplished using a standard freeze drying procedure, outlined in Section 2.5.3. This procedure allows direct mor-

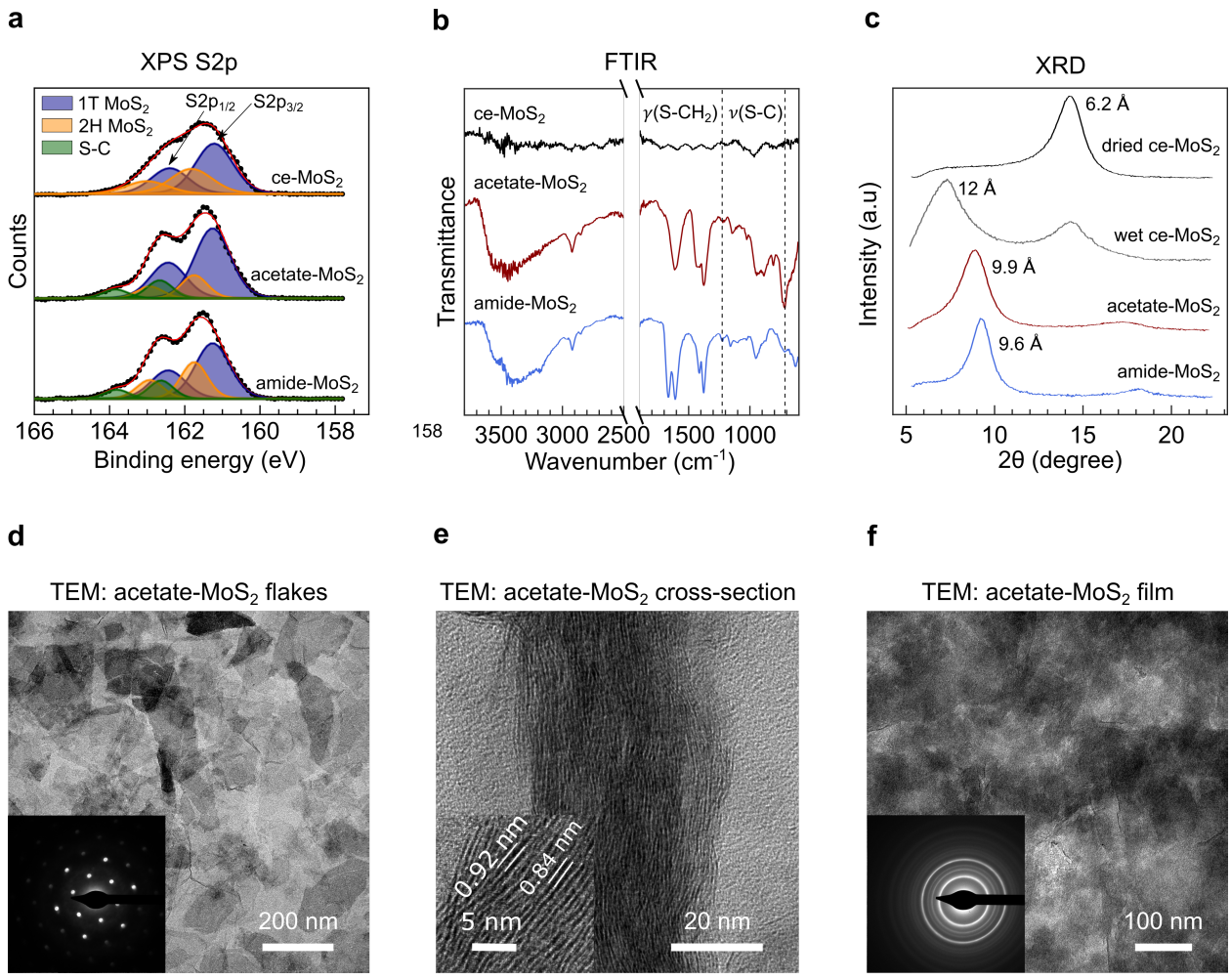

Figure 2.5: Characterization of functionalized MoS_2. **a**. XPS spectra of the S 2p region for ce-, acetate- and amide-MoS_2. The fraction of functional groups is computed by fitting the spectra with peaks from 1T and 2H MoS_2 phases as well as an S–C contribution. **b**. FTIR of MoS_2 samples showing the intramolecular acetate and acetamide stretches near 1500 $cm^{˘1}$, and S–CH_2 wagging peaks for acetate- and amide-MoS_2 at 1217 and 1225 cm^{-1}, respectively. Also evident are the S–C stretching peaks at ~715 $cm^{˘1}$. [71, 73]. **c**. XRD displaying the shift in interlayer spacing for dried functionalized MoS_2 and hydrated ce-MoS_2 relative to dried ce-MoS_2. **d**. Top-down TEM of acetate-MoS_2 flakes; the diffraction pattern for a single flake is inset, showing evidence of in-plane hexagonal symmetry. **e**. Cross-section TEM image of a 40 nm acetate-MoS_2 membrane. **f**. Top-down TEM image of a 50 nm acetate-MoS_2 membrane with the diffraction pattern inset, illustrating the random orientations of a thick composite flake stack.

phological comparison between dried ce-MoS_2 (Fig. 2.6 a), hydrated ce-MoS_2 (Fig. 2.6 b), and rehydrated acetate-MoS_2 (Fig. 2.6 c) on the mesoporous scale.

The membrane structure evident in SEM images is similar for rehydrated acetate-MoS_2 and dried ce-MoS_2 but differs for hydrated ce-MoS_2. In rehydrated acetate-MoS_2 and dried ce-MoS_2, the layers are regularly distributed whereas in hydrated ce-MoS_2, the layers are separated by mesoporous scale voids. The qualitative structure of these membranes is consistent throughout a given membrane and between membranes (Fig. 2.7.

We note that all images display similar qualitative structures: the variation between images provides the uncertainty in the void fraction profiles depicted by the shaded region in Fig. 2.6 d. The size of the voids in the MoS_2 membranes are quantified by thresholding the images in Fig. 2.7 at a constant greyscale value, tracing profiles normal to the plane of the MoS_2 membrane and measuring the peaks of the resulting square wave. The void height distribution is shown in Fig. 2.6; here, the curves represent the fraction of total void area for a given height (the resolution of the curve is limited by image pixel size). Each curve is calculated from 4 images with 1000 profiles each. As expected, hydrated ce-MoS_2 displays a broader peak at larger values (20 nm) compared to dried ce-MoS_2 and acetate-MoS_2 (10 nm). From this result, we conclude that with partial drying or surface functionalization and rehydration, the size of mesoporous scale voids can be greatly reduced.

The evolving mesoporous scale morphology is accompanied by evolving structure on the microporous scale. As shown in the XRD spectra in Fig. 2.6 e, in wet ce-MoS_2, two peaks are apparent corresponding to the bulk (6.2 Å) and hydrated (12 Å) interlayer spacings. As the membrane dries, the XRD peak corresponding to 12 Åinterlayer spacing decreases in intensity while the peak at 6.2 Åincreases. This evolution indicates irreversible stacking to bulk MoS_2. In contrast, no bulk peak (6.2 Å) is ever present in acetate-MoS_2 (Fig. 2.6 f) or amide-MoS_2 (Fig. 2.8; the singular channel width for acetate-MoS_2 simply shifts to smaller values as water leaves the membrane (from 11 Åto 9.9 Å).

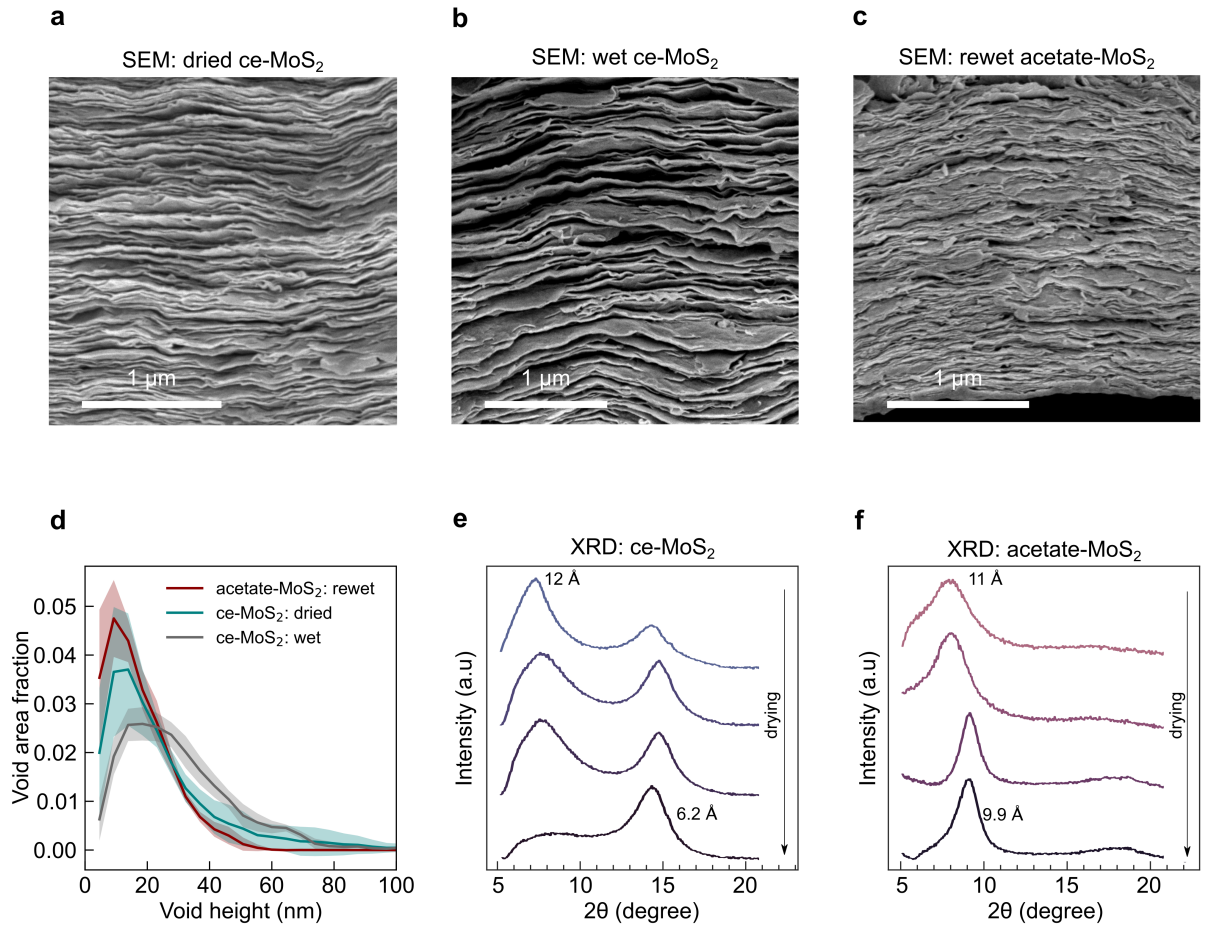

Figure 2.6: Characterization of membrane structure on the micro and mesoporous length scales. a, SEM cross-section of 3 μm thick dried ce-MoS_2 membrane displaying relatively small voids between layers. b, SEM cross-section of 3 μm freeze dried ce-MoS_2 membrane; relatively large gaps are visible between layers. c, SEM cross-section of 2 μm freeze dried acetate-MoS_2 membrane, dried then rehydrated. d, Quantification of void height distributions for a-c. The shaded region depicts the variability between images (shown in Fig. 2.7). e, XRD characterizing the hydration dependent structure of ce-MoS_2 on the microporous scale. As the membrane dries, the bilayer of water peak decreases in intensity, while the bulk-like peak rises. f, XRD characterizing the hydration dependent structure of acetate-MoS_2 on the microporous scale, where no bulk-like peak is evident.

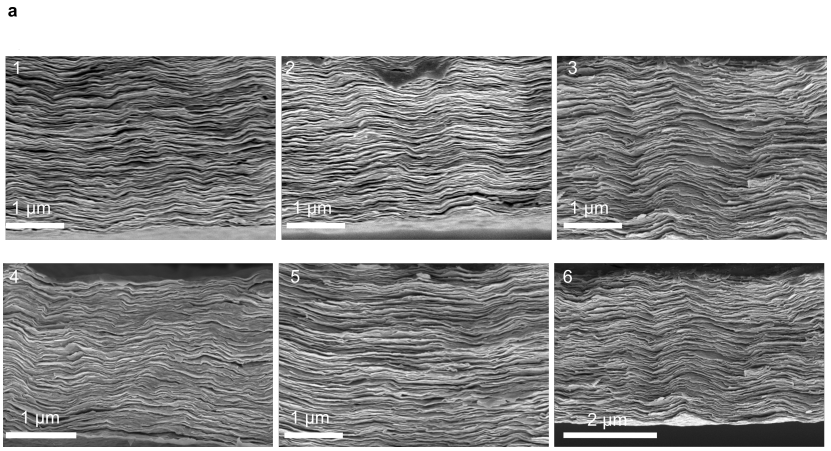

(a) Dried Ce-MoS_2

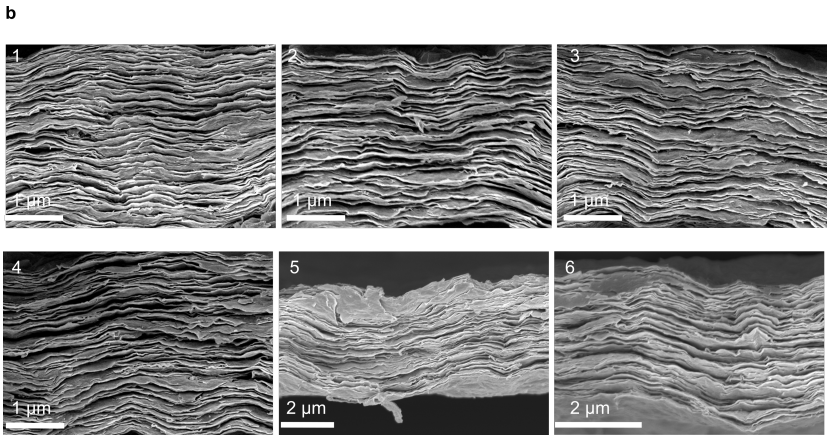

(b) Freeze-dried acetate-MoS_2

Figure 2.7: MoS_2 void characterization using SEM (continued on the next page).

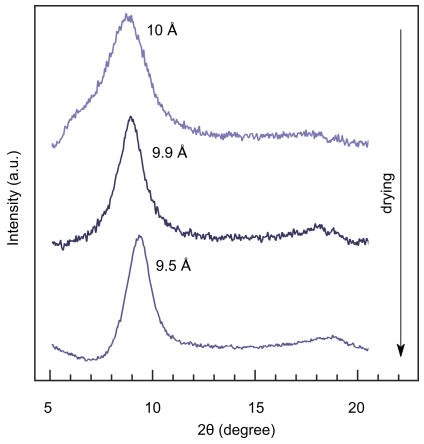

Figure 2.8: XRD characterizing the microporous structure of amide-MoS_2. No bulk ce-MoS_2 peak is visible. As the membrane dries the amide-MoS_2 peak shifts to slightly smaller interlayer separations, displaying similar behavior to that of acetate-MoS_2.

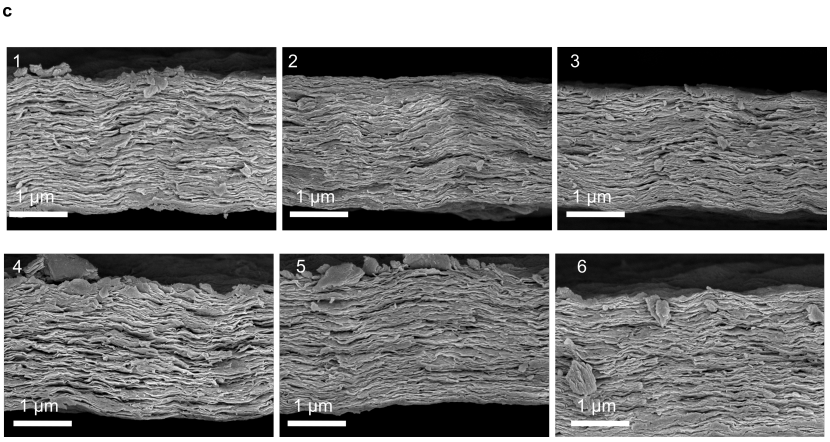

(a) Freeze-dried ce-MoS_2

Figure 2.8: (continued) MoS_2 void characterization using SEM. a, SEM cross-section of 3 μm dried MoS_2 membranes. Images from two membranes are shown: images 1-5 are taken at different points along the same membrane, and image 6 is from a separate sample. **b**, SEM cross section of 3 μm freeze dried MoS_2 membrane, showing images from two samples (images 1-4 and 5-6). c, SEM cross section of 2 μm acetate-MoS_2, all from different portions of the same membrane.

2.4 Functionalization and XPS analysis of MoS_2

During the lithium-intercalation and exfoliation process, lithium donates electrons to MoS_2. This electron transfer renders the MoS_2 net negatively charged with approximately 0.25 electrons per Mo atom[72]—it is this excess charge that allows ce-MoS_2 to be covalently functionalized. It also allows the flakes to remain suspended in solution (zeta potential -46(6) mV; see Table 2.2). The electrophilic organic fragments derived from organoiodide species share this excess charge to form C-S covalent bonds extruding from the MoS_2 surface. This neutralizes the net negative charge on the sheets; the surface charge is then controlled by the functional group. Acetic acid, which is deprotonated at neutral pH, induces a net negative charge on the sheet of equal magnitude to that of ce-MoS_2[70]. The sheet is neutral in the case of acetamide, but the polarity of the molecule allows the sheets to be suspended in aqueous solution[71].

Table 2.1: XPS fitting results. parameters for deconvolution of spectra in Fig. 2.5 and 2.9 Atomic percentages from S-C bonds for a given spectrum are summed to provide the degree of functionalization. Peak positions and widths are provided to increase reproducibility of these data.

Ce-MoS_2			
Component	Peak Position (eV)	FWHM (eV)	Atomic %
Mo 3d	-	-	-
1T $Mo3d_{5/2}$	228.32	0.57	23.5
1T $Mo3d_{3/2}$	231.47	0.66	15.7
2H $Mo3d_{5/2}$	228.85	1.05	36.6
2H $Mo3d_{3/2}$	232.11	1.22	24.1
S 2p			
1T $S2p_{1/2}$	161.22	1.18	42.5
1T $S2p_{3/2}$	162.4	1.18	21.7
2H $S2p_{1/2}$	161.82	1.33	23.7
2H $S2p_{3/2}$	163	1.33	12.1
Acetate-MoS_2			
Mo 3d			
1T $Mo3d_{5/2}$	228.41	0.71	30.1
1T $Mo3d_{3/2}$	231.51	0.71	19.8
2H $Mo3d_{5/2}$	228.84	1.09	30.1
2H $Mo3d_{3/2}$	232.18	1.09	20
S 2p			
1T $S2p_{1/2}$	161.26	1.11	46.3
1T $S2p_{3/2}$	162.44	1.11	23.6
2H $S2p_{1/2}$	161.75	0.82	11.4
2H $S2p_{3/2}$	162.93	0.82	5.8
S-C	162.67	0.8	8.6

Table 2.1 – continued from previous page

S-C	163.85	0.8	4.3
Amide-MoS_2			
Mo 3d			
1T $Mo3d_{5/2}$	228.44	0.67	27.3
1T $Mo3d_{3/2}$	231.54	0.67	18
2H $Mo3d_{5/2}$	228.88	1.11	32.9
2H $Mo3d_{3/2}$	232.17	1.11	21.7
S 2p			
1T $S2p_{1/2}$	161.26	1.08	38.2
1T $S2p_{3/2}$	162.44	1.08	19.5
2H $S2p_{1/2}$	161.75	0.83	19.3
2H $S2p_{3/2}$	162.93	0.83	9.9
S-C	162.63	0.77	8.8
S-C	163.81	0.77	4.4
N 1s			
Mo^{6+} $3p_{3/2}$	394.54	2.61	72.7
Mo^{4+} $3p_{3/2}$	397.33	1.81	6.2
N1s	399.51	1.44	21

The degree of MoS_2 functionalization is computed by deconvolving XPS spectra with a sum of Gaussian/Lorentzian lineshapes in the S2p, N1s, and C1s regions. First, however, the Mo3d region is analyzed to determine the approximate fraction of 2H and 1T phases Fig. 2.9[67]. We find that the Mo3d spectra for ce-, acetate- and amide-MoS_2 are qualitatively similar, indicating that the Mo atoms are unaffected by covalent modification and the functional groups are localized on the S atoms evident at higher energies[71]. Fitting parameters are provided in Table 2.1. Deconvolution of the N1s spectra[36] (Fig. 2.9 corroborates

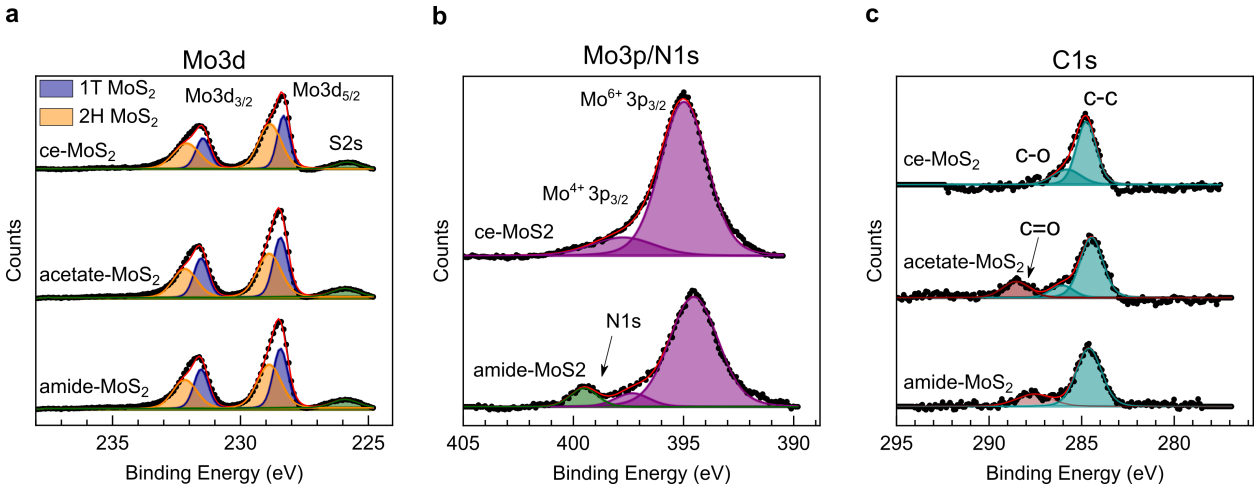

Figure 2.9: Deconvolved XPS spectra of MoS_2. a, XPS spectrum in the Mo3d region for ce-, acetate- and amide-MoS_2. b, XPS spectrum in the Mo3p region for ce- and amide-MoS_2; the peak assigned to the N1s orbital is apparent in amide-MoS_2, but no such peak is evident in ce-MoS_2. c, The C1s region for ce-, acetate- and amide-MoS_2. Functionalized MoS_2 shows clear evidence of a carbonyl peak

the results derived from the S2p region.

Finally, we confirm our results by analyzing the C1s region (Fig. 2.9. We calculate the ratio of the carbonyl peak intensity to that of the adventitious carbon (hydrocarbon contamination), then compare the total carbon intensity to the Mo intensity. For acetate-MoS_2, the degree of functionalization (per Mo atom) is computed to be 26% and 20 % using the S2p and C1s regions, respectively. For amide-MoS_2, the degree of functionalization is calculated to be 26%, 22% and 26% for the S2p, C1s and N1s regions, respectively.

Sample	**Zeta Potential (mV**
Ce-MoS_2	-46(6)
Acetate-MoS_2	-47(3)
Amide-MoS_2	-33(1)

Table 2.2: Zeta potential measurements of as-synthesized and functionalized MoS_2.

2.5 Methods

2.5.1 Ce-MoS_2 synthesis

First, 300 mg of MoS_2 powder (Sigma-Aldrich) is stirred with 3 ml of n-butyllithium for >48 hours under Ar atmosphere. The Li_xMoS_2 product is washed five times with hexane, transferred out of the Ar atmosphere and bath sonicated in 300 ml of water for 60 minutes. The resulting solution is dialyzed until the solution has a pH of 5 (several days). Finally, the solution is centrifuged for 15 min at 1500 rpm to remove any unexfoliated material. The final concentration of suspended flakes is on average 0.3 mg/ml. We functionalize ce-MoS_2 in liquid phase. 20x molar excess 2-iodoacetamide (Fisher Chemicals) or iodoacetic acid (Sigma-Aldrich) is stirred with ce-MoS_2 for five days. The solution is then washed 5 times with water via centrifugation and re-suspension, then centrifuged at 1500 rpm to remove aggregates and is sonicated at low power for 20 minutes. Membranes are fabricated by vacuum filtering a known quantity of MoS_2 solution through a mixed cellulose ester substrate with 25 nm pores (Millipore Sigma), cut to shape and dried for a defined period before testing

2.5.2 Zeta potential measurements

Measurements are conducted on the Malvern Zetasizer Nano ZS instrument, using DTS1070 folded capillary cells. Samples are prepared by mixing equal parts stock acetate-, amide- or ce-MoS_2 solution with a phosphate buffer solution to keep the pH constant at 7.4. Each trial is an average of three runs.

2.5.3 Freeze-drying of MoS_2 membranes

A 3 μm thick ce-MoS_2 membrane is submerged in liquid nitrogen immediately after its fabrication. After freezing, the membrane is dried at low pressures until the ice sublimates. We

fabricate 3 μm thick membranes for SEM imaging only; during filtration tests the thickness is 50–200 nm. Freeze drying is commonly employed to preserve the structure of aerogels and other mesoporous materials, as the process prevents collapse during evaporative drying [74–77]. In our system, the method prevents the high surface tension of water from bringing the flakes together and closing voids on the mesoporous scale. This process allows direct visualization of the MoS_2 membrane structure with the voids intact. We are then able to image and compare, using SEM, a dried and freeze dried ce-MoS_2 membrane fabricated from the same solution under the same conditions (Fig. 3 a-b). We also image, for comparison, a 2 μm acetate-MoS_2 membrane after it is dried and rehydrated Fig. 2.6. We ensure that water has diffused into the acetate-MoS_2 layers by measuring the interlayer spacing after soaking in water for 12 hours (Fig. 2.10).

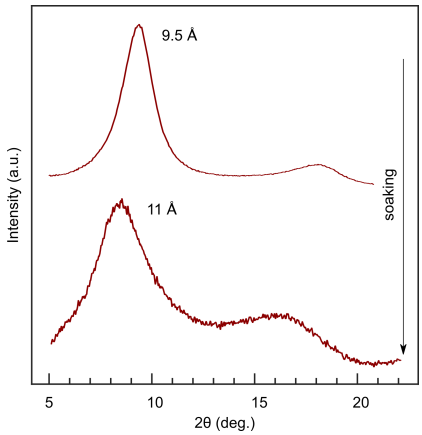

Figure 2.10: XRD of 2 μm acetate-MoS_2 membrane, dried and rewet by soaking in deionized water for 12 hours. This same membrane is, immediately after characterization, freeze dried and characterized by SEM (Fig. 2.7). We note that the dried interlayer spacing is marginally (0.4 Å) smaller than that measured for thinner dried acetate-MoS_2 membranes; this may originate from the broad underlying XRD spectrum of the polymer substrate, which has a varying relative influence depending on membrane thickness.

2.5.4 Preparation of cross-section TEM samples

A 20-50 nm membrane is filtered on a mixed cellulose ester substrate using vacuum filtration. Before letting it dry, the membrane is submerged in water at which point the MoS_2 film

delaminates from the polymer substrate. A small piece of this film is then sectioned using a diamond knife Leica UC6 ultramicrotome in a polymer-resin mold.

2.5.5 Materials characterization

EM characterization was carried out using ThermoFischer/FEI Tecnai Spirit 120 kV and Tecnai F30 300 kV FEG TEMs at the University of Chicago and a ThermoFischer Tecnai F20 TEM at Argonne National Laboratory, operating at 80 kV. We note that, although the images at the University of Chicago are acquired at beam energies above the damage threshold for monolayer MoS_2, the material is temporally stable and no evidence of degradation is observed. Further characterization is carried out using a Bruker Nanoscape AFM operated in tapping mode; a Zeiss Merlin Field-Emission Scanning Electron Microscope operating at 2 kV; a Malvern Zetasizer NanoZS for zeta potential measurements; a Shimadzu IRTracer-100 FTIR; a Bruker D8 Discover GADDS with Vantec2000 2-Dimensional detector for powder XRD; a DSA-100 Drop Shape Analyzer for contact angle measurements; and a Kratos AXIS Nova based on a monochomatic Al Kα X-ray source for XPS measurements.

CHAPTER 3

IONIC AND MOLECULAR TRANSPORT IN RE-STACKED 2D MATERIAL MEMBRANES

3.1 Introduction

Restacked MoS_2 membranes are excellent systems for the extraction of small molecules or ions based on size and charge effects. The free spacing of a hydrated or functionalized membrane (~6 Å, see Fig. 2.5) is commensurate with the size of a hydrated ion (~7-9 Å) [29], but larger than that of a single water molecule (~3 Å). As such, we expect solutes (such as monovalent and divalent ions) to be excluded from the membrane, but water to pass easily through. We test this hypothesis in the following section, using the membranes in a desalination system. With the acetate-MoS_2 membranes, we demonstrate consistently high filtration performance: 92(2)% rejection of Na_2SO_4 and 1.5(6) LMH bar flux, higher than acetamide functionalized MoS_2 (amide-MoS_2) and equivalent to carefully tuned ce-MoS_2. Interestingly, acetate-MoS_2 membranes also demonstrate 6.6 fold selectivity of Cu^{2+} over the monovalent cation Na^+, suggesting the membrane's possible use for selective ion removal and recovery. This seemingly anomalous result is confirmed, and the mechanism elucidated, with a systematic screen of seventeen ions simultaneously.

Further, we explain the effect of molecular functionalization on the interlayer spacing of MoS_2 films using molecular dynamics (MD) simulations. The connection between surface chemistry and membrane structure has previously been attempted using mean field theories that do not account for the layered structure of confined water, which we find is a dominant effect [18]. The MD simulations reveal that the choice of functional group controls the number of water layers within the MoS_2 channel and consequently governs the interlayer spacing and affects water flux. We also find that the diffusion constant of water molecules varies with functionalization but that this has a modest effect relative to the membrane's

physical structure.

3.2 Desalination with restacked MoS_2 membranes

The evolving structure of ce-MoS_2 membranes dramatically affects separation performance, as indicated by the dependence of water flux and ion rejection on membrane drying time. To detail this association, membranes are dried for a defined period in room temperature conditions (humidity 20-30%) after fabrication, then loaded in a stirred, pressure-assisted dead-end filtration cell for tests. All samples are tested in brackish water conditions with 17 mM (2500 ppm) Na_2SO_4 under pressures of 150 psi (10.3 bar). The performance metrics are measured until the ion rejection stabilizes. Acetate-MoS_2 membranes are also tested against 34 mM (2000 ppm) NaCl and 17 mM (2300) ppm $CuCl_2$, the neutral dyes 4-Nitroaniline (NA) and bromothymol blue (BrB).

The ion rejection of ce-MoS_2 membranes increases within the initial drying period but subsequently remains constant (Fig.3.1 a); the flux, on the other hand, decreases by two orders of magnitude as a function of drying time (Fig. 3.1 b). We associate the initial increase in rejection with the closure of percolating voids. Once these voids are closed, no further increase in ion rejection is expected, despite lower water flux values; restacking to bulk entirely seals off portions of the membrane instead of forming smaller water channels. By tuning the drying time (to the minute) ce-MoS_2 membranes can display performance as high as 95(1)% rejection of Na_2SO_4 with 0.8(2) LMH bar water flux. Even though ce-MoS_2 shows great potential for ion separations, the transient membrane structure makes the membrane hard to preserve for practical applications.

The drying-dependent performance of acetate-MoS_2 differs qualitatively from that of ce-MoS_2. The ion rejection plateaus more slowly for acetate-MoS_2 membranes (Fig.3.1 a). Furthermore, when the membrane is dried completely by heating at 60 °C for four hours, after rehydration during testing, water flows at 1.5(6) LMH bar while the ion rejection

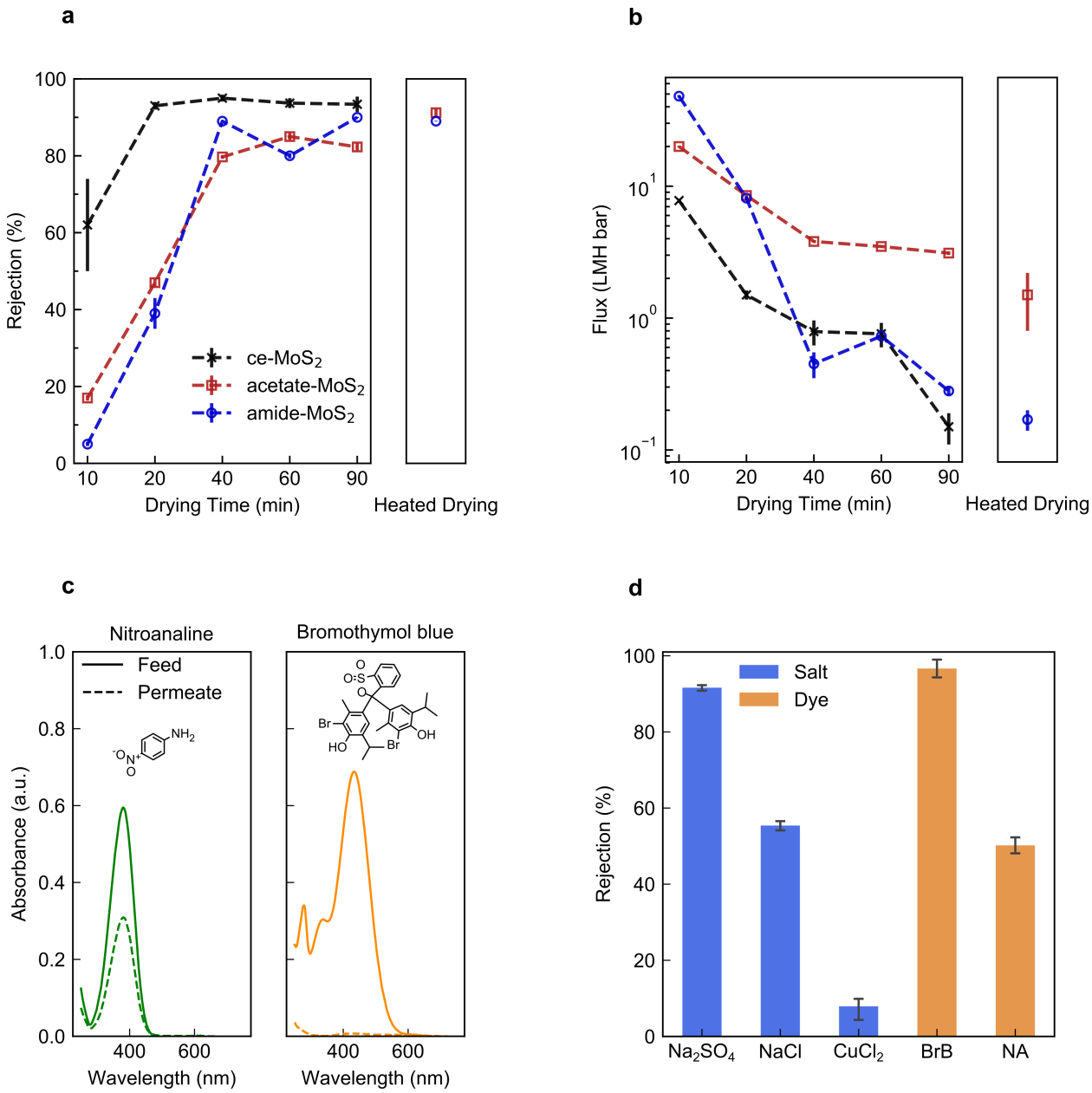

Figure 3.1: Membrane separation performance: hydration dependent ion rejection (**a**) and water flux (**b**) for ce-, acetate- and amide-MoS_2 in 17 mM Na_2SO_4;water flux and ion rejection for acetate- and amide-MoS_2 prepared by heated drying and rehydrating are also shown. **c**, UV-VIS spectra of two neutral dyes, NA (molecular size ~4.32 Å× 6.89 Å[78]), and BrB at pH = 5.6 (~10.8 Å× 13.5 Å[79]), filtered through acetate-MoS_2 membranes. The spectra for feed and permeate solutions are shown, along with a drawing of the dye molecules to emphasize the size discrepancy. **d**, solute rejection of A_2B (Na_2SO_4), AB (NaCl), and AB_2 ($CuCl_2$) salts as well as the two neutral dyes, NA and BrB, using acetate-MoS_2 membranes. The rejection between NaCl and $CuCl_2$ indicates a 6.6 fold selectivity of Cu^{2+} to Na^+.

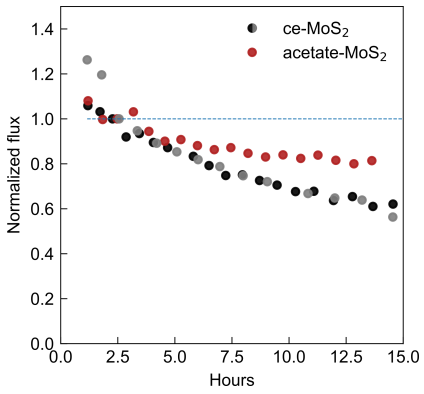

Figure 3.2: Flux of DI water through ce- and acetate-MoS_2 membranes as a function of time. The flux is normalized to the point after which 5 ml of permeate is collected, which is 2.6, 1.5 and 2.3 LMH bar for the two ce-MoS_2 experiments and the single experiment for acetate-MoS_2, respectively.

reaches 92(2)% (ce-MoS_2 membranes dried under the same conditions are impermeable). Furthermore, the flux of acetate-MoS_2 decays at a slower rate (and eventually appears to plateau) relative to that of ce-MoS_2, which nearly halves in 15 hours Fig. 3.2. This result suggests that functionalizing MoS_2 with acetate ions is a reliable method to achieve high rejection of divalent anions, only transiently attainable via partial drying of ce-MoS_2. The amide-MoS_2 membranes exhibit smaller flux at long drying times relative to acetate-MoS_2. They do remain permeable after complete drying, however, unlike the ce-MoS_2 membranes: dried amide-MoS_2 membranes exhibit 89.0(1)% rejection with a flux of 0.7(2) LMH bar.

We test acetate-MoS_2 membranes against two different neutral dyes in order to isolate the size sieving from the electrostatic repulsion effects on solute rejection (Fig. 3.1 c). Acetate-MoS_2 rejects the large neutral dye molecule BrB (molecular size 10.8 Å$\times$ 13.5 Å[79]) with an efficacy of 98%, but only partially impedes the permeation of the smaller neutral molecule NA (~4.32 Å$\times$ 6.89 Å[78]), corroborating the import of the size sieving effect (Fig. 3.1 d).

We also measure the rejection of NaCl and $CuCl_2$ (Fig. 3.1 d). Interestingly, $CuCl_2$ is barely impeded by acetate-MoS_2 membranes, likely a result of both the slightly smaller hydrated radius of Cu^{2+} compared to Na^+ and SO_4^{2-} and its overall charge[80]. We note the selectivity towards divalent cations over monovalent cations measured here (calculated as the

reciprocal of the ratio of $CuCl_2$ and NaCl rejection) is 6.6, higher than that of recent studies of 2D materials, which report divalent over monovalent cation selectivity of, at a maximum, ~1 – 1.9 [81–83]. In commercial Nafion ion exchange membranes, the selectivity is typically reversed, with monovalent cations preferentially transported over divalent cations[84].

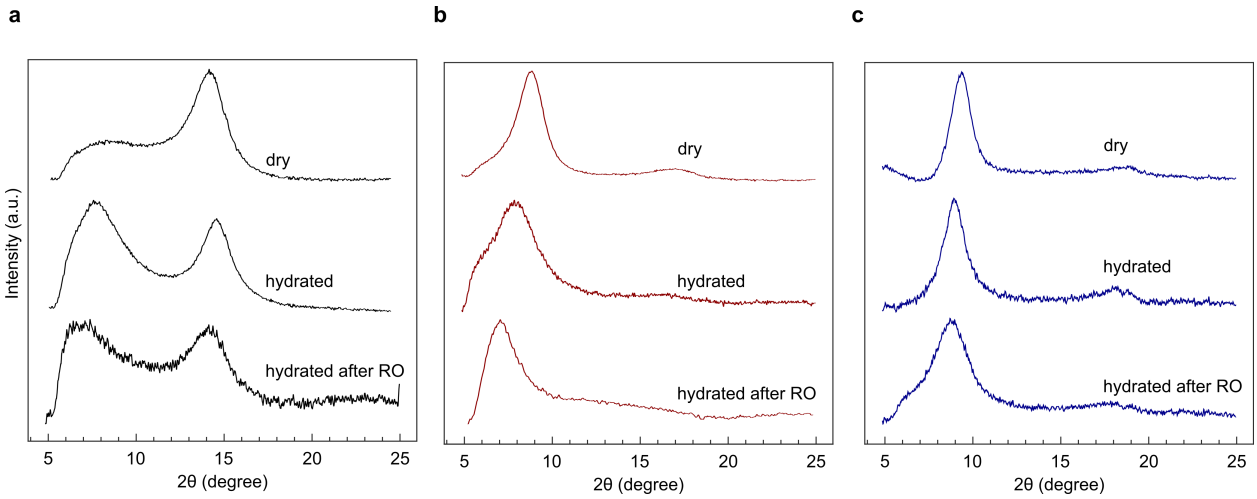

Figure 3.3: XRD spectra of ce- (**a**), acetate- (**b**) and amide-MoS_2 (**c**) membranes when completely dried, in their hydrated state after fabrication, and after testing in a dead-end filtration cell. The XRD spectrum for hydrated ce-MoS_2 shows a bulk-like peak that retains its intensity after testing whereas no such peak is apparent for functionalized MoS_2, indicating that water can diffuse between the functionalized MoS_2 sheets. During membrane testing, the hydrophilic acetate-MoS_2 membranes swell as water is forced through the channels defined by neighboring flakes. We note that there is no noticeable delay between the time at which pressure is applied to the feed solution and when the permeate begins to accumulate, indicating fast rehydration of acetate-MoS_2 membranes. The interlayer spacing increases from 9.9 Åto 12 Å, to match that of hydrated ce-MoS_2. The interlayer spacing of the more hydrophobic amide-MoS_2, on the other hand, remains relatively constant (increasing only 0.3 Å, from 9.6 Åto 9.9 Å, an order of magnitude less than that of acetate-MoS_2)

The dependence of water flux on MoS_2 surface treatment is a result of differing water diffusion constants within membrane channels and varying membrane porosities. Diffusion constants are calculated via MD simulations discussed in the subsequent section; porosity is determined by structure of MoS_2 membranes on the microporous and mesoporous scales. As depicted in Fig. 3.3, ce-MoS_2 partially restacks to bulk, decreasing the effective porosity of the membrane, whereas the acetate- and amide-MoS_2 channels remain uniformly open.

The different behaviors demonstrated by amide-MoS_2 and acetate-MoS_2 are likely a result of their differing hydrophilicities (Fig. 3.4); functionalization with acetic acid (acetamide) increases (decreases) the hydrophilicity relative to that of ce-MoS_2. Consequently, the interlayer spacing of acetate-MoS_2 increases to a greater extant relative to that of amide-MoS_2 when rehydrated, as shown in Fig. 3.3. In the following sections, we employ MD simulations to provide a quantitative description of the microporous structure of ce- and functionalized MoS_2 that rationalizes with greater detail each sample's equilibrium hydrated interlayer spacing.

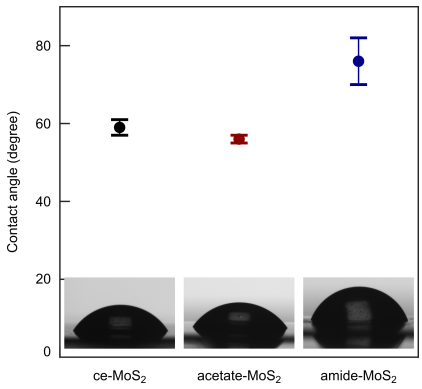

Figure 3.4: Contact angles of functionalized and ce-MoS_2. Contact angles are measured with ultrapure water on MoS2 membranes. Reported values are an average of at least four measurements. Of particular note is the greater hydrophobicity of amide-MoS_2, resulting from the quenching of ce-MoS_2 surface charge[71]. See Section 3.7 for procedural details

3.3 Ion selectivity in MoS_2 channels

Although MoS_2 membranes are demonstrably selective towards water molecules over all dissolved species tested above, they are still semi-permeable to ions, especially when the ions are positively charged. The near complete loss of selectivity towards the divalent Cu^{2+} species (Fig. 3.1 is surprising, given its similar size relative to that of Na^{+}. This result indicates that charge and size alone does not explain ion transport through the MoS_2 channels. Furthermore, the selective permeation of ions in this MoS_2 film may mean it can be used for

efficient water decontamination or resource extraction from dilute aqueous sources[85].

To test the selectivity of acetate-MoS_2, we conduct a screen of seventeen different ions in forward-osmosis diffusion experiments; we also test the uptake of the membrane (static absorption of ions between MoS_2 layers) for the same seventeen ions (Fig. 3.5.

To conduct the screen, we load the membrane between two reservoirs, one of which is filled with the seventeen-salt mixture (4 mM of each salt), and the other is DI water. The concentration gradient across the membrane drives the dissolved ions across the film to the DI water side. Using inductively-coupled mass-spectroscopy (ICPMS), we measure the concentration of *each ion* in the DI water side as a function of time. From these traces, we extract the overall permeability of all seventeen ions.

We also conduct uptake experiments, wherein a given membrane is soaked in both single-salt solutions (Fig. 3.5 d or a mixed-salt solution Fig. 3.5 e-f. The membrane is then rinsed and dissolved; the ions trapped in the membrane are released into a solution, which is sub-micron filtered and its concentration tested using ICPMS. Complete procedural details for all experiments can be found in Wang *et al.*[44].

The permeation experiments with bare PTFE membranes (Fig. 3.5 a) reflect bulk trends in ionic mobility: as the hydration enthalpies of the ions increase, their diffusion constants decrease. This trend is broken, however, for both functionalized and as-synthesized MoS_2 membranes(Fig. 3.5 b-c). We first note that the level of selectivity towards the small monovalent ions generally increases with introduction of MoS_2, indicating that the membrane is playing a dominant role in transport. Most crucially, we see a relative increase in the transport of Pb^{2+} and Cu^{2+}, consistent with our results in Fig. 3.1.

The uptake experiments reveal a similar phenomenon, although it is even more exaggerated. In single-ion uptake tests (Fig. 3.5 d) the uptake of Pb^{2+} and Cu^{2+} is slightly higher than that of any other ion; in the mixed uptake experiments, however, the uptake of these two divalent cations far outstrips an of their competitors. This result indicates that the

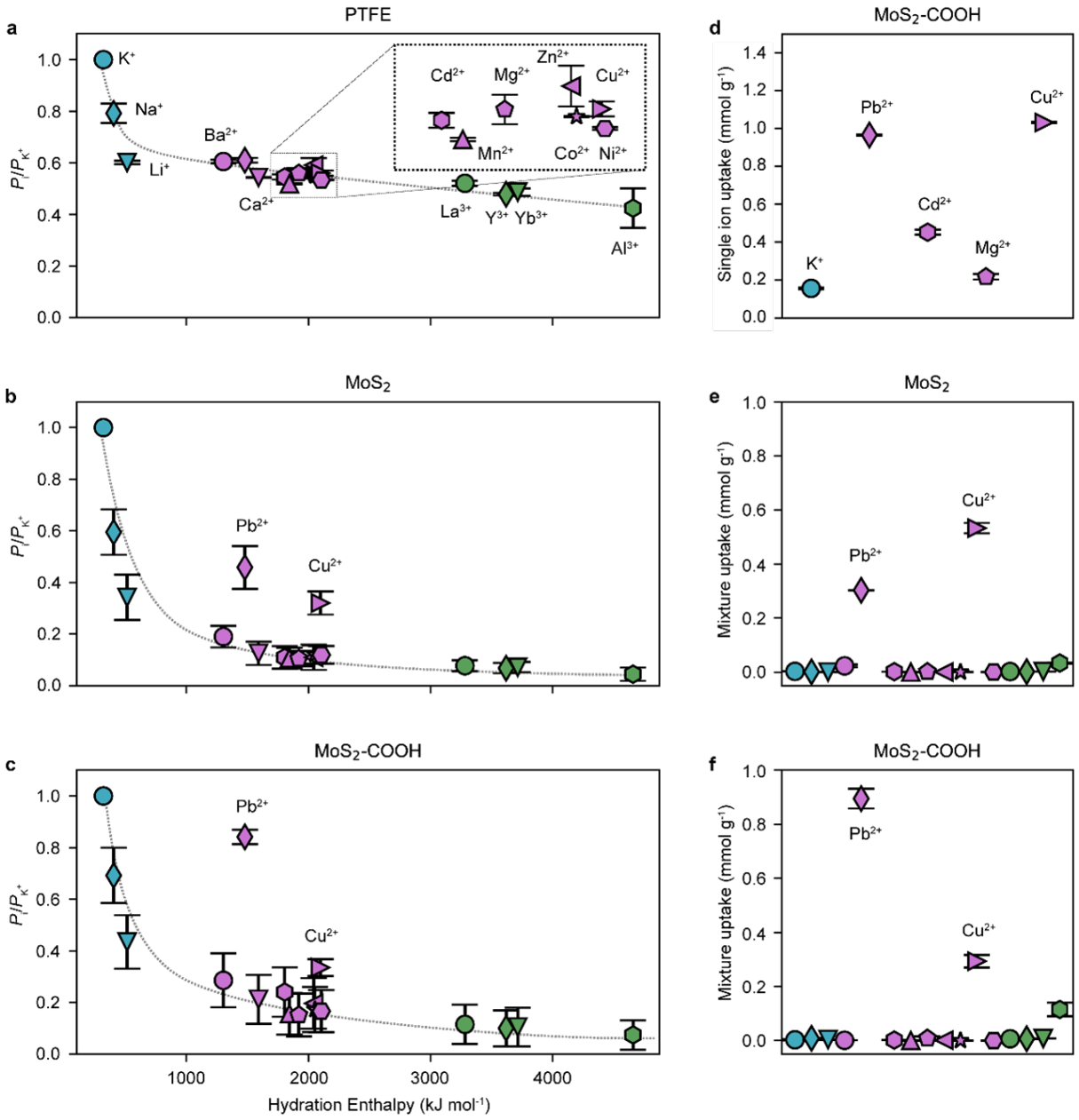

Figure 3.5: The relative ion permeation rates versus the hydration enthalpies of ions across bare PTFE (**a**), ce-MoS_2 (**b**) and acetate-MoS_2 (**c**) membranes. The dashed lines are guidelines. **d**. Uptake in the acetate-MoS_2 membranes in the single ion solution (~4 mM). Uptake in ce-MoS_2 (**e**) and acetate-MoS_2 (**f**) membranes in a mixed solution. The mixture is comprised of: ~4 mM, Cl^-/NO^{3-} anions, pH $\approx$ 4.13

increased permeance of Pb^{2+} and Cu^{2+} is a function of their enhanced interactions with the MoS_2 and functional groups, leading to higher overall concentrations inside the membrane. Further details concerning the role of the functional group, and ion pairing effects can be found in Wang *et al.*[44].

3.4 MD simulations of molecular transport in MoS_2 membranes

3.4.1 Water dynamics in MoS_2 channels

To elucidate the factors contributing to water diffusion in ce- and functionalized MoS_2, we conduct MD simulations on single channels formed by parallel MoS_2 sheets (the setup is shown in Fig. 3.6) a. By characterizing the water structure and dynamics at a sequence of interlayer spacings for ce-, acetate- and amide-MoS_2, we cover the entire parameter space attainable in our experiments. To probe the effects of surface modification, we decorate the MoS_2 sheets with functional groups at a similar density to that measured experimentally (Fig. 3.6) b).

To compare water flux between samples, we compute the diffusion constant (derived from the mean squared displacement of water molecules in the MoS_2 channel) for interlayer spacings from 10 to 17 Å. We find that for a 12 Åinterlayer spacing, the diffusion constant varies with surface chemistry as ce-MoS_2 > amide-MoS_2 > acetate-MoS_2 Fig. 3.6) c). We attribute the lower diffusion constants for acetate-MoS_2 and amide-MoS_2 partially to steric obstruction arising from the functional groups extruding from the MoS_2 surface. Given consistent interlayer spacing and mesoscale morphology for all membrane surface chemistries tested here, our MD simulations indicate that ce-MoS_2 should exhibit the fastest water flux. Experimentally, however, ce- and acetate-MoS_2 have equivalent hydrated interlayer spacings (12 Å) but acetate-MoS_2 demonstrates the highest water flux. This result suggests that the restacking to bulk behavior effectively reduces the porosity of the membrane (or increases the tortuosity), leading to reductions in flux that overcome the marginally larger diffusion constant for ce-MoS_2 relative to functionalized MoS_2. The reduced flux of amide-MoS_2 relative to acetate-MoS_2 likely derives from its smaller interlayer spacing in the hydrated state. An analytical relationship between these morphological factors and the total water flux through the MoS_2 membranes tested here is provided in Section 3.6.

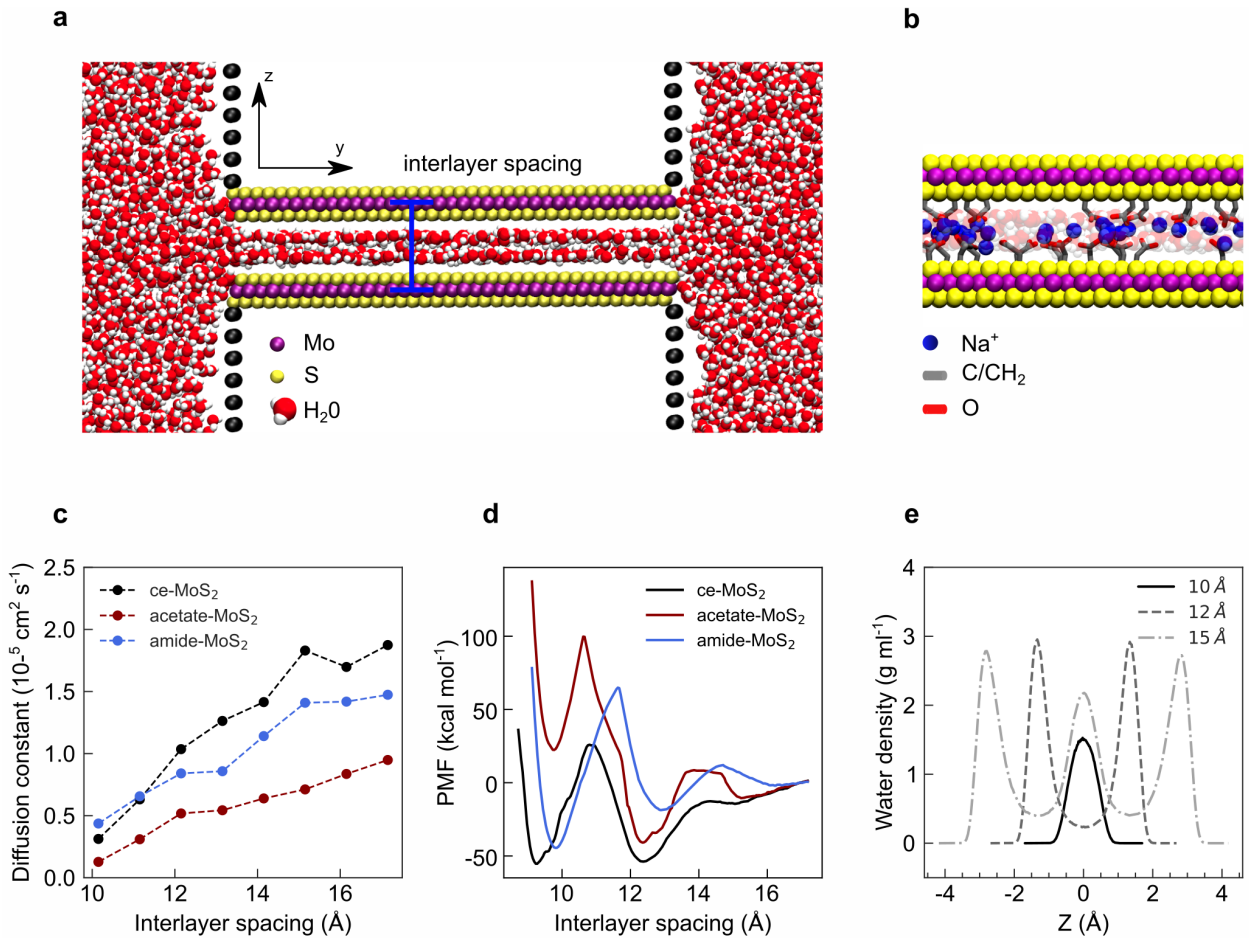

Figure 3.6: MD simulations describing the dynamics and structure of water in membranes. **a**, MD simulation snapshot showing water confined in a MoS_2 channel with 12 Åinterlayer spacing (center-to-center Mo–Mo distance). **b**, Cross section of acetate-MoS_2 with functional groups placed randomly at 0.2 per Mo atom, **c**, The diffusion constant of water in ce-, acetate-, and amide-MoS_2 channels as a function of interlayer spacing. **d**, PMF as a function of interlayer spacing for ce-, acetate-, and amide-MoS_2. **e**, The density of water as a function of the z-coordinate in an acetate-MoS_2 channel. Here, we show profiles for interlayer spacings that exhibit clearly resolved water layering.

3.4.2 Water structure and interlayer spacing

The equilibrium spacing between MoS_2 sheets in an aqueous medium governs the ion rejection and water flux through the membranes assembled from those sheets. The equilibrium spacing is determined by the complex interplay of electrostatic and van der Waals interactions in addition to hydration forces arising from the confinement of water in the MoS_2 channel[86]. To quantify the sum of these interactions, we use umbrella sampling to calculate the potential of mean force (PMF) as a function of interlayer spacing (Fig. 3.6) d). This approach captures the effects of water structure on the interlayer spacing at the subnanometer scale, the details of which are not included in models such as extended DLVO theory[18, 86]. While our model, which is parametrized to capture water–water and water–MoS_2 interactions, may break down at small interlayer spacings where MoS_2–MoS_2 interactions dominate, at the spacings of interest here the MoS_2 interactions are largely mediated by water molecules and hydration forces dominate [86] (for futher details, see Supplementary Fig. 15 in Hoenig *et al.*[35]).

The PMF profiles depicted in Fig.3.6 d display clear minima at around 9–10 and 12–13 Å, but the relative depths of these two minima vary dramatically with surface functionalization. As detailed in Supplementary Section 17 of Hoenig *et al.*[35], these minima and their relative depths explain the stability and value of the interlayer spacing of ce- and functionalized MoS_2 membranes in aqueous media. The structure of the PMFs in Fig. 3.6 d can be interpreted in terms of interactions in the system at the molecular level. The overall oscillatory structure is well understood and is a result of the discrete nature of the water layers confined within the channel [86–88]. To illustrate this, we compute the water density profile along the membrane normal at fixed interlayer spacings between 10 and 17 Å(Fig. 3.7). The minima in the PMF profiles at around 10, 12.5, and 15 Åcorrespond to one, two, and three layers of water inside the channel, respectively; this is shown for acetate-MoS_2 in Fig. 3.6e.

Given that hydrated ce- and acetate-MoS_2 membranes have experimental interlayer spac-

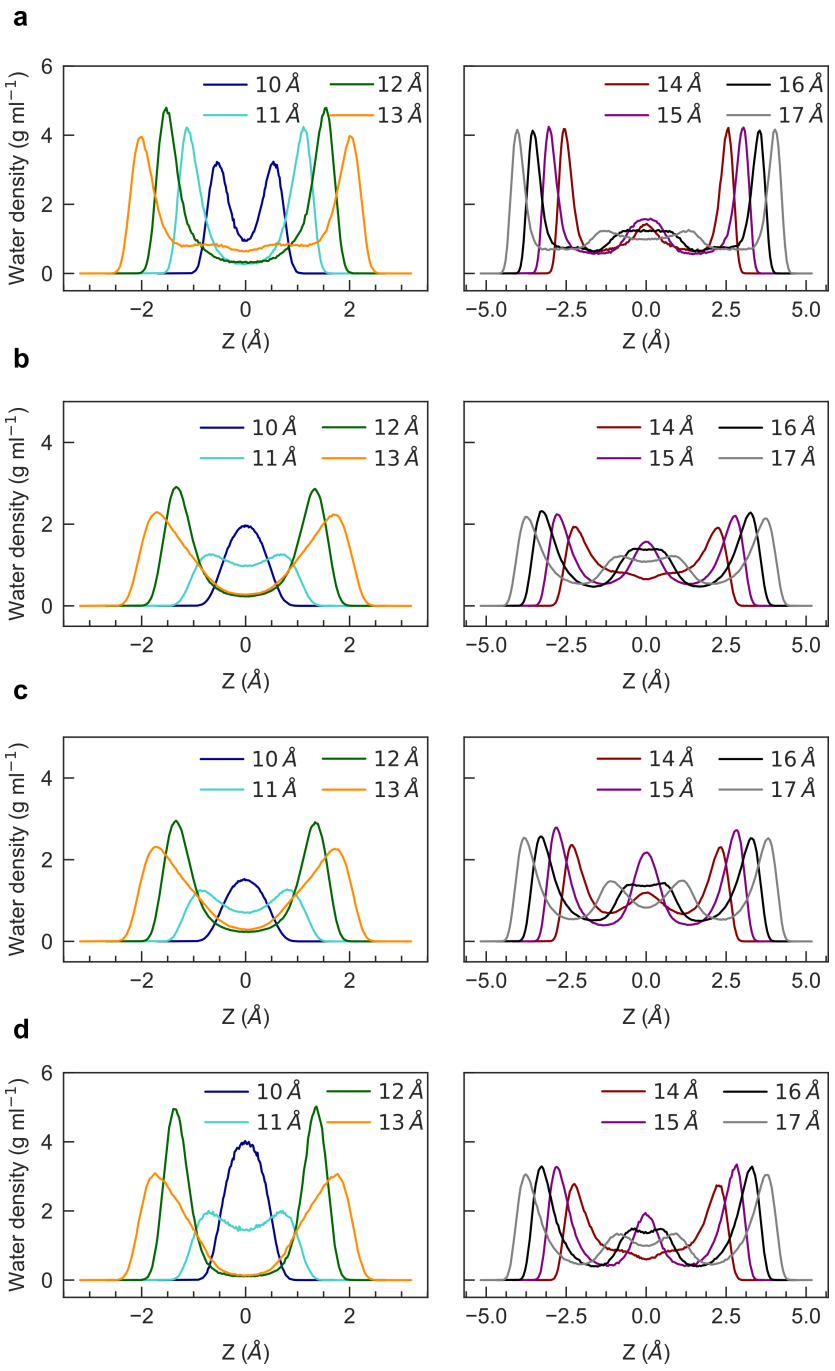

Figure 3.7: MD simulations of water density as a function of the distance away from the channel center for a range of interlayer spacings for: **a**, ce-MoS_2, **b**, acetate-MoS_2 **c**, amide-MoS_2 and **d**, neutral-MoS_2. We note that for ce-MoS_2, the monolayer of water at the 10 Åinterlayer spacing is pulled apart slightly by the surface charge. This results in two peaks in the density profile, even though there is only one layer of water. These peaks are much closer together and less resolved than the true bilayer of water visible at the 12 Åinterlayer spacing.

ings of 12 Å, the density profiles in Fig. 3.7 indicate that each MoS_2 sheet adsorbs a single layer of water approximately 2 Åthick. We conclude that a bilayer of water occupies each channel, as hypothesized in prior studies[53, 89–92]. These results also indicate that the steric effects of functional groups decorating the MoS_2 surface are secondary to that of the structure of water within the MoS_2 channel; within our current experimental setup, the interlayer spacing can only take on discrete values corresponding to an integer number of water layers. It remains an open question whether a greater degree of functionalization ($\gg$20%) might destroy the ordering of the water, thereby reducing the hydration forces and permitting finer control over the interlayer spacing. However, this will likely also reduce the flux due to the density of functional groups in the channel.

3.5 Discussion

We have shown that the ion sieving properties of MoS_2 membranes can be tuned by varying the degree of hydration. We have also demonstrated that membrane functionalization with acetic acid groups is a promising route toward consistently achieving high salt rejection and water flux. Direct evidence of the effect of surface charge would be useful to evaluate the efficacy of alternative functional groups but would require complete decoupling of surface charge from membrane morphology. Increasing the water flux of acetate-MoS_2 membranes could be realized by employing thinner films with less surface topography; this may be accomplished through synthesis of larger and more uniform flakes, employing a smoother substrate, or through alternative fabrication techniques[93]. MD simulations have revealed the structure of water within the membrane that forms the basis for its hydration-dependent structure. In addition, the trends derived from these MD simulations corroborate the dominance of the rehydration behavior of MoS_2 membranes in separation tests and emphasize the importance of water structure on both the microporous and mesoporous scales. Our work provides structural and chemical information on MoS_2 membranes, providing insight into their behavior

as separation membranes or when employed in nanofluidic platforms or even as electrode materials.

3.6 Relationship between flux and diffusion in MoS_2 membranes

3.6.1 Derivation of the relationship between flux and diffusion

The experimental measurement of water flow through the membrane is water flux, defined by the flow rate per unit area of membrane. The simplest model of a membrane is an array of straight, unconnected pores extending through the entirety of its bulk. Using this model as a starting point, the flux J through the membrane is determined by the flux through each pore J_p times the porosity of the membrane:

$$J = \frac{N_p A_p}{A_m} \tag{3.1}$$

, where N_p is the number of pores in the membrane, A_p is the area of each pore, A_m is the area of the full membrane and the factor $\frac{N_p A_p}{A_m}$ is the membrane porosity. The geometry of a MoS_2 membrane is more complicated than the simple picture described above, however. To build a model, we consider a single MoS_2 flake at the surface of a membrane; here, the area available for water permeation is proportional to the space between the flake and the membrane times the circumference of the flake. We take this area to represent a pore in our system, so

$$A_p \approx (d - d_{MoS_2})w \tag{3.2}$$

where d is the interlayer spacing, $d_{MoS_2} \approx 6$ Åis the thickness of the excluded volume of a single layer of MoS_2, and w is the linear dimension of an average flake (e.g. the flake diameter or side length, depending on the flake geometry). The constant of proportionality is clearly a complicated function of the surrounding flakes and underlying flakes, so we neglect this

complexity in favor of a simple model. In this simple model, N_p is related to the number of flakes that can fit on the surface of the membrane:

$$N_p \approx \frac{A_m}{w^2} \tag{3.3}$$

Putting Eqs. eqs. (3.1) to (3.3) together, we arrive at the result, which is in agreement with recent literature[71]

$$J \approx (d - d_{\mathrm{MoS_2}} w) J_p \tag{3.4}$$

The flux through a single pore J_p has contributions from the entrance and exit of the pore, as well as the transport through the length of the pore. In the limit where entrance and exit rates are fast relative to intrapore transport, the flux is related solely to the pressure drop and diffusion constant. This can be seen using Fick's law and the Van't Hoff equation. Fick's law states that the one-dimensional osmotic flux (in our specific case J_p) due to a concentration gradient ∇C is,

$$J_p = -D \nabla C \tag{3.5}$$

where D is the diffusion constant and C is a number concentration. We are interested in flow driven by pressure rather than an osmotic gradient. The osmotic pressure drop generated by a concentration difference is given by the Van't Hoff equation in the low concentration limit

$$\Delta P = k_B T \Delta C \tag{3.6}$$

where K_B is Boltzmann's constant, T is the temperature and ΔP is the applied pressure. The concentration difference ΔC is measured between two reservoirs on opposite sides of the membrane. The average concentration gradient is given by

$$\nabla C = \frac{\Delta C}{L} \tag{3.7}$$

where L is the distance between the two reservoirs or the thickness of the membrane. Combining Eqs. eqs. (3.5) to (3.7),

$$J_p = -\frac{D\Delta P}{k_B T L} \tag{3.8}$$

Plugging Eq. 3.8 into Eq. 3.9 we arrive at the relationship between the experimentally measured flux and the diffusion constant computed through MD simulations:

$$J \approx \left(\frac{d - d_{\mathrm{MoS_2}}}{wL}\right) \frac{D\Delta P}{k_B T} \tag{3.9}$$

3.6.2 Application of relationship between flux and diffusion in a realistic membrane

In a real membrane, the pores are interconnected in complicated ways. Two assumptions can remove this difficulty, however. First, we assume that the porosity of each layer is the same, second, we assume that the connections between layers permit fast transport, just like the entrances and exits of the channels. Finally, the distance a water molecule must traverse between two reservoirs is much further than the thickness of the membrane, due to the tortuosity of the path. This can be accounted for by simply replacing L with an effective length L_{eff}.

To compare the simulated trend in diffusion to our experimental observations, we must account for variations to the membrane porosity, tortuosity, and interlayer spacing, which depend on preparation. In a simple model system, the total flux through a membrane J can be related to these parameters using the relationship derived above (Eq. 3.9).

We attribute the lower observed flux for amide-MoS_2 relative to acetate-MoS_2 in part to

the smaller experimental interlayer spacing for amide-MoS_2 Fig. 3.3, which corresponds to a smaller free channel spacing $d - d_{MoS_2}$ in Eq. 3.9. In the hydrated state, the free channel spacing is 4 Åfor amide-MoS_2 and 6 Åfor acetate-MoS_2. The difference in measured fluxes could also originate in part from differences in the mesoporous morphology including the effective path length L_{eff} and the connectivity. Together, these considerations explain the lower overall flux exhibited by amide-MoS_2 relative to acetate-MoS_2, despite the similar diffusion constants computed in our MD simulations. While our MD simulations are incapable of capturing the connectivity, porosity, and tortuosity of the membranes on the mesoporous scale due to computational cost, they can be used to interpret the experimental changes in interlayer spacing.

3.7 Methods

3.7.1 Reverse osmosis tests

Circular membranes with 2.5 cm diameter are loaded into a pressure cell (Sterlitech); 100 ml of 17 mM Na2SO4 solution is carefully added to the cell; the solution is then stirred at 300 rpm and the cell pressurized at 150 psi (10.3 bar). The conductivity of the feed and permeate is measured and the rejection is computed as

$$R = 1 - \frac{C_{permeate}}{C_{feed}}$$

. Flux and conductivity data are collected once for every 3 ml of permeate. The feed concentration is recalculated for each data point based on the permeate conductivity. Data is collected until ion rejection stabilizes or rises slowly and linearly due to the increasing conductivity of the feed solution. The reported flux and rejection values for a given experiment are the average of three stabilized values. Each data point displayed for all ce-MoS_2 and fully dried acetate-MoS_2 are then an average of two separate membranes; data for amide-

and partially dried acetate-MoS_2 are from single membranes (a different membrane for each drying time). The value in parentheses following the reported value provides the uncertainty in the final digit, calculated as the standard deviation of all points used in the final averaging. UV-VIS data measuring the dye concentration are taken using a Shimadzu UV-3600 Plus UV-VIS-NIR spectrophotometer. The relative concentration is related to the absorbance through application of Beer's law. The feed concentration for both dyes is 50 μM.

3.7.2 MD simulations

The simulation geometry is schematized in Fig. 3.6 a and described in the main text. The regions above and below the MoS_2 sheets are blocked off using Weeks-Chandler-Andersen particles[94] to save computational cost by reducing the number of water molecules in the simulation. We use the SPC/E water model[95], held rigid using the SHAKE algorithm[96]. The atoms of the MoS_2 sheets are immobile during the simulations. The water-MoS_2 interactions are parameterized mostly according to the Luan and Zhou force field[97] and the acetate and acetamide functional groups are modelled using the DREIDING force field field[98] (see Supplementary Information in Hoenig *et al.*[35] for details). The acetate and acetamide groups are tethered to the surface with a S-CH_2 bond, described by the DREIDING force field. The functional groups are randomly distributed over the surfaces of the MoS_2 sheets at a surface coverage of 0.20 groups per Mo atom. The density profiles and mean squared displacements (MSDs) are averaged over ten instances of the random placement of the functional groups.

For charged but un-functionalized MoS_2, the total negative charge on the sheets is the same as the total charge on the acetate groups at the surface coverage above to permit a direct comparison (see Supplementary Information in Hoenig *et al.*[35] for details). In both the acetate-functionalized and charged MoS_2 simulations, charge neutrality is maintained by adding sodium ions, which are modelled with the Joung and Cheatham potential[99].

Charge fluctuations in the sheets are probably important to capture the correct dynamics of the sodium ions, but we are only interested in the dynamics of the water molecules, so we only consider static charges[100].

The system is held at a temperature of 298 K and a pressure of 1 atm using the Nosé-Hoover style algorithm of Shinoda, Shiga, and Mikami[101–105]. The barostat is nonstandard and is discussed in more detail in the Supplementary Information of Hoenig *et al.*[35]. The simulations are performed using the LAMMPS simulation package[106], modified for the nonstandard barostat. The modified code is available upon request.

The MD snapshots are generated with the VMD program[107, 108]. The PMFs are computed using umbrelling sampling with the COLVARS package[109] and the Weighted Histogram Analysis Method[110–112] (see Supplementary Information in Hoenig *et al.*[35] for details). The density profiles and mean squared displacements (MSD) are computed for molecules that are inside the channel and at least 1 nm from the edge of the MoS_2 sheet. The MSD is only computed in the y-direction, which is the periodic dimension of the MoS_2 sheets. To compute a two-dimensional diffusion constant, each simulation is performed twice: once with the lattice a direction of the MoS_2 sheet oriented parallel to the y-axis, and once with the lattice a direction parallel to the x-axis. These two MSDs are summed to compute the two-dimensional diffusion constant. This ensures that diffusion along the two nonequivalent directions on the MoS_2 surface is accounted for.

CHAPTER 4

IN SITU GENERATION OF (SUB)NANOPORES IN FEW-LAYER MOS_2 MEMBRANES

4.1 Introduction

The precise fabrication of nm and sub-nm pores in ultrathin films (one to several atomic layers) will enable membranes with both high selectivity and permeance. The transport behavior of ions and small molecules confined to nm-scale pores or channels found in such membranes differs dramatically from that measured in bulk liquids. Under confinement, the discrete nature of molecules and atoms, ionic correlations, and long-range electrostatic interactions as well as specific adsorption play large roles in the overall dynamics[5, 37, 113–115], which can be manipulated via the nanopore characteristics to optimize species selectivity. If successfully fabricated on a large scale, nanoporous membranes would be applicable to batteries, fuel cells, osmotic power generators, and separation processes [16, 116–119]. They would be especially useful for ion separations, which can enable efficient water decontamination, water softening, and resource recovery from aqueous solutions[85, 120–127].

To date, the fabrication of arrays of nm pores on ultrathin membranes made from two-dimensional (2D) materials, such as graphene and transition metal dichalcogenides, has been demonstrated with electron and ion irradiation, as well as oxygen plasma etching[14, 56, 128–131]. These methods have been used to create pores in the sub-nm range but have drawbacks including the complexity of the instruments involved and significant pore-size variation within a given device. Nanopores can also be fabricated in ultrathin membranes via bottom-up methods by introducing defects during crystal growth[14, 132, 133]. All of these membrane fabrication techniques are based on ex situ methods, which suffer from pore blocking by trapped nanobubbles, the introduction of ambient contaminants, and often

display a large degree of variation between devices[134, 135].

Here we develop a new in situ fabrication method to generate (sub)nm pores with tunable pore size and density by applying a transverse electric field across polycrystalline membranes. This method exploits the electrostatic and electrochemical effects from the strong electric field formed across the 2D semiconductor, molybdenum disulfide (MoS_2) with the configuration of electrolyte gating[136]. The porosity is determined by the strength and duration of the applied electric field, as well as the atomic features of the starting material. Using few-layer mechanically exfoliated MoS_2 and vertically aligned MoS_2 films for comparison, we pinpoint the critical role of grain boundaries in polycrystalline MoS_2 for the generation of nanopores. We demonstrate an all-solid-state membrane with average pore size ranging from $<$1 nm to 4 nm in diameter via in situ tuning. Our pore fabrication procedure expands the total pore area at a rate down to 0.2 $nm^2\ s^{-1}$, allowing us to control the pore sizes with sub-nm precision.

4.2 Characterization of and pore creation in few-layer MoS_2

4.2.1 Characterization of few-layer MoS_2

We choose MoS_2 as our starting material due to its nm-scale thickness, its electrochemical activity and tunability via the material synthesis parameters. The crystallinity of the pristine membrane determines its response under an applied electric field. Grain boundaries and edge sites, with dangling bonds and defects, are well-known chemically active sites in MoS_2, whereas the basal plane of MoS_2 is relatively inert[137, 138]. We hypothesize that the boundaries between MoS_2 crystallites act as seeding points where, upon partial degradation, pores are formed. Therefore, chemical vapor deposition (CVD) grown few-layer MoS_2 films (CVD-MoS_2) with a high-density of grain boundaries and mechanically exfoliated MoS_2 (ME-MoS_2), which are devoid of grain boundaries[139], are chosen for direct comparison.

Few-layer (8 nm) MoS_2 films are grown via molybdenum sputtering and subsequent sulfurization[140–142]. Both ME- and CVD-MoS_2 are transferred to a silicon nitride (SiN) chip with a single 300-500 nm diameter pore, over which the film is freely suspended (Fig. 4.2). Atomic Force Microscopy (AFM) images show that the CVD-MoS_2 films have nanoscale surface topography due to the polycrystalline nature of the thin film, in contrast to ME-MoS_2, which is atomically smooth, absent blisters and wrinkles (Fig. 4.3). High-resolution scanning transmission electron microscopy (STEM) imaging is conducted on both CVD- and ME-MoS_2. Real-space images and selected-area electron diffraction (SAED) of ME-MoS_2 confirms the single crystalline nature of the thin film (Fig. 4.1 a, b). In stark contrast, CVD-MoS_2 is highly polycrystalline with nm-scale domains as shown in the STEM image and SAED (4.1 c, d). Continuous rings evident in the CVD-MoS_2 diffraction pattern indicate that the grains are randomly rotated in-plane with respect to each other, and Moiré patterns evident in real-space images indicate that grains are partially overlapping. The grain boundaries in CVD-MoS_2 can extend entirely through the membrane, as evidenced

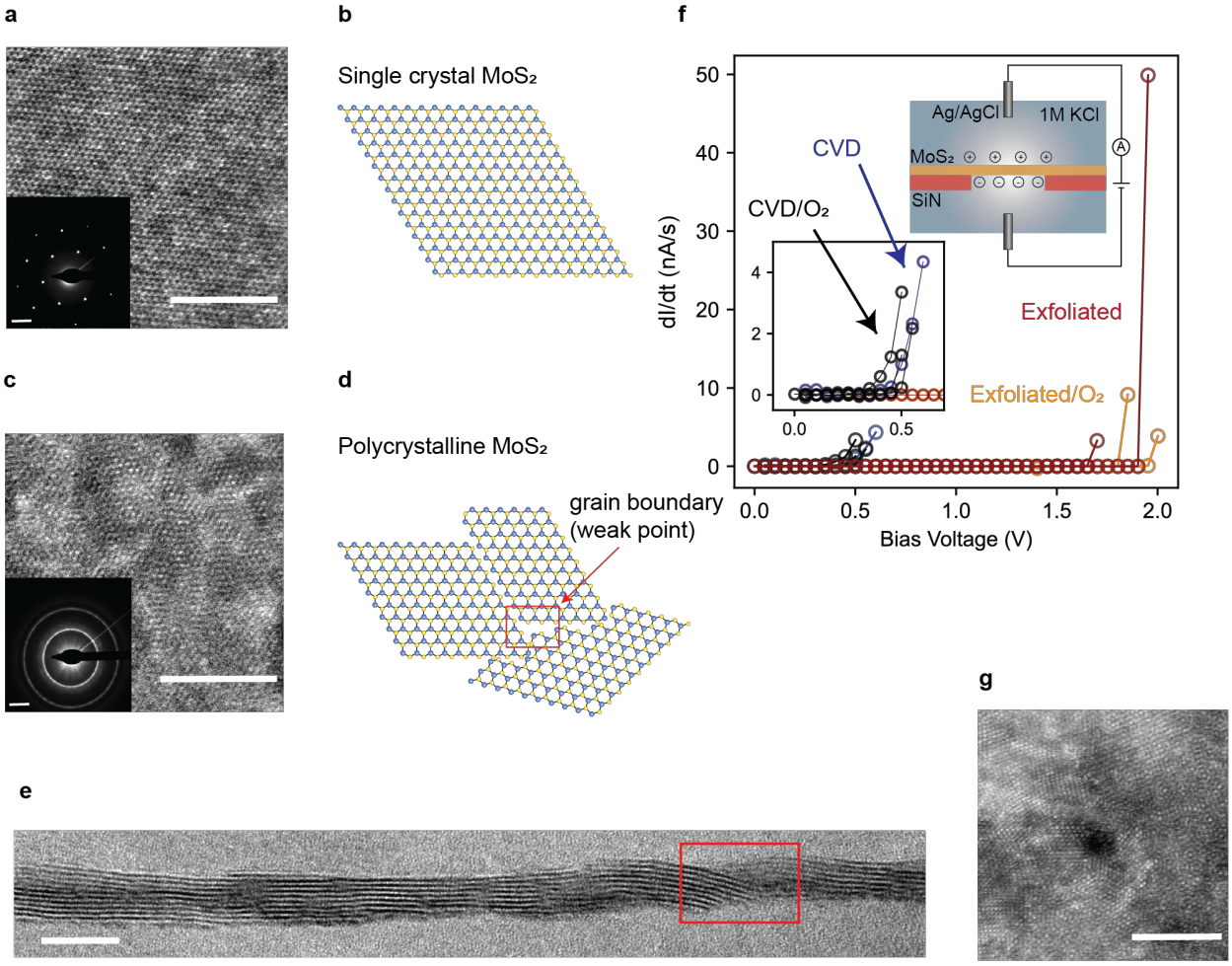

Figure 4.1: Electrochemical pore creation in polycrystalline, few-layer MoS_2 as compared to mechanically exfoliated few-layer single crystals. STEM images and cartoons of few-layer single crystal ME-MoS_2 (**a**-b) and polycrystalline CVD-MoS_2 (**c**-**d**) with diffraction patterns inset. **e**, Cross-section TEM image of polycrystalline MoS_2, with a grain-boundary marked in red. **f**, Change in ionic current for a given (constant) bias voltage applied across the membrane. Device schematic is inset, showing ion accumulation leading to large electric fields across the membrane. **g**, Polycrystalline MoS_2, after electrochemical etching, showing a single (out of many) 1 nm diameter pore. Scale bars are 5 nm in **a**, **c** and **g**; 2 nm-1 in **a** and **c** inset; and 10 nm in **e**.

by cross-section transmission electron microscopy (TEM) (Fig. 4.1 e). Although chemically active sulfur vacancies exist in ME-MoS_2, they are unlikely to stack vertically from layer to layer and thus cannot enable pore formation in multilayer films[143, 144]. CVD-grown monolayer MoS_2, tested in a previous work[145], has similar behavior to CVD-grown polycrystalline MoS_2, likely because S vacancies accelerate the electrochemical formation of single isolated pores.

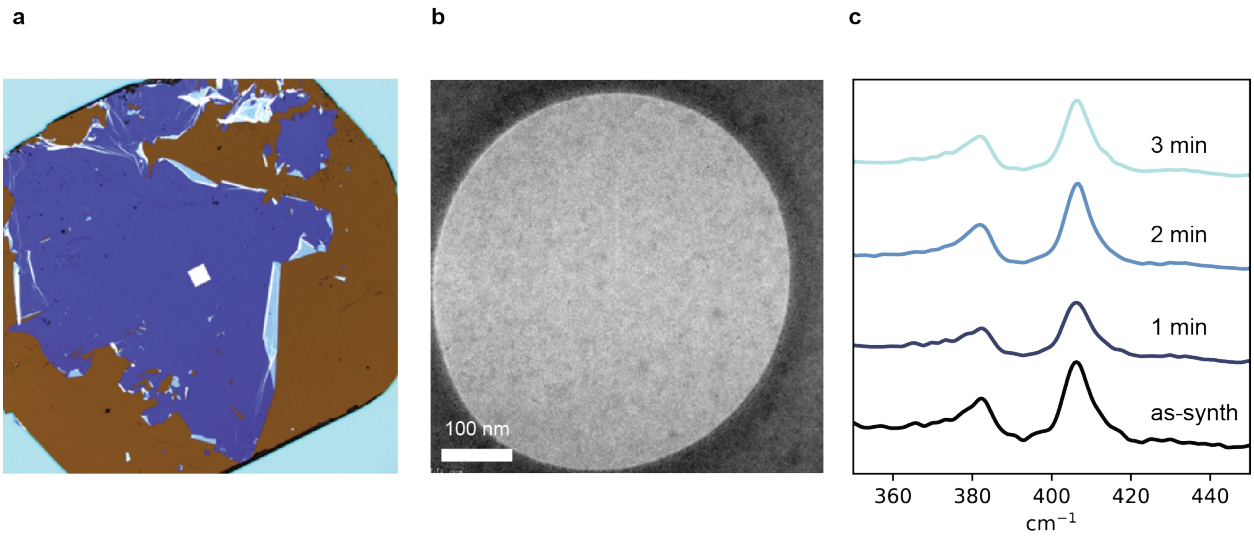

Figure 4.2: Transfer and plasma treatment of CVD-MoS_2 on a SiN chip. **(a)**, Image of a 3 mm SiN TEM grid with a single SiN membrane (white square) in the center. CVD-MoS_2 (blue film) is transferred on the chip and covers the entire SiN membrane. **(b)**, TEM image of CVD-MoS_2 transferred on a single pore drilled in the SiN window. **c**, Raman spectra after remote oxygen plasma treatment of CVD-MoS_2, showing little change in the film integrity. Likely only the first layer of MoS_2 is oxidized[12]

4.2.2 Pore creation in few-layer MoS_2

The SiN chips with MoS_2 films are mounted in a custom flow cell and separate two reservoirs with 1 M KCl electrolyte, electrically connected with Ag/AgCl electrodes (Fig. 4.1 f, inset). The as-transferred MoS_2 films are impermeable to K^+ and Cl^- ions, in agreement with previous work[16, 145, 146](Fig. 4.4). Nanopore creation is induced by the application of a remote electric field across the membrane (the membrane itself is not connected

to the electrical circuit). The bias across the membrane leads to charge accumulation and corresponding membrane polarization[147]. A rapid, but controllable, increase in current is apparent for CVD-MoS_2 at 0.4-0.5 V (inset), whereas a significantly more rapid, and difficult-to-control breakdown occurs for ME-MoS_2 at 1.75-2 V. Partial oxidation of the film does not have a significant effect on the breakdown voltage. Past a threshold voltage, the large interfacial electric field across the membrane induces the removal of atoms from the MoS_2 films resulting in the sub(nm) pores.

For CVD-MoS_2, as the bias voltage exceeds the threshold value of 0.4-0.5 V, the ionic current through polycrystalline MoS_2 increases rapidly and irreversibly (Fig.. 4.1 f, Fig. 4.4). With increasing voltage, the rate of increase rises. The breakdown voltage of ME-MoS_2 is significantly larger than that of CVD-MoS_2 and the high threshold voltage required for ME-MoS_2, results in rapid and unpredictable etching. The minimum rate of current change for ME-MoS_2 (2 nA/s at 1.7 V) is 20 times that of CVD-MoS_2 (0.1 nA/s at 0.4 V), making the process much less controllable. To isolate the role of film morphology over surface chemistry or wettability, we subject both CVD and ME-MoS_2 films to remote O_2 plasma treatment. The O_2 plasma partially oxidizes the top-surface of the MoS_2 films, without destroying the overall integrity (Fig. 4.2)[12]. After plasma treatment, the voltage gap between the threshold of CVD and ME-MoS_2 remains. As shown in Fig. 4.1 g, we find that the polycrystalline MoS_2 films are amenable to the controllable fabrication of 1 nm diameter pores. Using a simple one-pore model (see Section 4.3.1), we determine that, at a threshold voltage of 0.4-0.5 V, the total pore area increases at a rate of $0.2\ nm^2\ s^{-1}$.

The importance of grain boundaries is also confirmed with vertically aligned CVD-MoS_2 films, which are grown using a thicker Mo seed layer (in this case 15 nm)[140]. In the vertically aligned CVD-MoS_2 films, the MoS_2 layers are easily identifiable via TEM imaging (Fig. 4.6). The relative orientations of these layers can then be used to distinguish neighboring grains. After electric field driven pore creation, we find that the MoS_2 degrades predominantly at

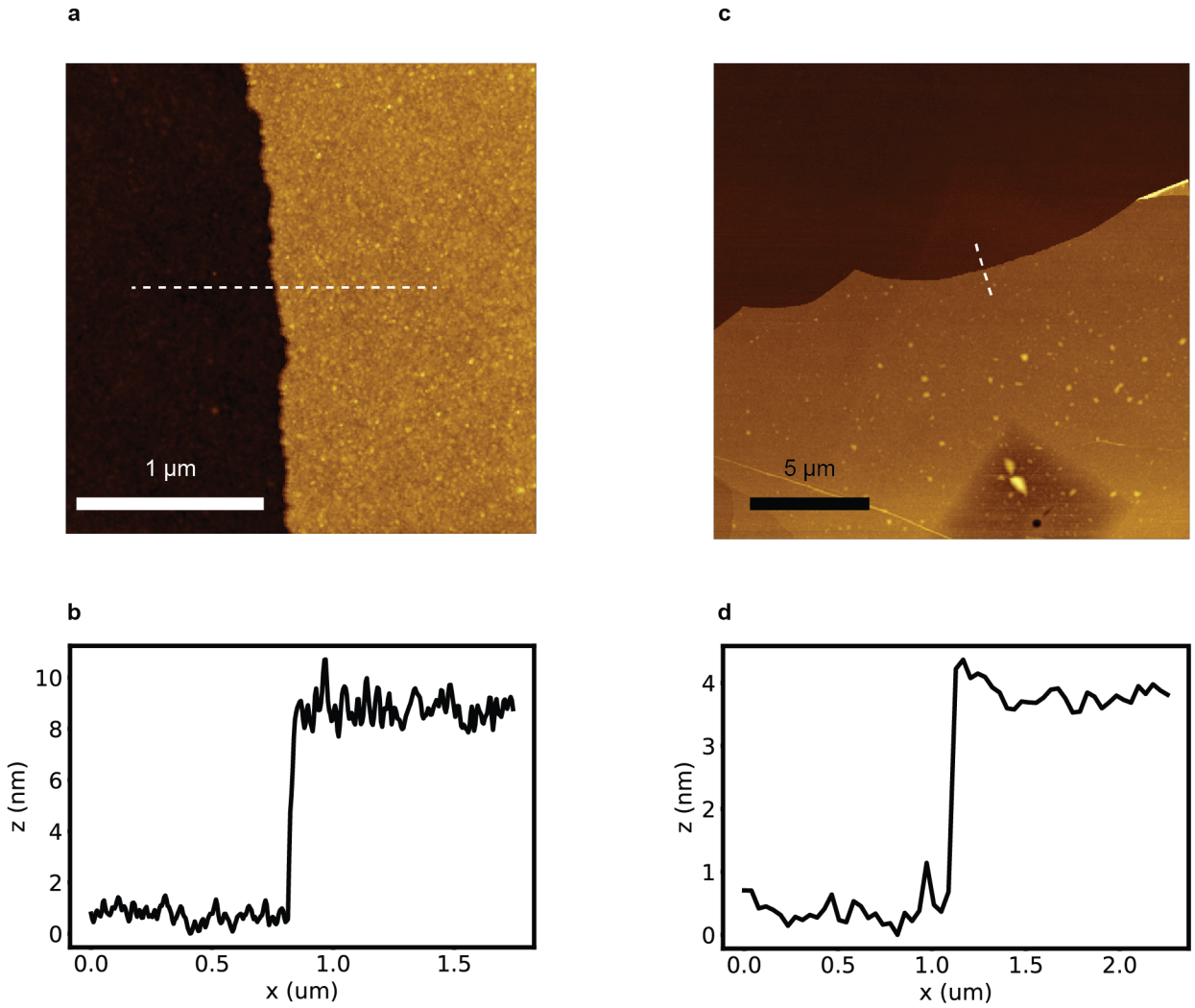

Figure 4.3: Transfer and plasma treatment of CVD-MoS_2 on a SiN chip. **(a)**, Image of a 3 mm SiN TEM grid with a single SiN membrane (white square) in the center. CVD-MoS_2 (blue film) is transferred on the chip and covers the entire SiN membrane. **(b)**, TEM image of CVD-MoS_2 transferred on a single pore drilled in the SiN window. **c**, Raman spectra after remote oxygen plasma treatment of CVD-MoS_2, showing little change in the film integrity. Likely only the first layer of MoS_2 is oxidized[12]

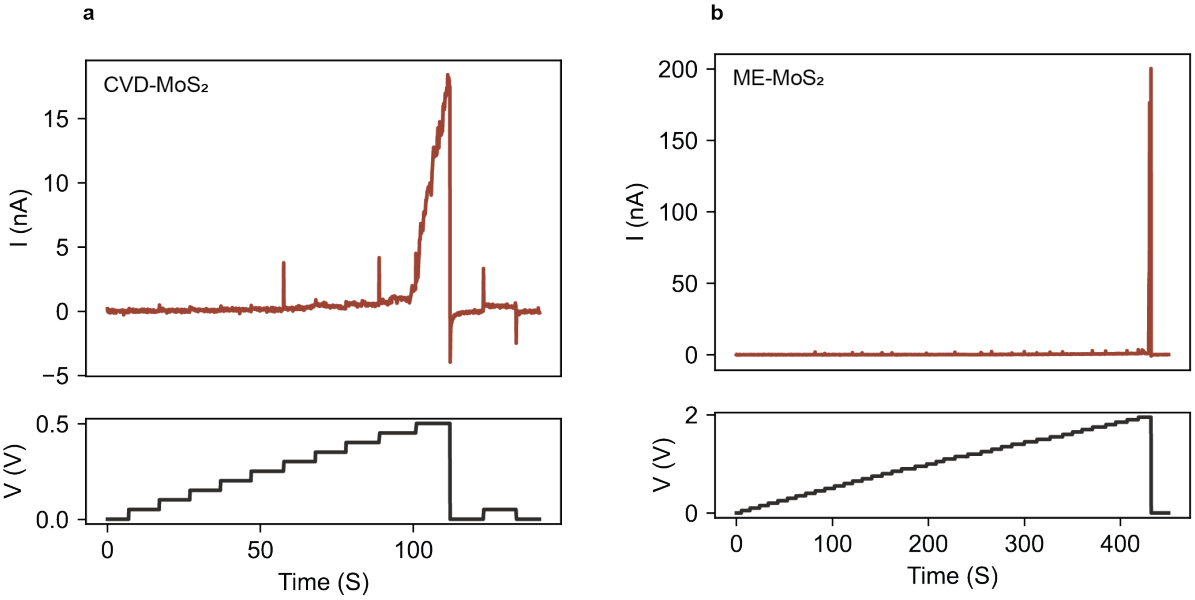

Figure 4.4: Electrochemical pore creation in MoS2 films. Current vs time traces depicting electrochemical pore creation in (**a**) CVD-MoS2 and (**b**) ME-MoS2. Negligible leakage current is detected for CVD-MoS2 before the breakdown threshold of 0.4-0.5 V, at which point the current increases rapidly. For ME-MoS2, that threshold is pushed to nearly 2 V, and the current increases significantly more rapidly (Fig. 4.1).

grain boundaries, further confirming our hypothesis that the exposed atoms at the grain boundaries are more active and have smaller binding energies (Fig. 4.6). We conclude that, in contrast to isotropic etching, our technique leaves the CVD-MoS_2 lattice mostly intact, with pores forming preferentially at grain boundaries.

The dimension of the pores can be controlled via external field strength and application time. In the following, we tune the porosity by applying discrete pulses above the threshold voltage. The morphology of the films after a single 5 ms, 1.5 V pulse and after many 10 ms, 1.5 V pulses differ dramatically, which we characterize with ex situ STEM (Fig. 4.5 a-f). By applying a series of voltage pulses, we increase the porosity, and therefore the conductance, of the film (4.5 g-i). We determine the upper limit of the pore diameter by identifying and then imaging the few largest pores in a given membrane. In Fig. 4.5 a, the largest pores of a film subjected to a single etching step are outlined, and their corresponding high-resolution

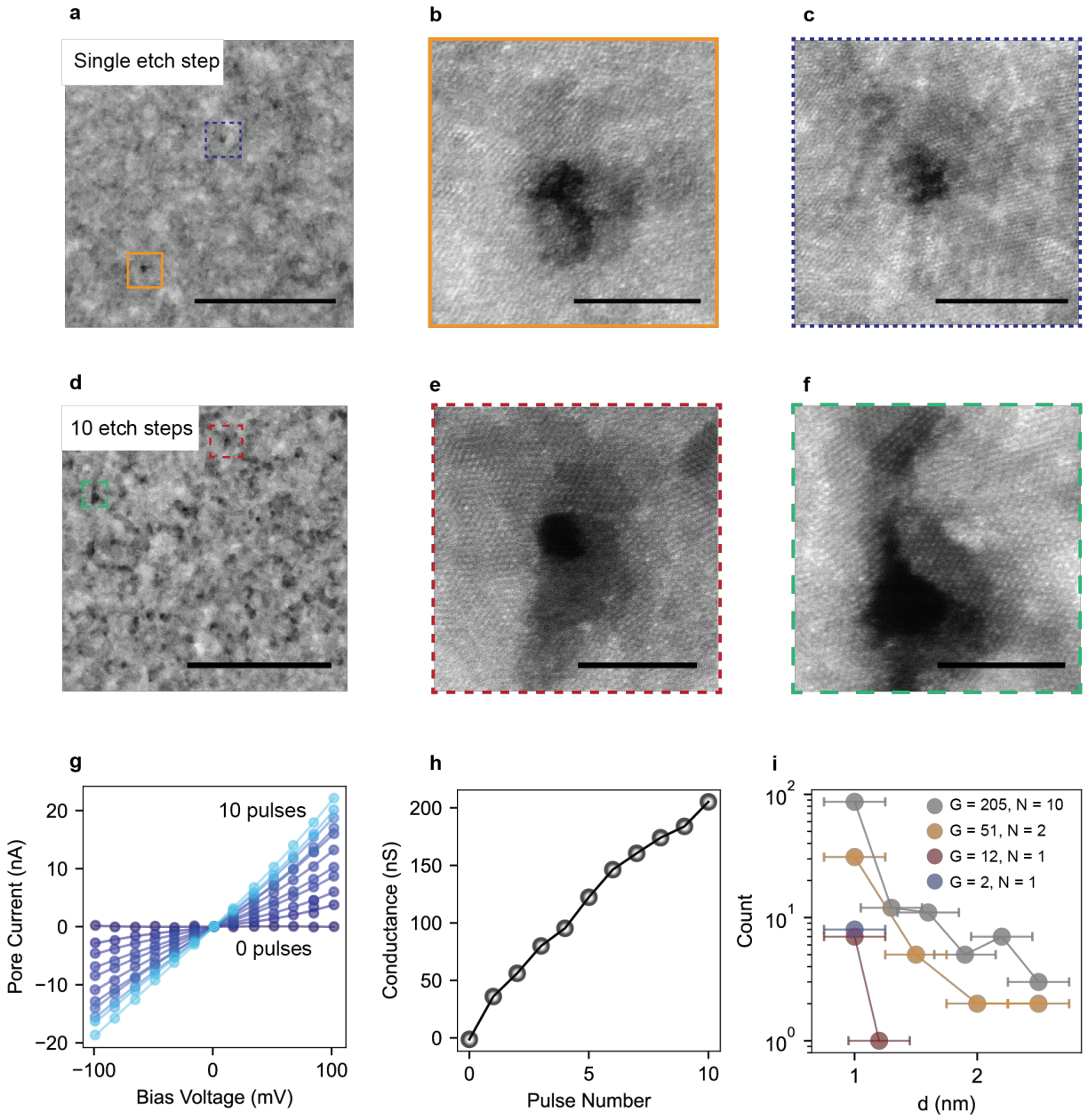

Figure 4.5: Nanopore characterization and in situ tuning. STEM images of porous MoS_2 after (**a**-**c**) a single electrical pulse of 5 ms at 1.5 V and after (d-**f**) ten electrical pulses of 10 ms each at 1.5 V. Only the few largest pores are identified, and images taken, as these pores dominate the ionic current through the membrane. **g**, IV traces and their corresponding conductance values (**h**) taken after each pulse for the film shown in **d**-**f**. **i**, Pore size distributions for four different membranes, with different conductance values (G) after different numbers (N) of 1.5 V, 5-10 ms voltage pulses. Scale bars are 100 nm in **a** and **d**; and 5 nm in **b**, **c**, **e** and **f**.

images shown in Fig. 4.5 b-c, where none exceed 1.5 nm in diameter. This pore size is suitable for the separation of small ions, which we demonstrate in the following section. A film subjected to 10 pulses is shown in Fig. 4.5 d-f, where the largest pore is approximately 4 nm in diameter, which could be suitable for the separation and detection of macromolecules (such as proteins or nucleotides)[148, 149].

4.3 Characterization of nanoporous MoS_2

We calculate pore size distributions for four different membranes via segmentation and thresholding of images of the entire free-standing MoS_2 area (Fig. 4.7). The pore-size distributions (Fig. 4.5 i) for membranes with larger conductance values have more (going from 100 to 2000 pores/mum^2 for 1 to 10 pulses) and larger (from 5 Åto 4 nm) pores, indicating that the applied electric field simultaneously forms new pores and expands existing pores. The measured conductance of KCl through the membranes is in approximate agreement with the expected conductance for a given size distribution (Fig. 4.8), indicating that the membrane is mostly unobstructed, and the ionic current is determined by the porosity of the membrane as opposed to trapped contaminants or bubbles.

4.3.1 Estimating the conductance of a heterogeneous pore array

In the following, we make phenomenological arguments to approximate the conductance of heterogeneous porous array. To estimate conductance of a close-packed, heterogeneous distribution of pores, we modify two models, one of which incorporates the effect of surface charge and the other of access-resistance in a two-dimensional pore array. The conductance of an uncharged, isolated pore with $\frac{d}{L} \ll 1$ (where d is the pore diameter and L the pore length) is proportional to the bulk conductance of the electrolyte k_b, and the ratio of pore area to pore length. When $\frac{d}{L} \approx 1$, however, we must account for access resistance: following Gadaleta *et al.*[151], we add an additional term in series with the pore resistance:

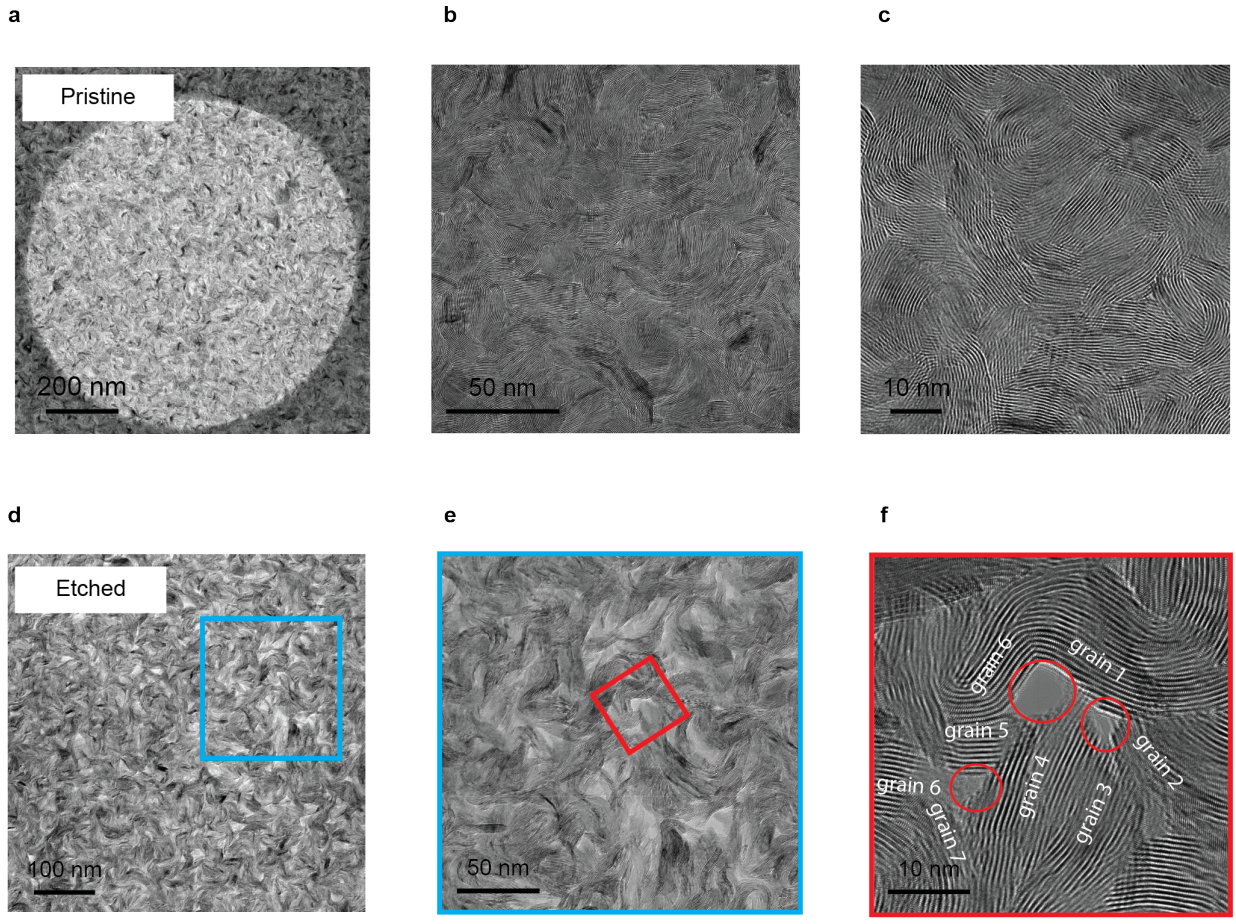

Figure 4.6: Pore generation at grain boundaries in vertically aligned MoS2. Here we show vertically aligned MoS2 before and after electrochemical pore creation. In the pristine sample (**a**-**c**) grains are easily visualized by observing the relative orientation of the MoS2 layers. No discernable gaps or pores are visible between grains. After applying a 1.5 V bias across the membrane for 10 ms in 1 M KCl, the film partially degrades, with pores opening up at the intersections of neighboring grains (**d**-**f**). In**f**, grains are labelled based on the relative orientation of the vertically aligned layers, and pores are circled in red.

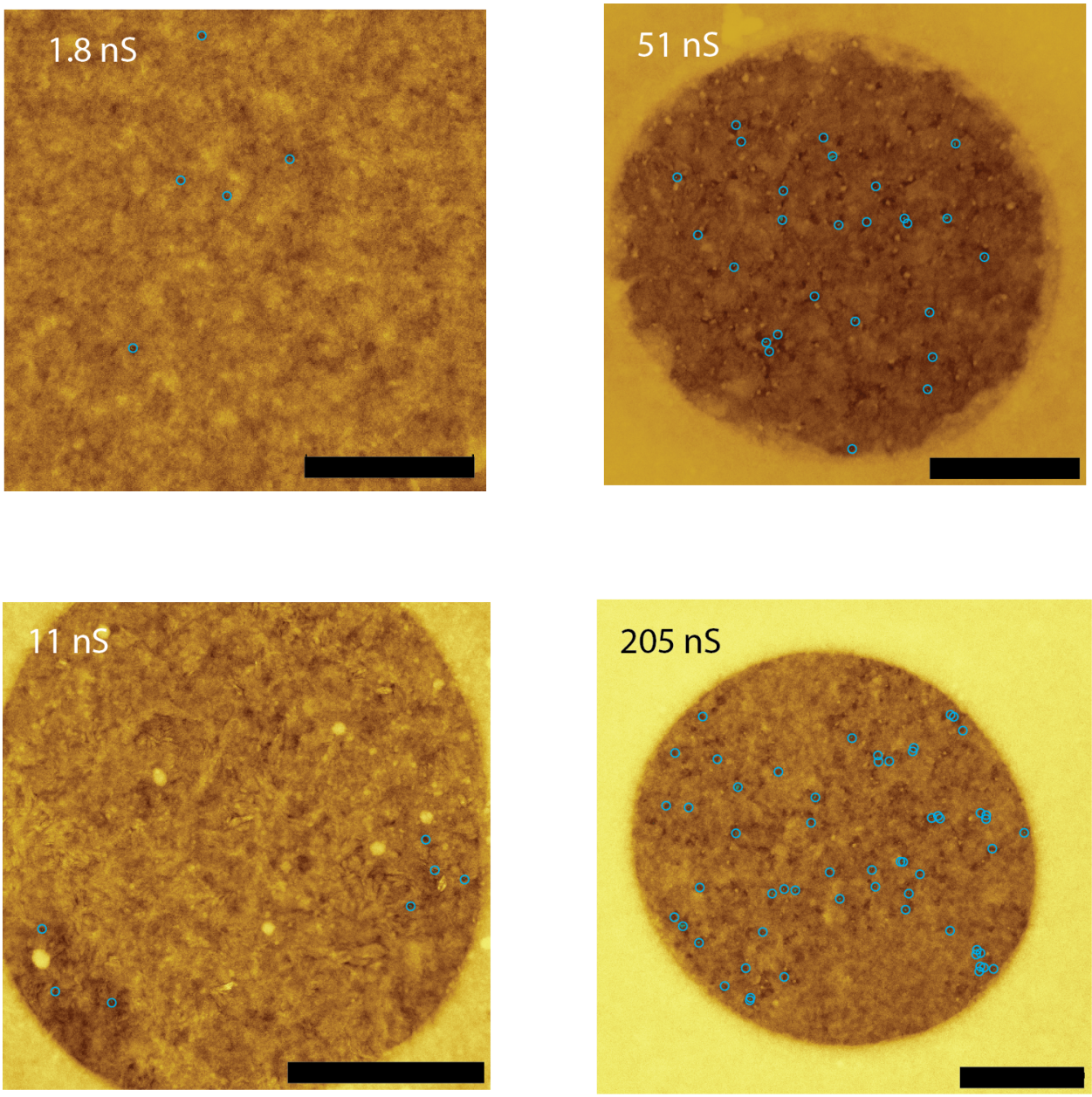

Figure 4.7: STEM images of CVD-MoS2 suspended over SiN pores. The pore size distribution (Fig. 4.5 in the main text) is determined by the segmentation function implemented in Gwyddion[150]. The resulting distribution depends on the threshold as well as the degree of Gaussian smoothing. To accurately set these parameters, we tune them until the size of a select pore matches its high-resolution counterpart, as shown for example in Fig. 4.5 **b-c** and **e-f** of the main text. Identified pores are circled. The scale bars in all images are 100 nm.

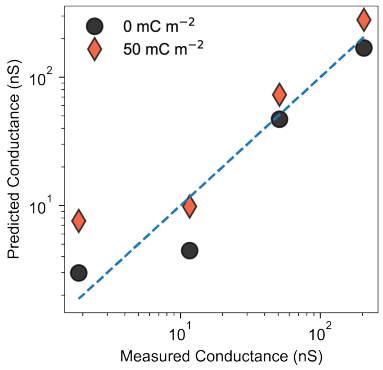

Figure 4.8: Predicted conductance vs expected conductance. Values are calculated from the pore size distribution shown in Fig. 4.5 h of the main text and using Eq. 5 for both 0 and 50 mC m^{-2} against the measured conductance in 1 M KCl. Dashed blue line indicates perfect agreement. Good agreement is observed for the larger pore size distributions; at small pore sizes, the estimation technique begins to diverge from the measured values, likely because the size of a single pixel approaches the size of the nanopores.

$$G = k_b \left(\frac{4L}{\pi d^2} + \frac{1}{d} \right)^{-1} \tag{4.1}$$

Eq. 4.1 neither accounts for pore-pore interactions nor surface charge, theories for both of which have been well studied. Choongyeop et al.[152] derive a relationship between conductance and surface charge that describes the common conductance plateau at low concentrations, wherein the conductance at low concentration is determined by the surface charge and pore geometry, rather than charge carrier number in the bulk:

$$G = k_b \left(\frac{4L}{\pi d^2} \frac{1}{1 + 4\frac{l_{Du}}{d}} + \frac{2}{\alpha d + \beta l_{Du}} \right)^{-1} \tag{4.2}$$

Where l_{Du} is the so-called Dukhin length, which is the ratio of surface to bulk conductivities, and scales linearly with surface charge and inversely with bulk concentration. α and β are geometrical factors and can be approximated to be two here[16, 153]. Gadaleta *et al.* derive a scaling relationship for the conductance of close-packed 2D array of homogeneous pores that effectively increases the access resistance of any given pore in the array by

introducing an effective diameter d_{eff}:

$$G = k_b \left(\frac{4L}{\pi d^2} + \frac{1}{d_{eff}} \right)^{-1} \tag{4.3}$$

$$d_{eff} \approx \frac{d}{1 + \gamma_N \frac{d}{2L}} \tag{4.4}$$

where $\gamma_N \approx \sqrt{N}$ for large N. Here, we note that Gadaleta *et al.* derive the scaling relationship for γ_N by noting that, for large N, the capacitance (and thus the effective diameter of the pore) scales with the lateral size of the array. We account for the variation in pore size diameter by scaling the contribution of each pore by its area. We arrive at:

$$\gamma_{eff} \approx \sum_i \sqrt{\frac{d_i^2}{d_{avg}^2}} \tag{4.5}$$

Noting that the second term in the parentheses of Eq. 4.2 accounts for access resistance, we can combine Eq. 4.2 and 4.4 to arrive at an approximate relationship between the conductance and pore size distribution for a tightly packed and large array of heterogeneous pores:

$$G = \sum_i G_i \approx \sum_i k_b \left(\frac{4L}{\pi d_i^2} \frac{1}{1 + 4\frac{l_{Du}}{d_i}} + \frac{1}{d_{eff,i} + l_{Du}} \right)^{-1}, \tag{4.6}$$

$$d_{eff,i} \approx \frac{d_i}{1 + \gamma_{eff} \frac{d_i}{2L}} \tag{4.7}$$

4.4 Methods

4.4.1 MoS_2 synthesis

We follow a standard synthesis procedure for CVD-$MoS_2$42. A Si/SiO2 wafer is diced into pieces, solvent-cleaned, baked at 120 deg. C and plasma treated to remove residual organics

and render the chips hydrophilic. A thin Mo film is deposited using magnetron sputtering (AJA ATC Orion 8 UHV Sputtering System) at 30 W and 1 mTorr with 30 s.c.c.m Ar flow. The deposition rate is determined to be 4 nm min^{-}1 under these conditions. The Mo film is then sulfurized via chemical vapor deposition. A quartz boat with sulfur powder (Sigma Aldrich, 99.98% trace metals basis) is loaded immediately upstream of the oven with the Mo film in the center; a separate heat belt is used to control the sulfur temperature. The one-inch tube furnace is pumped down and purged multiple times with Ar gas. The Ar flow rate is then held at 50 sccm and the pressure is 1 Torr. The furnace is heated to 300 deg. C and held for one hour, after which it is ramped to 750 deg. C at 15 deg. C min^{-}1. The heating belt upstream of the furnace is ramped quickly to 140 deg. C. to vaporize the sulfur. After 10 min, the oven and heating belt is cooled down naturally.

4.4.2 MoS_2 transfer onto SiN chips

A thin layer of PMMA (Nano 495) is spin-coated (3000 rpm for 1 min) on a freshly synthesized MoS_2 thin film then baked on a hot plate set at 150 deg. C. A diamond-tipped scribe is used to etch 1 mm squares in the polymer coated film. A portion of the chip is then submerged slowly in water, at which point the MoS_2 film easily delaminates from the SiO_2 chip. We transfer 1:1 EtOH:H_2O into the water containing the floating MoS_2 films, then scoop the film with a 3 mm SiN TEM grid (Norcada) with a single 300-500 nm diameter hole drilled via focused ion beam in the center. The chip is left to dry, then cleaned in acetone held at 60 deg. C for 12 hours, then IPA and ultrapure water and blow dried with N2.

4.4.3 Mechanical exfoliation and transfer onto SiN chips

We follow a hybrid of procedures outlined in previous work to transfer to mechanically exfoliated MoS_2[139, 154]. Few-layer MoS_2 crystals (SPI supplies) are thinned using Nitto blue tape. PDMS (Sylgard 184 elastomer), stamps are prepared on clean Si wafers, then

peeled off and transferred to a glass slide, with the side facing the Si facing up. The flakes are transferred to the PDMS and imaged. Using a micrometer, we adjust the position of the stamp to align with the SiN window while imaging using an optical microscope (Olympus DSX1000). The PDMS is brought down to contact the SiN chip, then very slowly raised, leaving the target flake covering the SiN pore.

4.4.4 Pore creation and ion conductance tests

All buffers and electrolytes are degassed and <20 nm filtered with Whatman Anotop syringe filters (Millipore Sigma). The SiN chip is loaded into a custom-built flow cell with reservoirs bridged by freshly chlorinated Ag/AgCl electrodes and is wetted with EtOH. We then exchange the buffers with 4:1, 1:1, 1:4, and 0:1 EtOH:H_2O. After 20 min, we slowly run 1M KCl through both sides of the reservoir until the solution is entirely exchanged. The electrodes are connected to a home-built amplifier with which we record current-voltage traces. To open pores, the voltage is ramped with 15-50 mV steps, brief 5-10 ms, 1.5 V pulses are applied across the film. After testing, the chip is rinsed with water, then solvent-cleaned again to remove adsorbed organics.

4.4.5 Characterization of MoS_2 Film

Raman spectroscopy is carried out using a HORIBA LabRAM HR Evolution Confocal Raman Microscope. Scanning electron microscopy is performed using a Carl Zeiss Merlin SEM. To perform STEM measurements, we use a JEOL JEM-ARM200CF; and for TEM measurements, a Tecnai F30 microscope. AFM is carried out using an Asylum Research Oxford Instruments Cypher ES AFM.

CHAPTER 5

ION SELECTIVE TRANSPORT IN NANOPOROUS FEW-LAYER MOS_2

5.1 Introduction

2D material membranes have yet to demonstrate significant selectivity for different cations, especially of the same charge, even though they are excellent at separating cations from anions[5, 16, 37, 121, 127, 155]. Without adding additional active elements, such as conical nanoporous substrates[156] or nanobubbles[135], the selectivity (the higher permeance of one ion relative to all others) of nanoporous 2D material membranes for monovalent ions (K^+, Li^+, Na^+ and Cs^+) has remained around two (after accounting for trends in bulk mobility)[14, 146, 157]. Here, we use our nanoporous few-layer MoS_2 membranes as ionic sieves, achieving high selectivity while retaining a relatively large absolute conductance.

Existing methods and starting material design have limited the performance of nanoporous membranes. Furthermore, these methods have been applied to only monolayer (never few-layer) membranes, limiting the intrinsic selectivity. Computational efforts also have mainly focused on the transport properties of ions in monolayer membranes and have identified the effect of ion dehydration as the primary driver of selectivity[21, 43]. There has been little work studying the interplay between ion transport and water dynamics, however, which we find is one of the driving factors for monovalent cation selectivity in our few-layer nanoporous films.

Owing to its combination of high surface charge density, tight pore-size distribution, and nm-scale thickness, MoS_2 nanoporous membranes demonstrate selective transport of both monovalent and divalent cations. The level of ion selectivity of nanoporous, few-layer MoS_2 membranes is among the highest for ultrathin solid-state membranes to date, compared with reported membranes with similar absolute conductance. We use classical molecular

dynamics (MD) simulations to elucidate the mechanism of the experimentally measured ion selectivity. We find that the unique interactions between cations and the sluggish water confined to the pore, as well as cation-anion interactions combine to result in qualitatively different transport behavior for KCl, NaCl, LiCl and $MgCl_2$ through nanoporous MoS_2. Such behaviors are suppressed in monolayer films, explaining the high selectivity measured in this study compared to existing literature using monolayer graphene and MoS_2 membranes[14, 146, 157].

5.2 Ion transport characterization

5.2.1 Ion selectivity

The size of the MoS_2 nanopores ($\sim$ 5 Å- 4 nm) fabricated here are commensurate with the diameter of hydrated ions ($\sim$ 7-9 Å). As such, the unique solvation characteristics of ions are paramount in determining their dynamics confined in the MoS_2 membrane [22]. The transport behaviors of five different salts (1 M KCl, NaCl, LiCl, $MgCl_2$, and $CaCl_2$) are probed by measuring current-voltage traces for a given membrane. We find that, across all 15 devices tested for KCl/$MgCl_2$ selectivity, the conductivity ratio between KCl and $MgCl_2$ increases dramatically with membrane resistance to KCl (Fig. 5.1 a, Table 5.1), and correspondingly with respect to decreasing pore size. By comparing the conductance values of the 15 devices tested for KCl/$MgCl_2$ selectivity to the corresponding pore size distributions calculated separately in Fig. 4.5, we determine that past a maximum pore size of $\sim$ 3 nm, the selectivity approaches unity.

We test the conductance of the entire suite of salts in a smaller subset of three membranes, measuring multiple current-voltage traces for each salt (Fig. 5.1 b). Again using Fig. 4.5 as a reference, we conclude that the pores are in the 5 Å-2 nm range. For each membrane, we measure the conductance going from small to large hydration enthalpy (K^+ to Mg^{2+}), then back from large to small (Mg^{2+} to K^+) to avoid artifacts from slow changes in conductance due to pore fouling (Fig. 5.4). We find that the conductance of all salts through the MoS_2 nanopores are suppressed relative to KCl (Fig. 5.1 c).

We define the pore-induced selectivity, accounting for differences in bulk conductivity, as

$$S_{p,i} = \frac{G_i}{G_{\text{kcl}}} \frac{k_{\text{kcl}}}{k_i} \tag{5.1}$$

where G_i and G_{kcl} are the measured conductance of a given salt and of KCl, respectively; and k_i and k_{kcl} are the bulk conductance of a given salt and of KCl, respectively. Even after

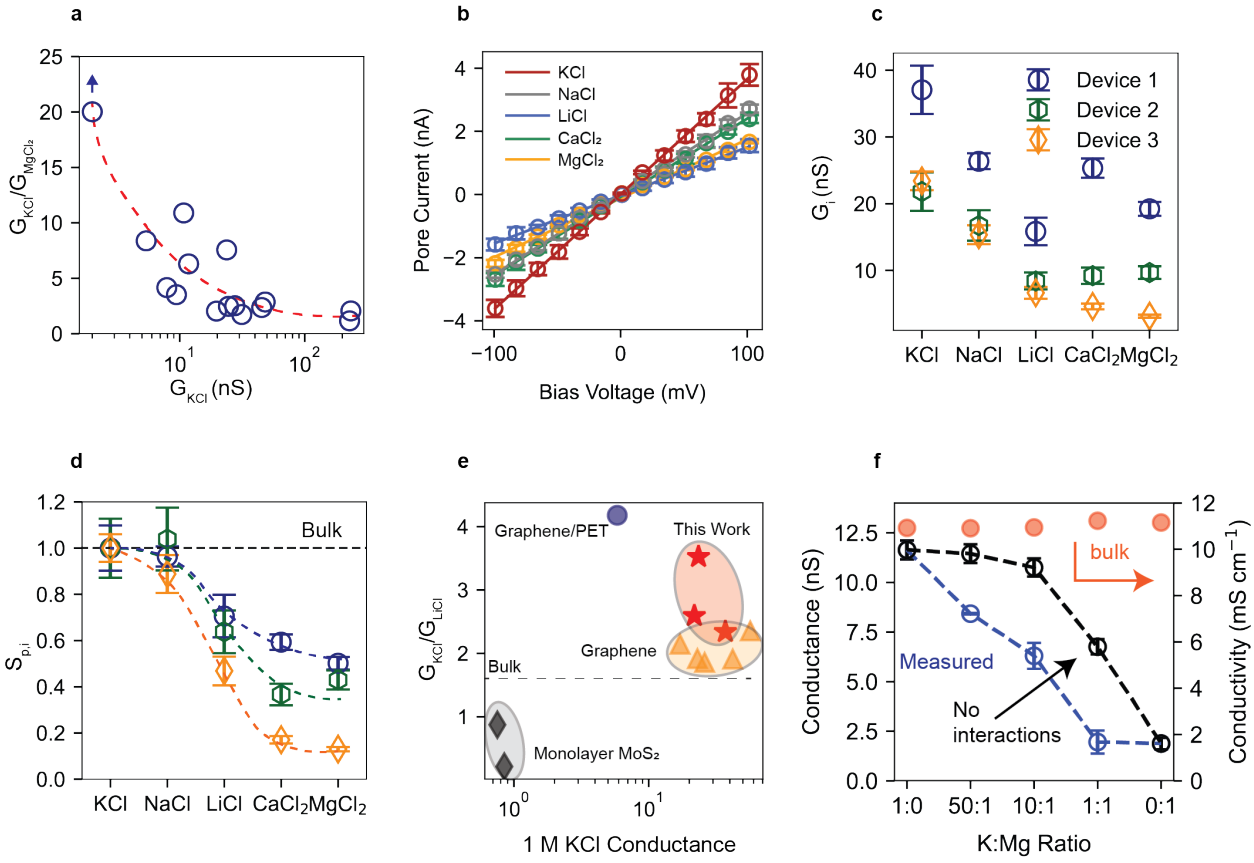

Figure 5.1: Ion transport measurements in MoS_2 nanopores. a, $KCl/MgCl_2$ selectivity for all 15 devices tested, plotted against membrane resistance to KCl. The dotted red curve is a guideline. The $MgCl_2$ conductance for the datapoint with the highest $KCl/MgCl_2$ selectivity is below our detection limit, and thus we can only establish a lower bound. **b**, Representative IV curves used to determine the membrane conductance values (this set corresponds to Device 1 in **c**. **c**, Ion conductance values for three devices, showing enhanced conductance of KCl relative to all other salts, even after (**d**) scaling using Eq. 5.1. **e**, Unnormalized conductance ratio of KCl and LiCl plotted against conductance of 1 M KCl through existing nanoporous 2D material membranes (see Supplementary Table 2 in Hoenig *et al.* for references and precise values[29]). **f**, Interactions between KCl and MgCl**2**. Blue curve shows measured conductance values as a function of K^+ to Mg^{2+} molar ratio. Black curve shows the predicted values, assuming KCl and $MgCl_2$ do not interact with the other cation or the membrane, calculated using the pure KCl and pure $MgCl_2$ conductance measurements. Red markers show that the bulk conductance changes $< 5\%$ as a function of the K^+ to Mg^{2+} molar ratio.

accounting for the contribution of the bulk conductance, the selectivity remains (Fig. 5.1 d). We emphasize in particular the selectivity between the monovalent salts KCl, NaCl, and LiCl, which is among the highest in ultrathin 2D material membranes to date (Fig. 5.1 e). Furthermore, due to the high density of nanopores in the polycrystalline MoS_2 films, the absolute conductance is a factor of > 2 higher than membranes with the same selectivity. This enhancement may also be a result of the fact that, because we test few-layer as opposed to monolayer 2D material membranes, a similar selectivity can be achieved with larger pore diameters, a point which we corroborate using MD simulations in the following section.

Sample	G_{MgCl_2} (nS)	G_{KCl} (nS)	Pulse Voltage (V)	Pulse Time (ms)	Pulse Number	Mo Seed (nm)
1	10.96	27.63	1.5	25	1	2
2	197.64	228.54	1.5	50	2	2
3	18.19	31.4	1.5	12.5	1	2
4	9.68	19.71	1.5	10	2	1.75
5	3.15	23.8	1.5	10	1	1.75
6	19.23	45.34	1.5	10	1	1.75
7	9.97	24.58	1.5	5	1	1.75
8	0.99	10.78	1.5	5	1	1.75
9	16.9	48.32	1.5	5	1	1.75
10	1.9	7.9	1.5	5	1	1.75
11	0.645	5.4	1.5	5	1	1.75
12	<0.1	2	1.5	5	1	1.75
13	2.68	9.43	0.4-0.5	NA	NA	1.75
14	114	234	0.4-0.5	NA	NA	1.75
15	1.875	11.805	0.4-0.5	NA	NA	1.75

Table 5.1: Devices tested for $KCl/MgCl_2$ selectivity. Test conditions and results for 15 different devices, used to measure the selectivity of KCl and $MgCl_2$. Samples were collected over the course of one year. Different film thickness and pulse frequencies were used, although in the ranges tested here there was little effect on the results.

5.2.2 Ion-ion interactions

It is well-established that under nm-scale confinement, ion-ion correlations play a large role in the transport behavior of charged species. We cannot assume, therefore, that the difference in conductance between salts is a function of the cation mobilities alone. To isolate the relative contributions of cation and anion to the total current, we measure the membrane

potential with 1 M and 0.1 M electrolytes in the two reservoirs, which is easily translated into the transference number, t_+ (Section 5.2.3). For monovalent ions, the current is dominated by the cation ($t_+ \sim 0.8$) and to similar degrees for KCl, NaCl, and LiCl (Fig. 5.2). It is surprising that the cation/anion selectivity is similar for LiCl and KCl, given the lower overall conductance of LiCl. The puzzle is resolved however, when considering that as the nanopore is occupied by cations the negative surface charge is partially screened, reducing the energy barrier for anions: a higher concentration for K^+ inside the nanopore results in a higher concentration of Cl^-. This theory is verified in the following section using MD simulations. The transference number for the divalent ions ($t_+ \sim 0.3$) is suppressed relative to the monovalent ions. The mechanism of this qualitative shift is elucidated by observing that the presence of Mg^{2+} in a mixed KCl/$MgCl_2$ solution suppresses the conductance of K^+ (Fig. 5.1 f), indicating that Mg^{2+} is adsorbed on or is stuck inside the MoS_2 membrane. The adsorbed cation reduces the magnitude of, or possibly inverts, the intrinsically negative surface charge, creating a more (less) favorable environment for the anion (cation).

5.2.3 Calculation of transference number

To determine the transference number for a given salt solution, we measure the current voltage trace (Fig. 5.3) and extract the zero-current voltage. We account for electrode potential difference, given by the Nernst equation:

$$V_n = \ln \Delta \frac{RT}{nF}, \tag{5.2}$$

where *Delta*is the concentration ratio between the two sides of the reservoir, and n is unity (the number of electrons exchanged in the silver chlorination/de-chlorination half-reactions). The membrane voltage is then $V_m = V_0 - V_n$. The mobility ratio is determined through the Henderson equation[13, 158]:

$$\frac{\mu_+}{\mu_-} = -\frac{z_+}{z_-}\frac{\ln\Delta - z_- FV_m/RT}{\ln\Delta - z_+ FV_m/RT} \tag{5.3}$$

Using the relation ($J_i = z_i c_i \mu_i E$) and noting that the product $z_i c_i$ as well as E are equal for cation and anions for both mono and divalent salts, the transference number is simply:

$$t_+ = \frac{1}{1 + \frac{\mu_-}{\mu_+}} \tag{5.4}$$

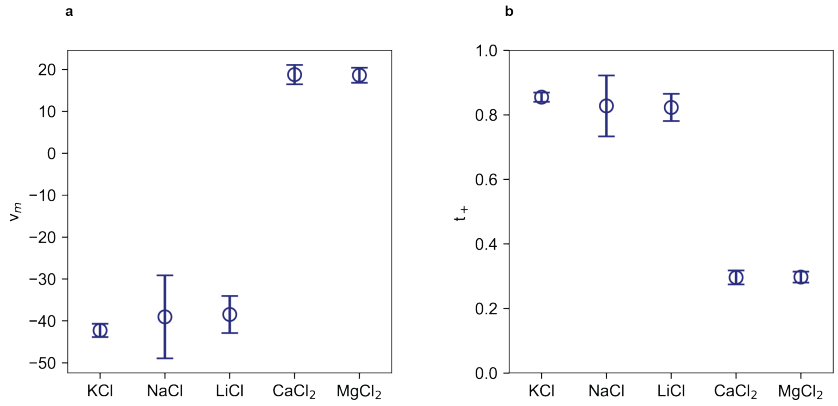

Figure 5.2: Membrane potential and transference number for various salts. **a**, Membrane potential for salts tested in 1 M/0.1 M reservoirs (after the electrode potential is subtracted). We note the qualitative difference for divalent salts compared to the monovalent salts tested in this study. **b**, Transference numbers in a single membrane calculated from a showing relatively stable values for monovalent but a precipitous drop-off for divalent cations. The transference number is 0.8 for monovalent salts but is < 0.5 for divalent salts, indicating the importance of both size exclusion and electrostatic effects in the pore.

5.3 MD simulations of ion transport

To further understand the dynamics of ions and unveil the origin of ion selectivity in the MoS_2 nanopores, we carry out classical MD simulations. In the simulations discussed below, two reservoirs with equal concentration of 1M KCl, NaCl, LiCl or $MgCl_2$ are separated by a single or six-layer (6L) MoS_2 film through which a 1 or 2 nm pore is drilled (Fig. 5.5 a-c). The pore is terminated by both Mo and S atoms to approximate the most likely pore

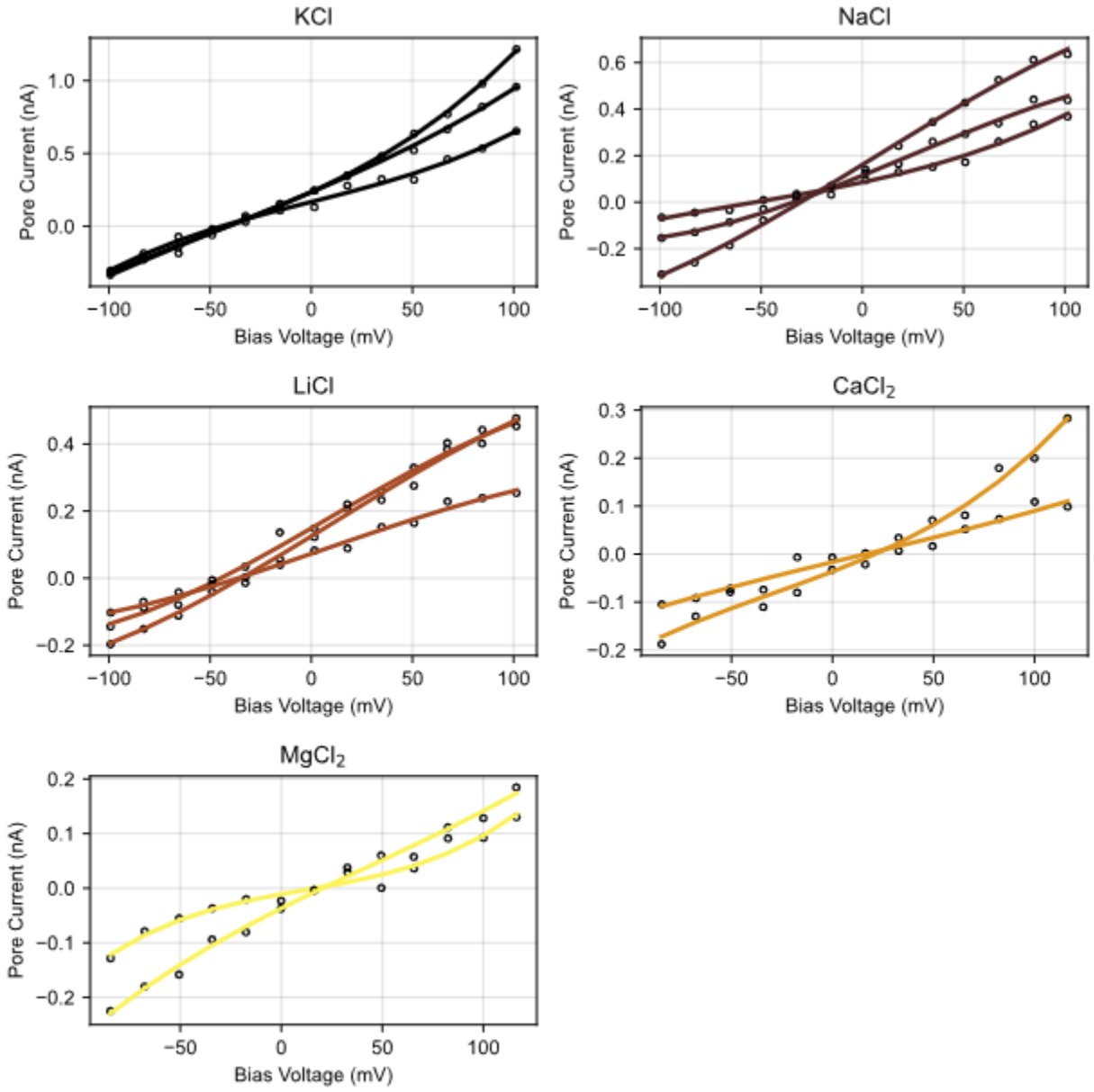

Figure 5.3: Asymmetric electrolyte tests. Current-voltage curves with an asymmetric electrolyte (1 M/0.1 M) in the two reservoirs. The Nernst potential has been subtracted, so the membrane potential is found by measuring the x-intercept. Note the instability in the conductance is likely due to partial pore fouling during repeated testing and cycling through different salts.

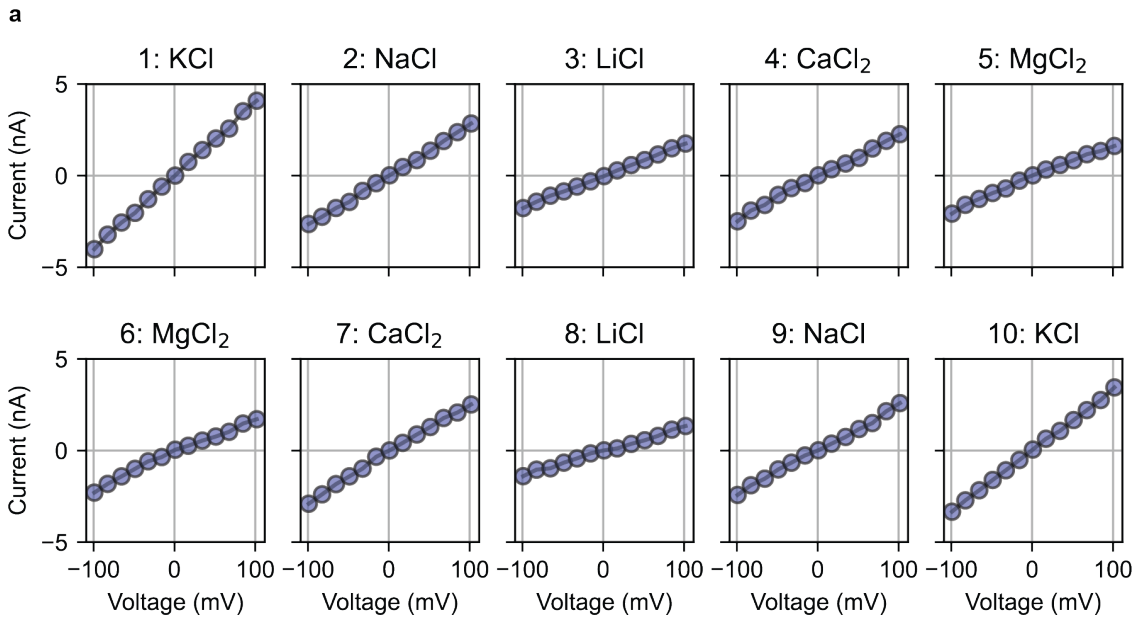

(a) Device 1

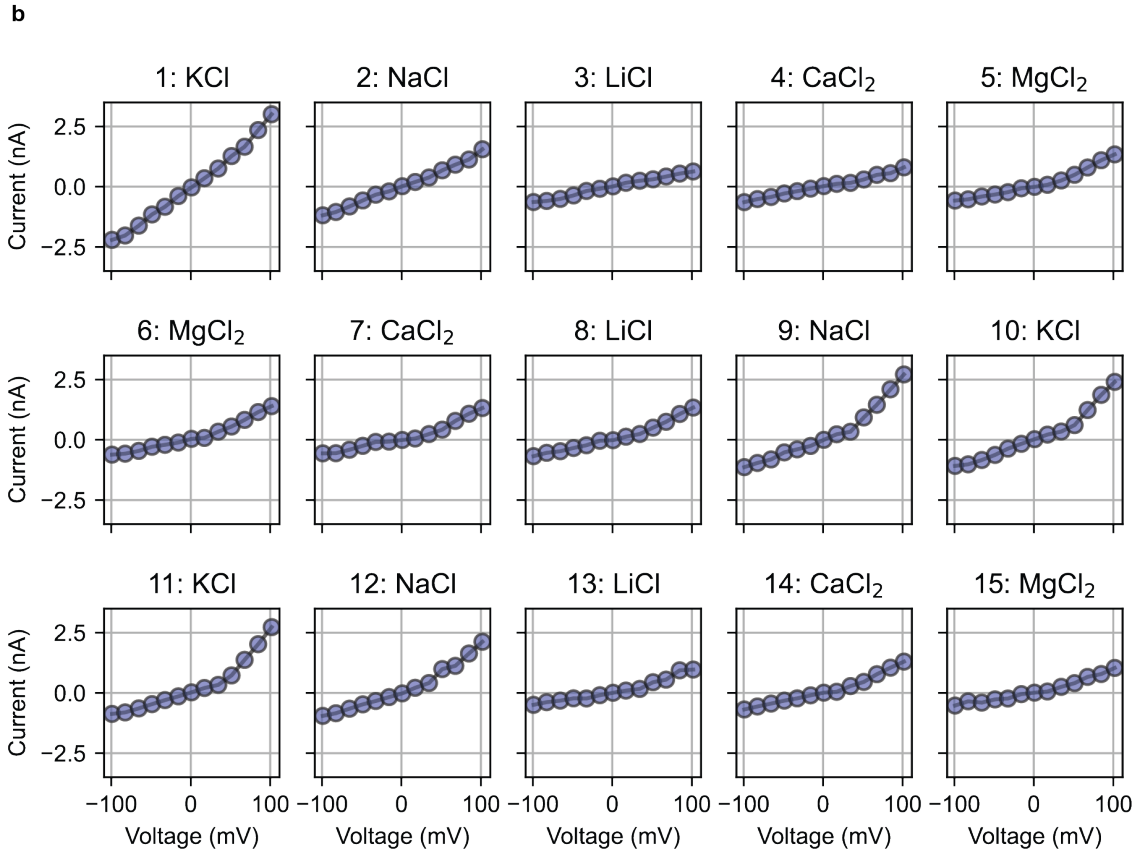

(b) Device 2

Figure 5.4: IV curves for all tested salts (continued on the next page).

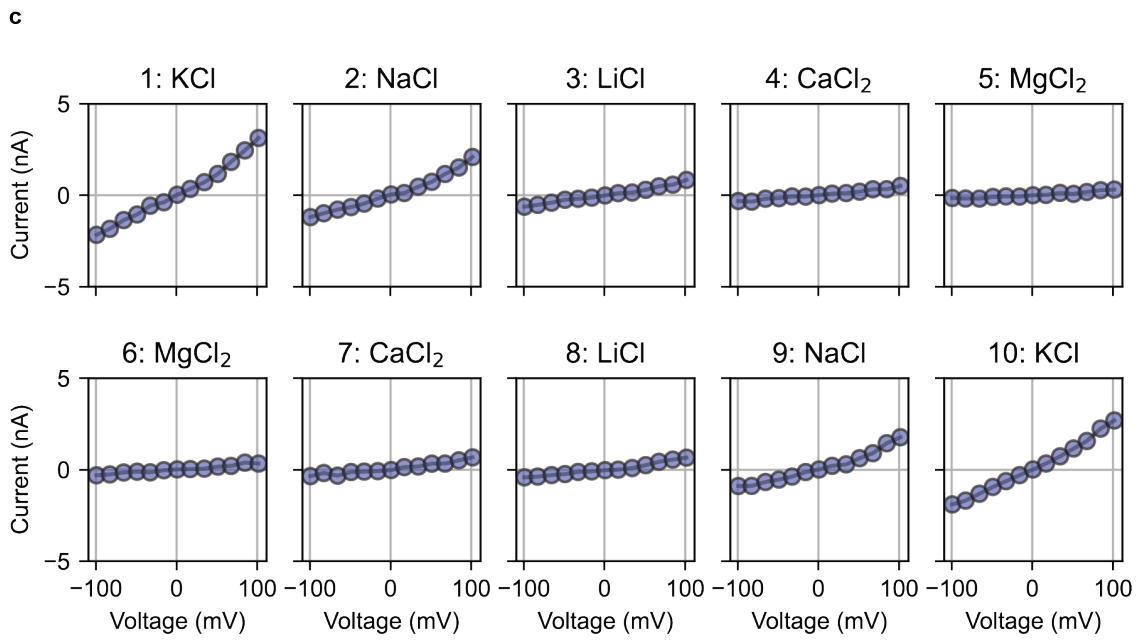

(c) Device 3

Figure 5.4: (continued) I-V traces in 1M salts. Traces are shown for device 1 (**a**), device 2 (**b**) and device 3 (**c**), for which average selectivity data is shown in Fig. 5.1 of the main text. Each trace is an average of multiple ($\gg 3$) scans. Data is taken in increasing numerical order (KCl to $MgCl_2$ and $MgCl_2$ back to KCl.

configuration, as was recently measured experimentally[129], and a partial charge is added to all terminating atoms to fix the surface charge at 50 mC m^{-2}[16]. A constant electric field is applied perpendicular to the membrane to generate net ion flux through the film. Further simulation details can be found in Section 5.6.

We first calculate the total ionic current for each salt through 6L-1nm, 6L-2nm and 1L-1nm MoS_2. After accounting for the bulk conductivity using Eq. (1), the transport of KCl through 6L-1 nm MoS_2 is significantly enhanced over LiCl ($S_p = 0.67$) and $MgCl_2$ ($S_p = 0.54$) and is slightly higher than NaCl ($S_p = 0.92$), in qualitative agreement with our experimental results (Fig. 5.5 d). We see no such selectivity for either 6L-2 nm MoS_2 or, surprisingly, 1L-1 nm MoS_2.

The ionic current is proportional to the average drift velocity of the ions and the total ion concentration. Analyzing 6L-1 nm MoS_2, we observe that the average velocities of Li^+

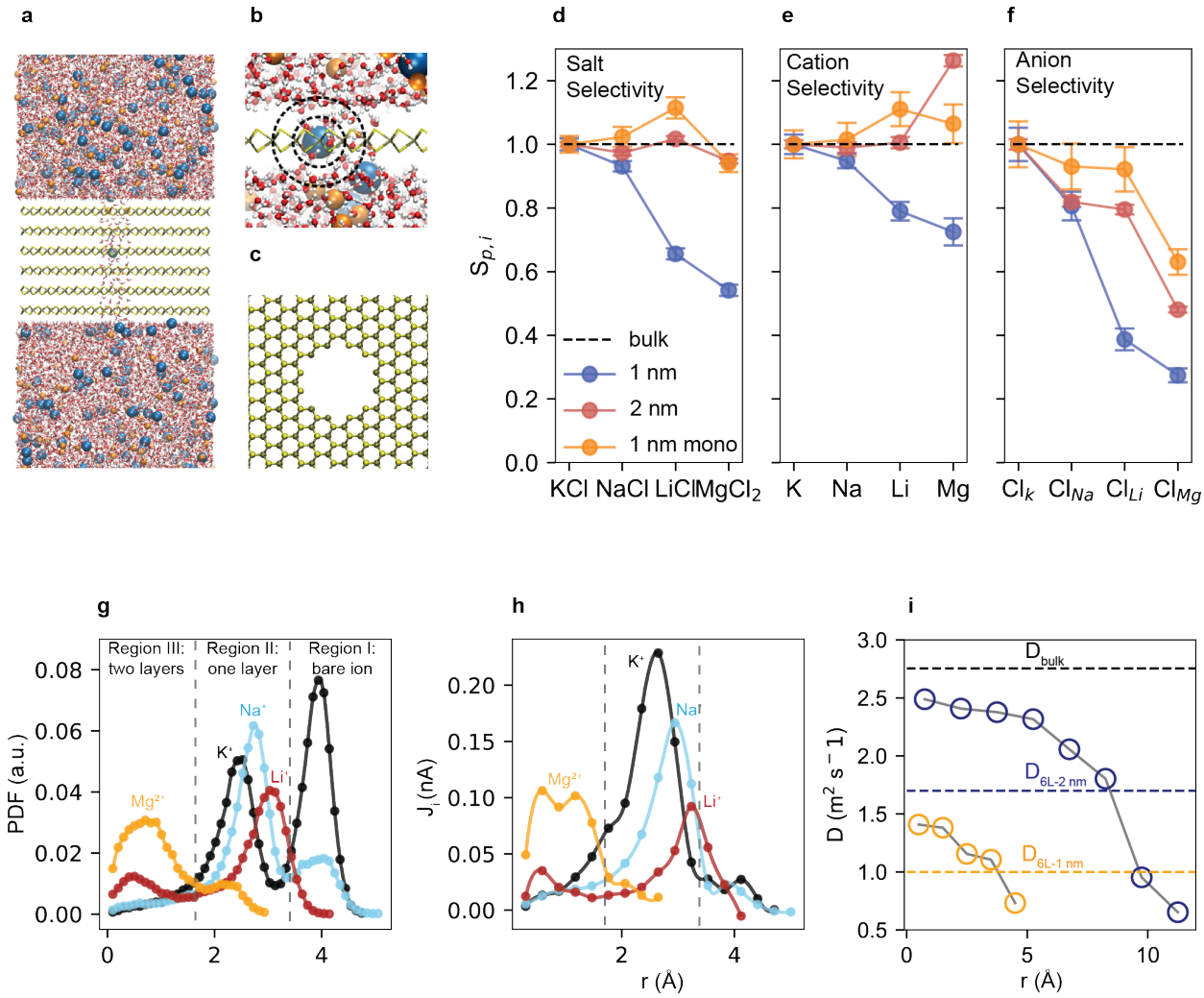

Figure 5.5: MD simulation results for ion transport in MoS_2 nanopores. MD simulation snapshots of a (**a**) 6L-1nm MoS_2 film and (**b**) 1L-1nm film separating two 1 M KCl reservoirs. Dotted black lines indicate locations of the first and second solvation shell of a Mg^{2+} ion. The second solvation shell spans the length of the pore. A single pore (**c**) is drilled in the center of the all MoS_2 films. **d**, Ion selectivity for KCl, NaCl, LiCl and $MgCl_2$ for 6L-1nm, 6L-2nm and 1L-1nm MoS_2. Decomposition of the total current into its (**e**) cationic and (**f**) anion components. Cations are normalized to their bulk mobility values, and anions scaled by their total concentration (a factor of two higher for $MgCl_2$). **g**, Probability density functions, normalized to K^+, for each cation inside the 6L-1nm pore. Three distinct regions are apparent, corresponding to different hydration levels. **h**, Cationic current as a function of radial position for all four cations. The current is dominated by the ions in the one-layer water region, even though a higher concentration of cations for K^+ can be found directly adjacent to the pore. **i**, Radial profiles of the water diffusion coefficient in the 6L-1nm and 6L-2 nm pores (without the presence of an applied bias or ions) as compared to the diffusion of water in the bulk reservoir. The diffusion of water in both pores is suppressed, especially near the pore edges, but is significantly more suppressed for the 6L-1nm pore.

Total				Cation						Anion					
Pore		Current (nA)		Velocity (m/S)		Concentration (M)		Velocity (m/S)		Concentration (M)		Velocity (m/S)		Concentration (M)	
6L-1 nm	KCl	0.96	0.02	0.65	0.02	8.01	0.17	1.079	0.003	0.31	0.02	-5.03	0.22	0.804	0.003
	NaCl	0.67	0.01	0.42	0.01	7.36	0.22	0.753	0.002	0.25	0.01	-5.67	0.28	0.59	0.002
	LiCl	0.39	0.01	0.27	0.01	6.56	0.28	0.551	0.002	0.12	0.01	-3.76	0.32	0.427	0.002
	MgCl2	0.5	0.02	0.34	0.02	4.44	0.23	0.499	0.002	0.17	0.01	-3.23	0.22	0.686	0.002
6L-2 nm	KCl	8.73	0.06	5.41	0.07	22.46	0.13	0.552	0.001	3.32	0.05	-20.35	0.19	0.374	0.001
	NaCl	6.37	0.06	3.65	0.06	16.66	0.13	0.502	0.001	2.72	0.05	-16.88	0.19	0.369	0.001
	LiCl	5.5	0.05	2.86	0.05	15.08	0.14	0.434	0.001	2.64	0.05	-18.58	0.21	0.326	0.001
	MgCl2	8.11	0.07	4.93	0.07	17.66	0.15	0.32	0.001	3.19	0.06	-14.34	0.13	0.509	0.001
1L-1 nm	KCl	3.65	0.09	2.5	0.11	141.4	4.2	0.233	0.008	1.15	0.08	-225.64	8.59	0.067	0.004
	NaCl	2.8	0.09	1.73	0.09	113.2	4.4	0.201	0.007	1.07	0.08	-225.22	10.03	0.063	0.004
	LiCl	2.52	0.08	1.46	0.07	89.2	3.33	0.216	0.007	1.06	0.08	-176.15	8.91	0.079	0.004
	MgCl2	3.36	0.1	1.92	0.11	76.26	2.96	0.166	0.006	1.45	0.09	-200.83	7.48	0.095	0.005

Table 5.2: Simulated ion transport metrics. Current, average velocity and average concentration of ions inside various pores. The first column in a given section is the measured value, and the second column is the standard error, estimated by calculating the variation in a given output over the course of the simulation. We note that although average velocities for ions differ significantly, the values match expectation give bulk mobilities.

and Na^+, relative to that of K^+ after accounting for bulk mobility, are undiminished and the velocity of Mg^{2+} only marginally so; at first glance, it appears that the selectivity between cations (Fig. 5.5 e) derives from the number of charge carriers (ion concentration), which we find varies significantly (Table 5.2). The variation in the number of charge carriers is explained by the ability of each ion to enter the pore, which in turn is based on the ease with which it sheds its first and second hydration shells. This mechanism is the common explanation for various exotic effects in ion transport[14, 21, 43]. As we explain below, however, concentration inside the pore is not the ultimate cause of cation selectivity.

The probability density function (PDF) of ions inside 6L-1nm MoS_2 has three distinct regions, corresponding to three discrete ion hydration levels: ions in direct contact with the pore wall (region I), ions separated from the wall by a single water layer (region II) and ions separated from the wall by two water layers (region III) as shown in Fig. 5.5 g. The distance between peaks in the PDF and the location of the first water (O_w) layer correlates with the associated Mx^+-O_W coordination distance in the bulk (Fig. 5.6). As determined by the PDFs displayed in Fig. 5.5 g, only K^+ (and Na^+ but to a significantly reduced degree) occupies region I, corresponding to direct ion-wall contact. Na^+, Li^+ and K^+ all show significant density in region II, whereas Mg^{2+} is only able to occupy region III, corresponding to two

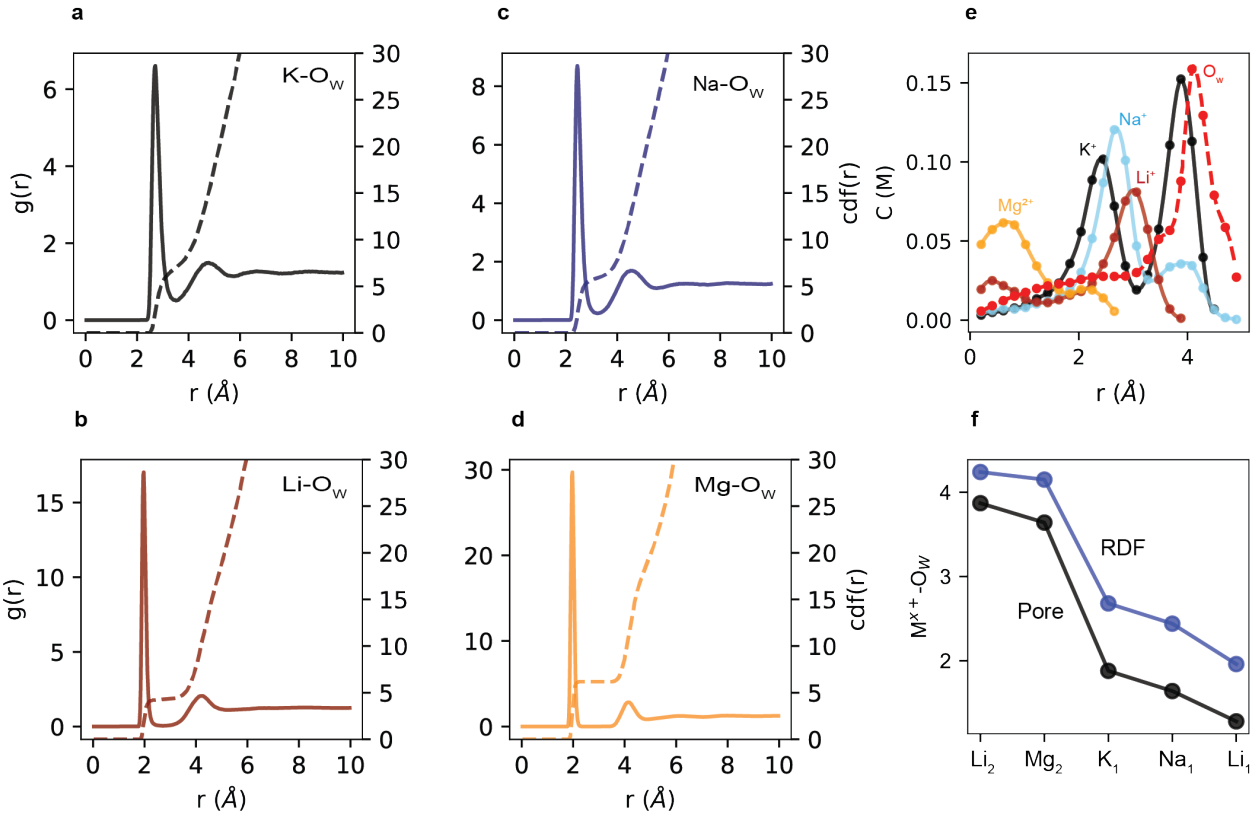

Figure 5.6: Ion solvation structures. M^{x+}- O_w radial distribution functions (RDFs) and cumulative distribution functions for all simulated cations (**a-d**). RDFs match existing literature, as do the coordination number in the 1st solvation shell for all cations[159, 160] **e**, Probability density functions, again normalized to K^+, for all cations as well as oxygen. **f**, Distance between the inner oxygen peak and the cation peak in e, compared to the corresponding peak in the RDF in **a-d**.

water layers between the ion and the pore wall. These results match expectations, given the relative hydration energies of the different cations[80]. The concentration of K^+ is higher because it occupies a larger fraction of the pore.

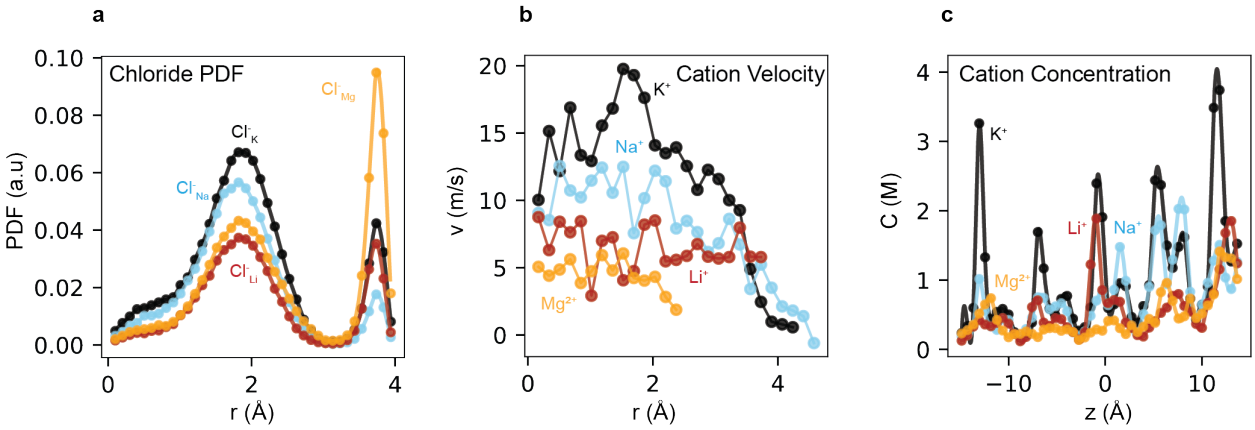

Figure 5.7: Simulated anion concentration and cation velocity data. **a**, Anion concentration profiles for all simulated salts. The preferred positions of chloride ions are independent of the cation, although the relative preference for each position varies. Velocity profiles for K^+, Na^+ and Mg^{2+} as a function of r and z for 6L-1nm MoS_2. **b**, Velocity profile for a 6L-1nm MoS_2 as a function of r for all ions simulated. These data are further analyzed in Fig 5.8, Cation concentration as a function of the z-coordinate in the pore. Ions prefer to occupy the Van der Waals gap between layers, leading to the oscillating pattern seen here.

The K^+ ions in direct contact with the pore wall do not, however, contribute significantly to the current, as they are trapped at the surface and their mobility approaches zero (Fig. 5.7 b). Instead, the vast majority of the current for all ions is from the second and third regions, where ions are separated from the pore wall by one to two layers of water (Fig. 5.5 h). Looking at these regions alone, we see that even though the monovalent ions have similar concentrations, the K^+ current outstrips that of Na^+ and especially Li^+. After normalizing by bulk mobility, the average velocity of monovalent cations goes as $K^+ > Na^+ > Li^+$ (Fig. 5.8) for this region. The observed selectivity between ions is not a function of the equilibrium concentration inside the pore, as was hypothesized previously, but is a dynamical process wherein the hydration energy of a given cation affects its mobility in the one- and two-layer of water region of the pore.

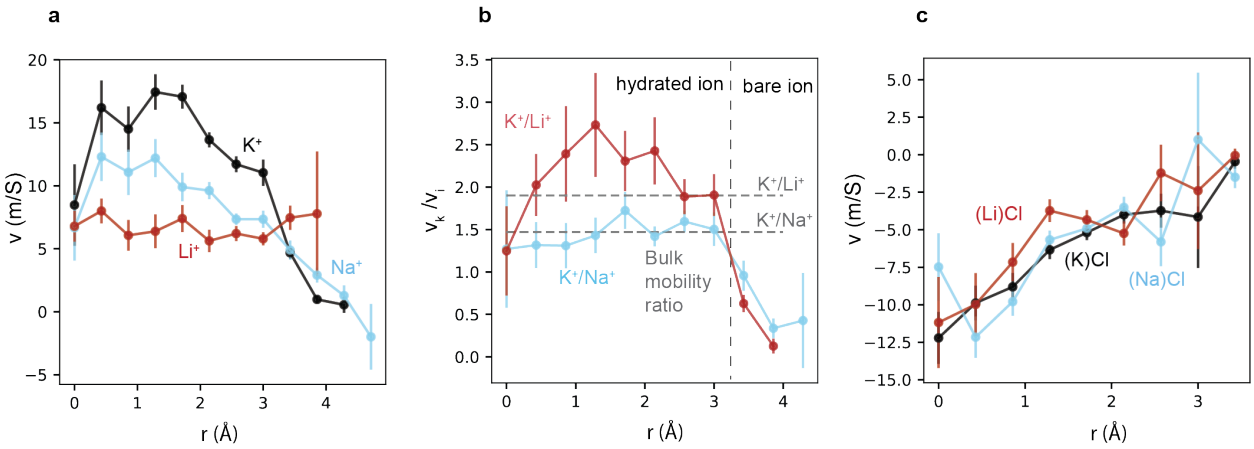

Figure 5.8: Radial velocity profiles for monovalent ions. **a**, Simulated velocity profiles for the monovalent ions K^+, Na^+, and Li^+. An obvious decay in velocity is observed for K^+ and Na^+ as the ions approach the wall. Li^+ remains hydrated (does not directly contact the wall) so the velocity does not decay at the pore edge. Because the distribution of K^+ ions is shifted towards the center of the pore relative to Na^+ (Fig. 5.5) their average speed is higher. **b**, Ratio of velocities (and the ratio of bulk mobilities) for the monovalent ions. Excluding ions at the pore edge, K^+ is significantly faster, even relative to its bulk value, than Li^+. **c**, Radial velocity profiles for chloride in the different monovalent salts. The velocity profile does not depend on cation identity, indicating that the concentration of anions is the sole determinant of total flux.

This dynamical effect is based on the relative ease with which a given cation exchanges its inner hydration shell and is impacted by the position the ion occupies inside the pore. We find that water molecules inside the 6L-1nm MoS_2 pore have a significantly reduced diffusion coefficient relative to that measured in the 6L-2nm MoS_2 or the bulk reservoir (Fig.5.5 i, Fig. 5.9). Water molecules, due to their interaction with the pore wall, are nearly trapped in place and are unable to travel with the transporting ion (Fig. 5.10). This has two effects: first, ions closer to the wall move more slowly. The selectivity between K^+ and Na^+ is a result of their relative preferred positions in the pore: K^+ is closer to the center, where the water moves more freely and enables the ion to move faster (Fig 5.5 i). Second, the sluggish water makes the rapid exchange of the inner hydration shell a larger component of ion mobility compared to the bulk case, where the inner hydration shell is partially carried along with the ion[80].

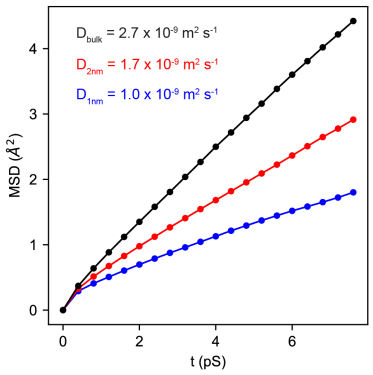

Figure 5.9: Calculation of water diffusion coefficients. Mean squared displacement of water molecules in the reservoirs of the simulation box (bulk) and in a 6L-2nm and 6L-1nm MoS_2. These data are calculated during a separate simulation run, in which no bias is applied across the simulation box and cations are added only to neutralize the MoS_2 surface charge. The bulk self-diffusion coefficient calculated from the MSD, which is in good agreement with the existing literature[161], is nearly three times as large for the bulk value compared to water confined to the 1 nm pore.

We calculate the energy penalty for the exchange of the inner hydration shell for each cation by performing a Boltzmann-inversion on the cation-oxygen radial distribution func-

tions; matching the drift velocity results, the order goes as K^+ $Na^+ < Li^+ < Mg^{2+}$ (Fig. 5.11). We conclude that inter-cation selectivity is determined by the preferred ion position and the rate of hydration shell exchange in the uniquely sluggish water inside the pore. This result highlights the role of the confining material, mediated through water friction, on ion transport. For example, we expect dramatically lower selectivity in hydrophobic nanochannels, such as carbon nanotubes[27], due to the reduced friction experienced by confined water.

We note that the transport dynamics of $MgCl_2$ are significantly different than the monovalent ions and underestimate the experimentally recorded selectivity. This is likely because our simulations are strictly classical and thus do not incorporate the effects of ion adsorption.

No cationic selectivity is observed for the monolayer film, in agreement with existing literature for sub-nm pores in monolayer MoS_2[157, 162]. Examining the velocity profiles of cations in the monolayer pore we find, after normalizing to their bulk values, little difference between ions. The thickness of the monolayer membrane (0.63 nm) is only slightly larger than the inner hydrated diameter of the cations, 0.4 – 0.54 nm, and smaller than the second hydration shell, 0.83 - 0.96 (Fig. 5.6). We infer that ions are partially hydrated by water molecules located outside the membrane, reducing the effect of confinement as shown in the snapshot image in Fig 5.5 b. We also note that two factors influence the total resistance felt by ionic species travelling through a single nanopore, the access resistance, R_{access} $\frac{1}{d}$, and the pore resistance, R_{pore} $\frac{4L}{\pi d^2}$, where L is the pore length and d the pore diameter57. For monolayer membranes with pore diameter $\sim$1 nm, the access resistance dominates, and any selectivity induced by the pore itself is reduced.

Now we turn to the role of the anion in the selectivity between different salts. As in our experiments, the transference number in our simulations with monolayer salts remains relatively constant (Fig. 5.12): the flux of K^+ is higher than that of Na^+ or Li^+, but so is the flux of $(K^+)Cl^-$ relative to $(Na^+)Cl^-$ and $(Li^+)Cl^-$ (Fig 5.5 f). For anions, this variation

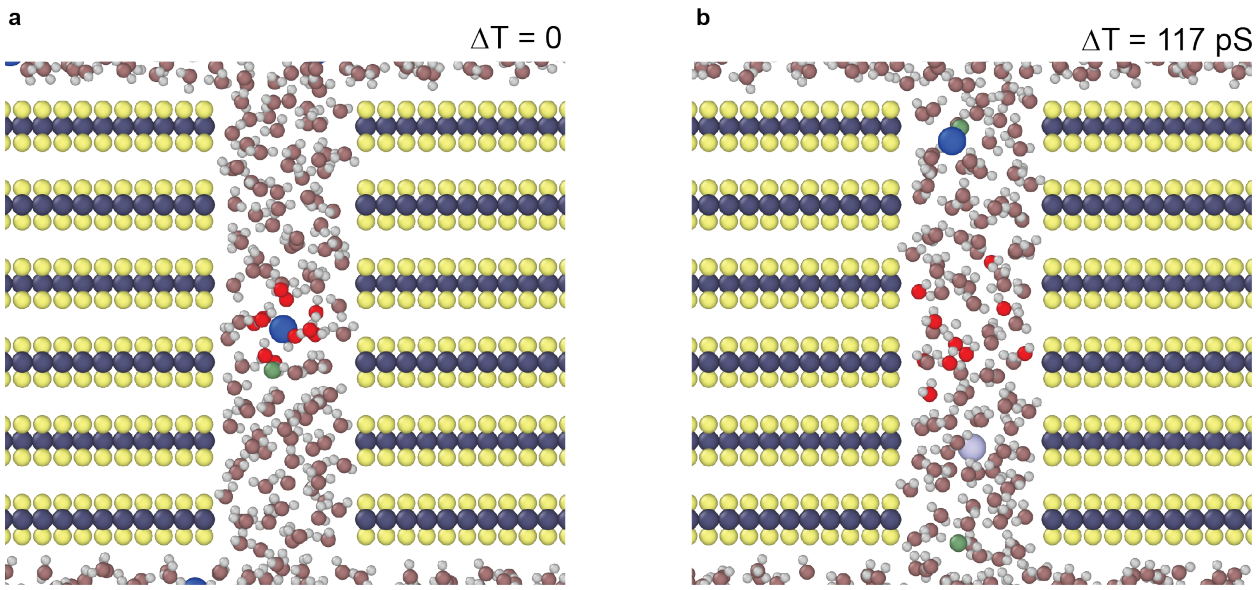

Figure 5.10: Snapshots showing water transport relative to ion motion. Molecular dynamics snapshots at two different times separated by 117 ps. In both snapshots, the same water molecules and K^+ ion are highlighted in bright red and blue, respectively (other K^+ ions are in pale blue). As the K^+ ion traverses the pore, it constantly exchanges its hydration shell, which remains mostly stuck in place.

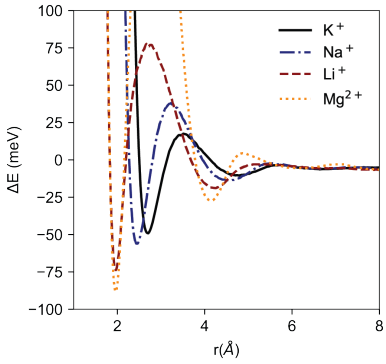

Figure 5.11: Radial energy profiles for M^{x+}-O_W interactions. These data are calculated via a Boltzmann-inversion of radial distribution functions (Fig. 5.6). Li^+ and Mg^{2+} show distinctly stronger interactions with the inner hydration shell, relative to K^+ especially, but also Na^+. Stronger interactions with the solvating water molecules lead to a reduced exchange rate and, therefore, slower migration.

is a function of both velocity and total concentration. There are more chloride anions in the center of the pore for K^+ and Na^+ compared to Li^+ or Mg^{2+}, and the total concentration varies significantly (Fig. 5.7). Although the anion velocity profiles are identical for each salt, the concentration distributions vary. The velocity of ions increases near the pore center, leading to higher average mobilities for $(K^+)Cl^-$ and $(Na^+)Cl^-$ (Fig. 5.8).

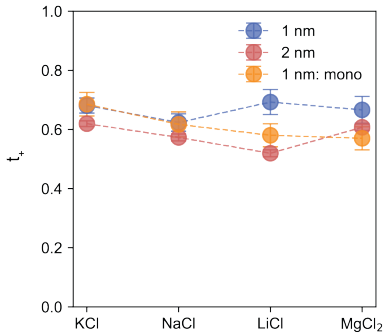

Figure 5.12: Simulated transference numbers. Transference number for various salts, calculated using the values in Table 5.2

The variation in concentration can be understood by observing that the 1 nm pore induces a high degree of ion-ion interactions between cation and anion. Two oppositely charged ions are strongly coupled when their internuclear distance d_{ij} is less than the Bjerrum length $l_B = \frac{e^2}{4\pi\epsilon_0\epsilon_r k_B T}$ 0.7 nm[163]. For 6L-1nm MoS_2, independent of the salt, chloride ions are paired with an adjacent cation for nearly half the total time it takes to permeate through the pore. Ion-ion interactions are effectively non-existent for 1L-1nm and are reduced in the 6L-2nm MoS_2 (Fig. 5.13). We conclude that, for long and narrow ($<$ 2 nm) negatively charged pores, a high degree of ion coupling takes place. This coupling results in a higher concentration of anions (near the center of the pore) due to the strong electrostatic attraction between cation and anion. Finally, we note that a marginal degree of selectivity between divalent and monovalent salts exists in 1 nm pores in multilayer membranes with sufficient surface charge, even if only electrostatic effects (Section 5.4) are considered. No selectivity between monovalent ions can exist in this simplified system, however.

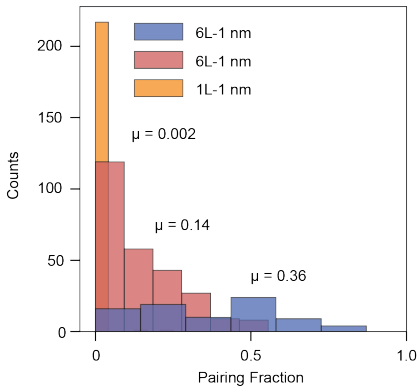

Figure 5.13: Ion pairing in nanopores. The number of cations that are paired ($d<l_B$) with an anion for a given fraction of the duration it takes for the cation to pass through the pore. Mean pairing fraction is given, showing that the ions are effectively non-interacting in the monolayer but are strongly coupled in the six-layer film.

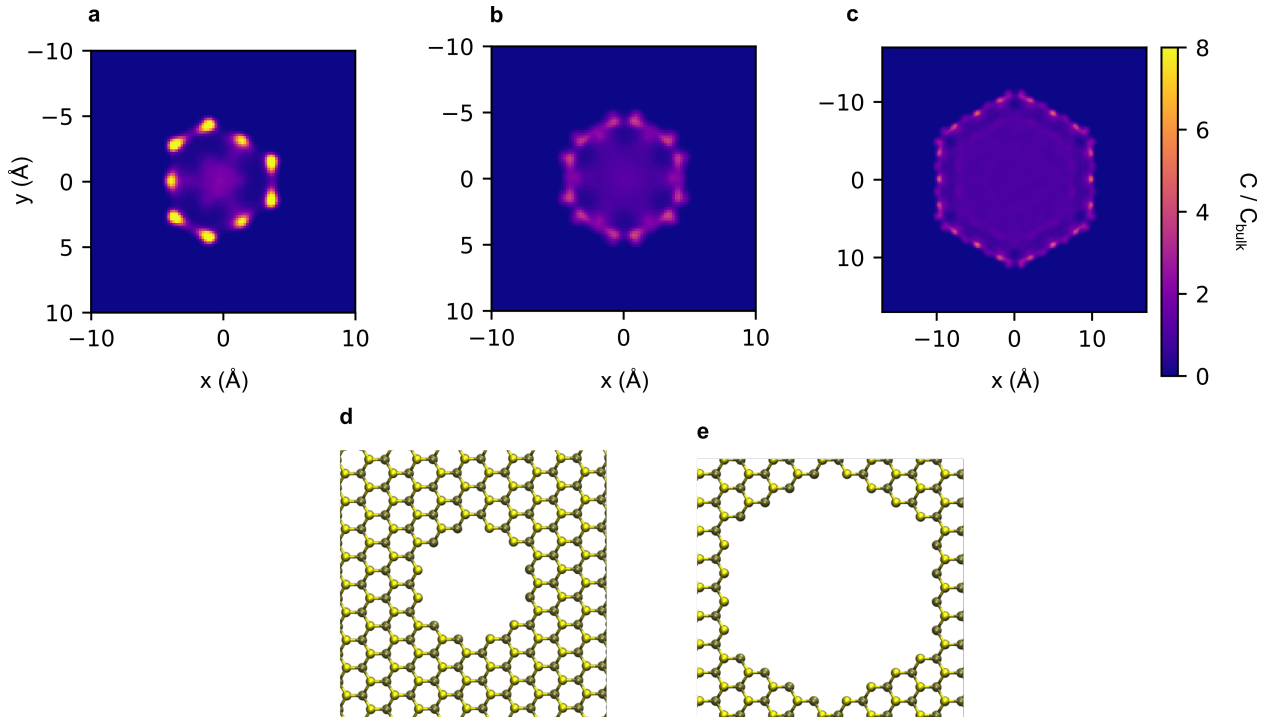

Figure 5.14: Oxygen (water) density profiles. Data shown for a (**a**) 1 nm diameter pore in monolayer, a (**b**) six-layer MoS_2 film and a (**c**) 2 nm diameter pore in a six-layer MoS_2 film. **d-e**, Crystal structure of a 1 nm and 2 nm diameter pore in a MoS_2 film, oriented to match the water density profiles in **a-c**.

Element	ϵ (kcal mol^{-1})	σ (Å)	Partial charge (e)
H	0	0	0.3
O	0.155	3.16	-0.6
K	0.583	2.69	1
Na	0.1	2.58	1
Li	0.167	2.95	1
Mg	0.14	1.63	2
Cl	0.1	4.4	-1
Mo	0.13	2.55	-0.76
S	0.25	3.5	0.38

Table 5.3: Lennard-Jones parameters and partial charges used for MD simulations.

5.4 Finite element simulations

Finite element (FE) simulations based on the standard Poisson-Nernst-Planck (PNP) model ignore both ion correlations and finite-size effects[39]. For salts with similar bulk conductivities, such as for $MgCl_2$ and KCl, FE simulations effectively isolate the electrostatic interactions between the ions and the channel wall. We focus on this pair because the effect of ion valence dominates in the absence of size effects. Due to the relatively small computational complexity of FE simulations, we are able to simulate a large fraction of the parameter space, varying both surface charge and pore diameter.

The Poisson-Nernst-Planck equations, detailed in Section 5.4.1, are solved in COMSOL Multiphysics with the Transport of Diluted Species and Electrostatics modules. We assume the pore is cylindrical and thereby enforce an axisymmetric symmetry and solve the PNP equations in two-dimensional (r, z) space. We use an adaptive triangular mesh. The geometry is schematized in Fig. 5.15. We parameterize the model with the surface charge and pore diameter, allowing the former to vary from 0-0.075 C m^{-}2 and the latter to vary from 0.5-5 nm. The concentration of cations is set at 1 M, and a 1 V bias is applied across the pore. Even in 1 M electrolytes, where the Debye length is 0.3 nm, significant deviations from bulk behavior are observed for moderate to high surface charge densities. First, we measure the KCl/$MgCl_2$ selectivity for pores with a diameter of 0.5 to 5 nm (5.15 b). The largest

pores fail to discern KCl and $MgCl_2$. KCl has a significantly higher conductance than $MgCl_2$ through pores < 2 nm with a surface charge $> .025$ C m$^-$2. As the chloride contribution is a small fraction of the total current for these pores (5.15 c), we attribute this difference to the cation alone. For a small enough pore with a large enough surface charge, the number of charge carriers will be increase to neutralize the pore. Mg^{2+} is divalent, so fewer ions are required to neutralize the pore, concentration in, and therefore the current through, the pore. We note that the selectivity measured via FE simulations is smaller than that measured in MD simulations under similar conditions, as the FE simulations only account for electrostatic effects.

5.4.1 PNP model of ion transport

To derive the PNP model [39], we start by writing down a mass-balance equation for the transport of a given ionic species i:

$$\frac{\partial c_i}{\partial t} = -\nabla \cdot F_i, \tag{5.5}$$

where c_i is the ion concentration and F_i is the ionic flux. F_i can be related back to concentration (and electrostatic potential) *via* Fick's law:

$$F_i = c_i u - \frac{D_i k_B T}{c_i} \nabla \mu_i, \tag{5.6}$$

where u is the bulk fluid velocity, μ_i is the chemical potential for a given ionic species, k_B is Boltzmann's constant, and T is the temperature. The first time in this expression denotes convection, the second diffusion. To solve for u in the convection term, we couple the PNP equations to the Navier-Stokes equations for fluid flow and assume incompressibility. In this thesis, we find that convection has a negligible effect on ion transport.

For the diffusion term, we write the chemical potential in terms of concentration and

electrostatic potential *via* a form of the Nernst equation:

$$\mu_i = -k_B T \ln(c_i) + ze\phi, \tag{5.7}$$

where z is the ion valence, e is the electron charge and ϕ the electrostatic potential. Finally, we relate the electrostatic potential to the charge density *via* the Poisson-equation:

$$-\nabla \cdot \epsilon \nabla \phi = \rho = \sum_i z_i e c_i \tag{5.8}$$

Ignoring convection, and adopting the boundary conditions relevant for a specific geometry, Eqs. 5.5–5.8 are a complete set of differential equations that can be used to solve for ion transport in a diverse set of scenarios. Standard boundary conditions are enforcing a constant potential ϕ and impermeable (no-flux) walls, or fixing the concentration c_i to a set value.

5.4.2 Finite element simulation results

By tuning the pore size and pore surface charge over the range of possible values (d = 0.5-2 nm, σ = 0-70 mC m^{-2}, we assess the effect of electrostatic interactions on both cation/anion and monovalent/divalent cationic selectivity. We find that only at the smallest pore diameters (<0.5 nm) at high surface charge (> 50 mC m^{-2} does the selectivity approach that derived in our molecular dynamics simulations, indicating that size and solvation is the dominating force driving selectivity in MoS_2 nanopores.

5.5 Conclusion

In summary, we present a novel in situ electrochemical method for the fabrication of nanoporous membranes using polycrystalline MoS_2. These membranes exhibit remarkable selectivity for small monovalent and divalent cations, showcasing their potential for ion separation applica-

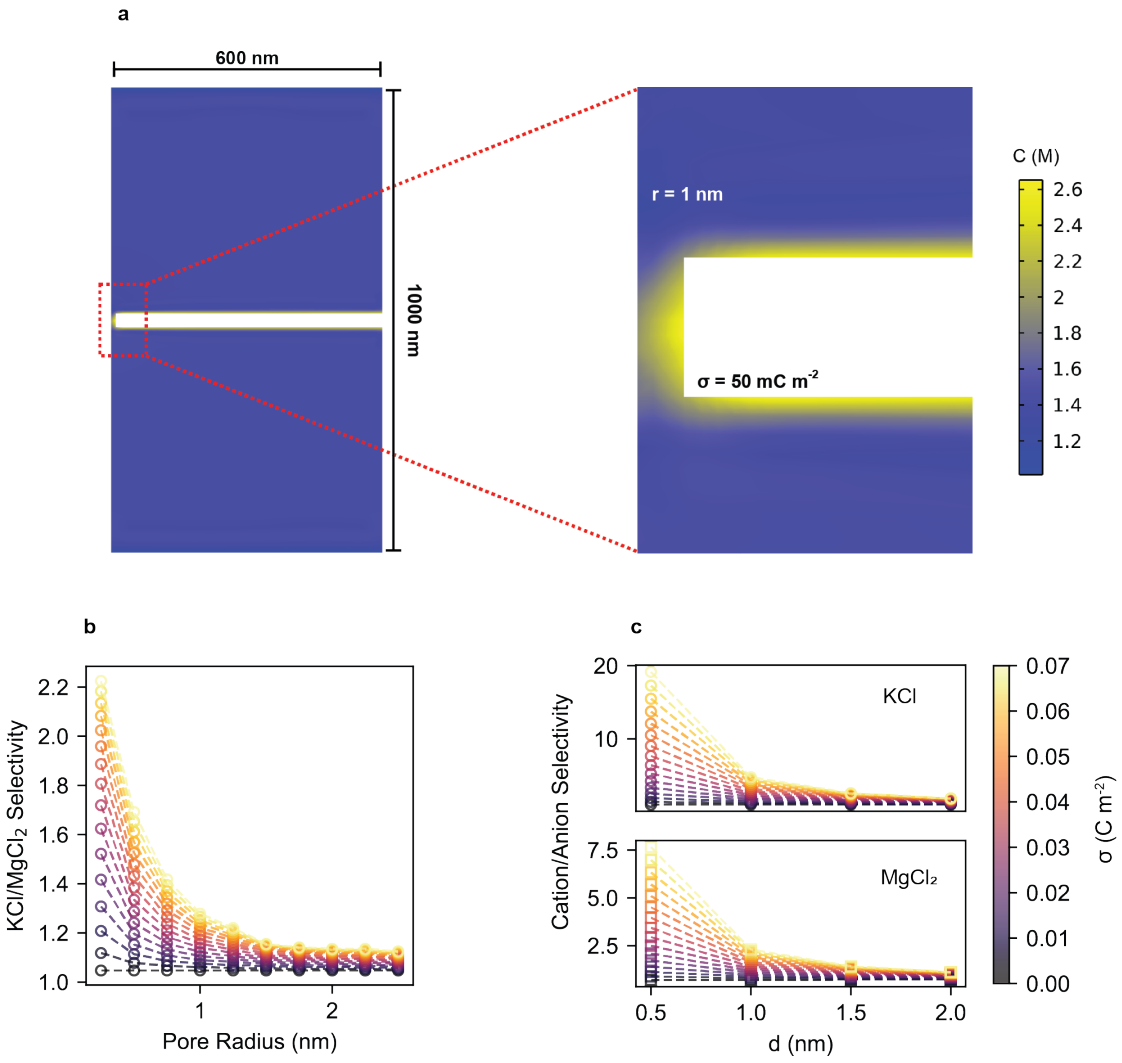

Figure 5.15: Finite element simulations results. Geometry of finite element simulations, with the steady-state concentration of K^+. The pore size and surface charge is tuned across a range of values; here, r = 1 nm and $\sigma = 50$ mC m^{-2}

tions. As a result of the dense array of nanopores in the MoS_2 membranes, the absolute flux outstrips existing devices that display similar levels of selectivity. This feature makes these membranes a more practical device for ion separations. MD simulations provide insights into the underlying mechanisms responsible for the observed selectivity, emphasizing the role of the sluggish water confined to the pore and ion-ion interactions.

5.6 Methods

5.6.1 MD simulations

We build 2H-phase MoS_2 slabs with one or six layers that separate two 1M electrolyte reservoirs. Mo and S atoms are deleted within a given radius in the center of the slab to create a pore. Each reservoir is 7.5 nm in height, and 3 nm in width and depth. The simulation is periodic in all three dimensions. Lennard Jones (LJ) parameters are tabulated in Table 5.3 and cross-terms are calculated using the Lorentz-Berthelot mixing rules. The mixing rule for $MgCl_2$ is modified to increase the interaction strength between Mg and Cl, as determined by Mamatkulov *et al.*[164] To retain consistency between ions, we use parameters that are optimized with the same set of simulation conditions (the same parameters for both anion and water). Water is modelled explicitly using the SPC/E model, and the bonds are held rigid using the SHAKE algorithm[96]. The atoms in the MoS_2 sheet are fixed. Likely due to hydroxyl adsorption, wetted pores in MoS_2 are negatively charged[16]. We model this effect by adding an additional charge to all Mo and S atoms exposed to the electrolyte, such that the total surface charge density is 50 mC m^{-2}. To obtain an accurate picture of water dynamics inside the pore, we perform an additional set of simulations with the same parameters, excluding both an applied electric field and the salt. Additional cations are, however, added to compensate for the negative surface charge of the MoS_2 film.

Molecular dynamic simulations were performed using the LAAMPS package[106]. The

initial configuration is calculated using Packmol[165] and the water bonds set by TopoTools in Visual Molecular Dynamics[166]. First, we run an NPT ensemble for 0.5 ns, at which time the pore is entirely filled with water molecules and all thermodynamic variables have stabilized. Then we carry out a production run with an NVT ensemble for 8-20 ns. The pure-water simulations are run for 0.5 ns. Analysis is carried out using MDAnalysis[167] software in Python. Ionic current is calculated by extracting average drift velocity of ions (motion parallel to the electric field), v_z and number density n through $J = qnv_z$, where q is the ion charge and J the current. Average velocity is calculated by averaging the gradient of position in the z direction over all ions in the pore through the course of the simulation. All code and simulation scripts are available on request.

REFERENCES

[1] D. S. Sholl and R. P. Lively, "Seven chemical separations to change the world," *Nature*, vol. 532, pp. 435–437, Apr. 2016.

[2] D. A. Doyle, J. M. Cabral, R. A. Pfuetzner, A. Kuo, J. M. Gulbis, S. L. Cohen, B. T. Chait, and R. MacKinnon, "The structure of the potassium channel: molecular basis of K+ conduction and selectivity," *Science*, vol. 280, pp. 69–77, Apr. 1998. Publisher: American Association for the Advancement of Science.

[3] L. Wang, J. He, M. Heiranian, H. Fan, L. Song, Y. Li, and M. Elimelech, "Water transport in reverse osmosis membranes is governed by pore flow, not a solution-diffusion mechanism," *Science Advances*, vol. 9, no. 15, p. eadf8488, 2023. Publisher: American Association for the Advancement of Science.

[4] K. Schmidt-Rohr and Q. Chen, "Parallel cylindrical water nanochannels in Nafion fuel-cell membranes," *Nature Materials*, vol. 7, pp. 75–83, Jan. 2008.

[5] N. R. Aluru, F. Aydin, M. Z. Bazant, D. Blankschtein, A. H. Brozena, J. P. de Souza, M. Elimelech, S. Faucher, J. T. Fourkas, V. B. Koman, M. Kuehne, H. J. Kulik, H.-K. Li, Y. Li, Z. Li, A. Majumdar, J. Martis, R. P. Misra, A. Noy, T. A. Pham, H. Qu, A. Rayabharam, M. A. Reed, C. L. Ritt, E. Schwegler, Z. Siwy, M. S. Strano, Y. Wang, Y.-C. Yao, C. Zhan, and Z. Zhang, "Fluids and electrolytes under confinement in single-digit nanopores," *Chemical Reviews*, vol. 123, pp. 2737–2831, Mar. 2023. Publisher: American Chemical Society.

[6] A. H. Castro Neto, F. Guinea, N. M. R. Peres, K. S. Novoselov, and A. K. Geim, "The electronic properties of graphene," *Rev. Mod. Phys.*, vol. 81, pp. 109–162, Jan. 2009. Publisher: American Physical Society.

[7] A. Splendiani, L. Sun, Y. Zhang, T. Li, J. Kim, C.-Y. Chim, G. Galli, and F. Wang, "Emerging photoluminescence in monolayer MoS_2," *Nano Letters*, vol. 10, pp. 1271–1275, Apr. 2010. Publisher: American Chemical Society.

[8] Y. Shin, M. Lozada-Hidalgo, J. L. Sambricio, I. V. Grigorieva, A. K. Geim, and C. Casiraghi, "Raman spectroscopy of highly pressurized graphene membranes," *Applied Physics Letters*, vol. 108, p. 221907, May 2016. Publisher: American Institute of Physics.

[9] P. Z. Sun, Q. Yang, W. J. Kuang, Y. V. Stebunov, W. Q. Xiong, J. Yu, R. R. Nair, M. I. Katsnelson, S. J. Yuan, I. V. Grigorieva, M. Lozada-Hidalgo, F. C. Wang, and A. K. Geim, "Limits on gas impermeability of graphene," *Nature*, vol. 579, pp. 229–232, Mar. 2020.

[10] J. C. Meyer, A. K. Geim, M. I. Katsnelson, K. S. Novoselov, T. J. Booth, and S. Roth, "The structure of suspended graphene sheets," *Nature*, vol. 446, pp. 60–63, Mar. 2007.

[11] F. Liu, W. Wu, Y. Bai, S. H. Chae, Q. Li, J. Wang, J. Hone, and X.-Y. Zhu, "Disassembling 2D van der Waals crystals into macroscopic monolayers and reassembling into artificial lattices," *Science*, vol. 367, pp. 903–906, Feb. 2020. Publisher: American Association for the Advancement of Science.

[12] Y. Liu, H. Nan, X. Wu, W. Pan, W. Wang, J. Bai, W. Zhao, L. Sun, X. Wang, and Z. Ni, "Layer-by-layer thinning of MoS_2 by plasma," *ACS Nano*, vol. 7, pp. 4202–4209, May 2013. Publisher: American Chemical Society.

[13] A. Esfandiar, B. Radha, F. C. Wang, Q. Yang, S. Hu, S. Garaj, R. R. Nair, A. K. Geim, and K. Gopinadhan, "Size effect in ion transport through angstrom-scale slits," *Science*, vol. 358, pp. 511–513, Oct. 2017. Publisher: American Association for the Advancement of Science.

[14] T. Jain, B. C. Rasera, R. J. S. Guerrero, M. S. H. Boutilier, S. C. O'Hern, J.-C. Idrobo, and R. Karnik, "Heterogeneous sub-continuum ionic transport in statistically isolated graphene nanopores," *Nature Nanotechnology*, vol. 10, pp. 1053–1057, Dec. 2015.

[15] A. K. Geim and I. V. Grigorieva, "Van der Waals heterostructures," *Nature*, vol. 499, pp. 419–425, July 2013.

[16] J. Feng, M. Graf, K. Liu, D. Ovchinnikov, D. Dumcenco, M. Heiranian, V. Nandigana, N. R. Aluru, A. Kis, and A. Radenovic, "Single-layer MoS_2 nanopores as nanopower generators," *Nature*, vol. 536, pp. 197–200, Aug. 2016.

[17] J. K. Holt, H. G. Park, Y. Wang, M. Stadermann, A. B. Artyukhin, C. P. Grigoropoulos, A. Noy, and O. Bakajin, "Fast Mass Transport Through Sub-2-Nanometer Carbon Nanotubes," *Science*, vol. 312, pp. 1034–1037, May 2006. Publisher: American Association for the Advancement of Science.

[18] Z. Wang, Q. Tu, S. Zheng, J. J. Urban, S. Li, and B. Mi, "Understanding the aqueous stability and filtration capability of MoS2 membranes," *Nano letters*, vol. 17, no. 12, pp. 7289–7298, 2017. Publisher: ACS Publications.

[19] V. Kapil, C. Schran, A. Zen, J. Chen, C. J. Pickard, and A. Michaelides, "The first-principles phase diagram of monolayer nanoconfined water," *Nature*, vol. 609, pp. 512–516, Sept. 2022.

[20] G. Algara-Siller, O. Lehtinen, F. Wang, R. R. Nair, U. Kaiser, H. Wu, A. K. Geim, and I. V. Grigorieva, "Square ice in graphene nanocapillaries," *Nature*, vol. 519, no. 7544, pp. 443–445, 2015. Publisher: Nature Publishing Group UK London.

[21] Y. Fu, S. Su, N. Zhang, Y. Wang, X. Guo, and J. Xue, "Dehydration-determined ion selectivity of graphene subnanopores," *ACS Applied Materials & Interfaces*, vol. 12, pp. 24281–24288, May 2020. Publisher: American Chemical Society.

[22] S. Goutham, A. Keerthi, A. Ismail, A. Bhardwaj, H. Jalali, Y. You, Y. Li, N. Hassani, H. Peng, M. V. S. Martins, F. Wang, M. Neek-Amal, and B. Radha, "Beyond steric selectivity of ions using ångström-scale capillaries," *Nature Nanotechnology*, Mar. 2023.

[23] P. Robin, N. Kavokine, and L. Bocquet, "Modeling of emergent memory and voltage spiking in ionic transport through angstrom-scale slits," *Science*, vol. 373, pp. 687–691, Aug. 2021. Publisher: American Association for the Advancement of Science.

[24] G. Hummer, J. C. Rasaiah, and J. P. Noworyta, "Water conduction through the hydrophobic channel of a carbon nanotube," *nature*, vol. 414, no. 6860, pp. 188–190, 2001. Publisher: Nature Publishing Group UK London.

[25] R. Tunuguntla, F. Allen, K. Kim, A. Belliveau, and A. Noy, "Ultra-Fast Proton Transport in Sub-1-nm Diameter Carbon Nanotube Porins," *Biophysical Journal*, vol. 110, no. 3, p. 338a, 2016. Publisher: Elsevier.

[26] K. V. Agrawal, S. Shimizu, L. W. Drahushuk, D. Kilcoyne, and M. S. Strano, "Observation of extreme phase transition temperatures of water confined inside isolated carbon nanotubes," *Nature nanotechnology*, vol. 12, no. 3, pp. 267–273, 2017. Publisher: Nature Publishing Group UK London.

[27] Z. Li, R. P. Misra, Y. Li, Y.-C. Yao, S. Zhao, Y. Zhang, Y. Chen, D. Blankschtein, and A. Noy, "Breakdown of the Nernst–Einstein relation in carbon nanotube porins," *Nature Nanotechnology*, vol. 18, pp. 177–183, Feb. 2023.

[28] R. H. Tunuguntla, R. Y. Henley, Y.-C. Yao, T. A. Pham, M. Wanunu, and A. Noy, "Enhanced water permeability and tunable ion selectivity in subnanometer carbon nanotube porins," *Science*, vol. 357, no. 6353, pp. 792–796, 2017. Publisher: American Association for the Advancement of Science.

[29] E. Hoenig, Y. Han, M. Wang, and C. Liu, "In Situ Generation of (Sub)Nanopores in MoS_2 Membranes for Ion Selective Transport," *Submitted*, 2023.

[30] Y. You, A. Ismail, G.-H. Nam, S. Goutham, A. Keerthi, and B. Radha, "Angstrofluidics: Walking to the limit," *Annual Review of Materials Research*, vol. 52, pp. 189–218, 2022. Publisher: Annual Reviews.

[31] N. Kavokine, M.-L. Bocquet, and L. Bocquet, "Fluctuation-induced quantum friction in nanoscale water flows," *Nature*, vol. 602, pp. 84–90, Feb. 2022.

[32] D. J. Bonthuis, K. F. Rinne, K. Falk, C. N. Kaplan, D. Horinek, A. N. Berker, L. Bocquet, and R. R. Netz, "Theory and simulations of water flow through carbon nanotubes: prospects and pitfalls," *Journal of Physics: Condensed Matter*, vol. 23, no. 18, p. 184110, 2011. Publisher: IOP Publishing.

[33] H. Y. Yang, Z. J. Han, S. F. Yu, K. L. Pey, K. Ostrikov, and R. Karnik, "Carbon nanotube membranes with ultrahigh specific adsorption capacity for water desalination

and purification," *Nature communications*, vol. 4, no. 1, p. 2220, 2013. Publisher: Nature Publishing Group UK London.

[34] R. Joshi, P. Carbone, F.-C. Wang, V. G. Kravets, Y. Su, I. V. Grigorieva, H. Wu, A. K. Geim, and R. R. Nair, "Precise and ultrafast molecular sieving through graphene oxide membranes," *science*, vol. 343, no. 6172, pp. 752–754, 2014. Publisher: American Association for the Advancement of Science.

[35] E. Hoenig, S. E. Strong, M. Wang, J. M. Radhakrishnan, N. J. Zaluzec, J. Skinner, and C. Liu, "Controlling the structure of MoS_2 membranes via covalent functionalization with molecular spacers," *Nano Letters*, vol. 20, no. 11, pp. 7844–7851, 2020. Publisher: ACS Publications.

[36] L. Ries, E. Petit, T. Michel, C. C. Diogo, C. Gervais, C. Salameh, M. Bechelany, S. Balme, P. Miele, N. Onofrio, and others, "Enhanced sieving from exfoliated MoS_2 membranes via covalent functionalization," *Nature materials*, vol. 18, no. 10, pp. 1112–1117, 2019. Publisher: Nature Publishing Group UK London.

[37] S. Faucher, N. Aluru, M. Z. Bazant, D. Blankschtein, A. H. Brozena, J. Cumings, J. Pedro de Souza, M. Elimelech, R. Epsztein, J. T. Fourkas, A. G. Rajan, H. J. Kulik, A. Levy, A. Majumdar, C. Martin, M. McEldrew, R. P. Misra, A. Noy, T. A. Pham, M. Reed, E. Schwegler, Z. Siwy, Y. Wang, and M. Strano, "Critical knowledge gaps in mass transport through single-digit nanopores: a review and perspective," *The Journal of Physical Chemistry C*, vol. 123, pp. 21309–21326, Sept. 2019. Publisher: American Chemical Society.

[38] S. Kumar and B. Bagchi, "Correlation lengths in nanoconfined water and transport properties," *The Journal of Chemical Physics*, vol. 156, p. 224501, June 2022.

[39] B. D. Storey and M. Z. Bazant, "Effects of electrostatic correlations on electrokinetic phenomena," *Physical Review E*, vol. 86, p. 056303, Nov. 2012. Publisher: American Physical Society.

[40] M. S. Kilic, M. Z. Bazant, and A. Ajdari, "Steric effects in the dynamics of electrolytes at large applied voltages. II. Modified Poisson-Nernst-Planck equations," *Physical review E*, vol. 75, no. 2, p. 021503, 2007. Publisher: APS.

[41] C. Cheng, G. Jiang, G. P. Simon, J. Z. Liu, and D. Li, "Low-voltage electrostatic modulation of ion diffusion through layered graphene-based nanoporous membranes," *Nature nanotechnology*, vol. 13, no. 8, pp. 685–690, 2018. Publisher: Nature Publishing Group UK London.

[42] M. Heiranian, A. B. Farimani, and N. R. Aluru, "Water desalination with a single-layer MoS2 nanopore," *Nature communications*, vol. 6, no. 1, p. 8616, 2015. Publisher: Nature Publishing Group UK London.

[43] S. Sahu, M. Di Ventra, and M. Zwolak, "Dehydration as a universal mechanism for ion selectivity in graphene and other atomically thin pores," *Nano Letters*, vol. 17, pp. 4719–4724, Aug. 2017. Publisher: American Chemical Society.

[44] M. Wang, T. Sadhukhan, N. H. Lewis, O.-S. Lee, W. Maoyu, X. He, Y. Gangbin, E. Hoenig, Y. Han, S. Fengyuan, D. Tiede, H. Zhou, A. Tokmakoff, G. Schatz, and C. Liu, "Anomalously Enhanced Ion Transport and Uptake in Functionalized Angstrom-Scale Two-dimensional Channels," *Submitted*, 2023.

[45] S. Hu, K. Gopinadhan, A. Rakowski, M. Neek-Amal, T. Heine, I. Grigorieva, S. Haigh, F. Peeters, A. Geim, and M. Lozada-Hidalgo, "Transport of hydrogen isotopes through interlayer spacing in van der Waals crystals," *Nature nanotechnology*, vol. 13, no. 6, pp. 468–472, 2018. Publisher: Nature Publishing Group UK London.

[46] D. Saha and P. Kruse, "Editors' choice—review—conductive forms of MoS2 and their applications in energy storage and conversion," *Journal of The Electrochemical Society*, vol. 167, no. 12, p. 126517, 2020. Publisher: IOP Publishing.

[47] J. Strachan, A. F. Masters, and T. Maschmeyer, "3R-MoS2 in review: history, status, and outlook," *ACS Applied Energy Materials*, vol. 4, no. 8, pp. 7405–7418, 2021. Publisher: ACS Publications.

[48] C. Hu, A. Achari, P. Rowe, H. Xiao, S. Suran, Z. Li, K. Huang, C. Chi, C. Cherian, V. Sreepal, and others, "pH-dependent water permeability switching and its memory in MoS2 membranes," *Nature*, pp. 1–5, 2023. Publisher: Nature Publishing Group UK London.

[49] Y. An, A. Kuc, P. Petkov, M. Lozada-Hidalgo, and T. Heine, "On the chemistry and diffusion of hydrogen in the interstitial space of layered crystals h-BN, MoS_2, and graphite," *Small*, vol. 15, no. 43, p. 1901722, 2019. Publisher: Wiley Online Library.

[50] L. Chen, G. Shi, J. Shen, B. Peng, B. Zhang, Y. Wang, F. Bian, J. Wang, D. Li, Z. Qian, and others, "Ion sieving in graphene oxide membranes via cationic control of interlayer spacing," *Nature*, vol. 550, no. 7676, pp. 380–383, 2017. Publisher: Nature Publishing Group UK London.

[51] M. Hu and B. Mi, "Enabling graphene oxide nanosheets as water separation membranes," *Environmental science & technology*, vol. 47, no. 8, pp. 3715–3723, 2013. Publisher: ACS Publications.

[52] T. Liu, L. Tian, N. Graham, B. Yang, W. Yu, and K. Sun, "Regulating the interlayer spacing of graphene oxide membranes and enhancing their stability by use of PACl," *Environmental science & technology*, vol. 53, no. 20, pp. 11949–11959, 2019. Publisher: ACS Publications.

[53] A. Morelos-Gomez, R. Cruz-Silva, H. Muramatsu, J. Ortiz-Medina, T. Araki, T. Fukuyo, S. Tejima, K. Takeuchi, T. Hayashi, M. Terrones, and others, "Effective

NaCl and dye rejection of hybrid graphene oxide/graphene layered membranes," *Nature nanotechnology*, vol. 12, no. 11, pp. 1083–1088, 2017. Publisher: Nature Publishing Group UK London.

[54] R. Nair, H. Wu, P. N. Jayaram, I. V. Grigorieva, and A. Geim, "Unimpeded permeation of water through helium-leak–tight graphene-based membranes," *Science*, vol. 335, no. 6067, pp. 442–444, 2012. Publisher: American Association for the Advancement of Science.

[55] S. Sahu and M. Zwolak, "Ionic selectivity and filtration from fragmented dehydration in multilayer graphene nanopores," *Nanoscale*, vol. 9, no. 32, pp. 11424–11428, 2017. Publisher: Royal Society of Chemistry.

[56] S. P. Surwade, S. N. Smirnov, I. V. Vlassiouk, R. R. Unocic, G. M. Veith, S. Dai, and S. M. Mahurin, "Water desalination using nanoporous single-layer graphene," *Nature Nanotechnology*, vol. 10, pp. 459–464, May 2015.

[57] K. Raidongia and J. Huang, "Nanofluidic ion transport through reconstructed layered materials," *Journal of the American Chemical Society*, vol. 134, no. 40, pp. 16528–16531, 2012. Publisher: ACS Publications.

[58] C. Chen, J. Wang, D. Liu, C. Yang, Y. Liu, R. S. Ruoff, and W. Lei, "Functionalized boron nitride membranes with ultrafast solvent transport performance for molecular separation," *Nature communications*, vol. 9, no. 1, p. 1902, 2018. Publisher: Nature Publishing Group UK London.

[59] C. E. Ren, K. B. Hatzell, M. Alhabeb, Z. Ling, K. A. Mahmoud, and Y. Gogotsi, "Charge-and size-selective ion sieving through Ti3C2T x MXene membranes," *The journal of physical chemistry letters*, vol. 6, no. 20, pp. 4026–4031, 2015. Publisher: ACS Publications.

[60] L. Ding, Y. Wei, L. Li, T. Zhang, H. Wang, J. Xue, L.-X. Ding, S. Wang, J. Caro, and Y. Gogotsi, "MXene molecular sieving membranes for highly efficient gas separation," *Nature communications*, vol. 9, no. 1, p. 155, 2018. Publisher: Nature Publishing Group UK London.

[61] L. Sun, Y. Ying, H. Huang, Z. Song, Y. Mao, Z. Xu, and X. Peng, "Ultrafast molecule separation through layered WS2 nanosheet membranes," *ACS nano*, vol. 8, no. 6, pp. 6304–6311, 2014. Publisher: ACS Publications.

[62] G. Liu, W. Jin, and N. Xu, "Two-dimensional-material membranes: a new family of high-performance separation membranes," *Angewandte Chemie International Edition*, vol. 55, no. 43, pp. 13384–13397, 2016. Publisher: Wiley Online Library.

[63] L. Sun, H. Huang, and X. Peng, "Laminar MoS 2 membranes for molecule separation," *Chemical communications*, vol. 49, no. 91, pp. 10718–10720, 2013. Publisher: Royal Society of Chemistry.

[64] W. Hirunpinyopas, E. Prestat, S. D. Worrall, S. J. Haigh, R. A. Dryfe, and M. A. Bissett, "Desalination and nanofiltration through functionalized laminar MoS_2 membranes," *ACS nano*, vol. 11, no. 11, pp. 11082–11090, 2017. Publisher: ACS Publications.

[65] S. Zheng, Q. Tu, J. J. Urban, S. Li, and B. Mi, "Swelling of graphene oxide membranes in aqueous solution: characterization of interlayer spacing and insight into water transport mechanisms," *ACS nano*, vol. 11, no. 6, pp. 6440–6450, 2017. Publisher: ACS Publications.

[66] M. Deng, K. Kwac, M. Li, Y. Jung, and H. G. Park, "Stability, molecular sieving, and ion diffusion selectivity of a lamellar membrane from two-dimensional molybdenum disulfide," *Nano letters*, vol. 17, no. 4, pp. 2342–2348, 2017. Publisher: ACS Publications.

[67] G. Eda, H. Yamaguchi, D. Voiry, T. Fujita, M. Chen, and M. Chhowalla, "Photoluminescence from chemically exfoliated MoS_2," *Nano letters*, vol. 11, no. 12, pp. 5111–5116, 2011. Publisher: ACS Publications.

[68] P. Joensen, R. Frindt, and S. R. Morrison, "Single-layer mos_2," *Materials research bulletin*, vol. 21, no. 4, pp. 457–461, 1986. Publisher: Elsevier.

[69] J. Zheng, H. Zhang, S. Dong, Y. Liu, C. Tai Nai, H. Suk Shin, H. Young Jeong, B. Liu, and K. Ping Loh, "High yield exfoliation of two-dimensional chalcogenides using sodium naphthalenide," *Nature communications*, vol. 5, no. 1, p. 2995, 2014. Publisher: Nature Publishing Group UK London.

[70] J. I. Paredes, J. M. Munuera, S. Villar-Rodil, L. Guardia, M. Ayan-Varela, A. Pagán, S. D. Aznar-Cervantes, J. L. Cenis, A. Martínez-Alonso, and J. M. Tascón, "Impact of covalent functionalization on the aqueous processability, catalytic activity, and biocompatibility of chemically exfoliated MoS_2 nanosheets," *ACS applied materials & interfaces*, vol. 8, no. 41, pp. 27974–27986, 2016. Publisher: ACS Publications.

[71] D. Voiry, A. Goswami, R. Kappera, C. d. C. C. e. Silva, D. Kaplan, T. Fujita, M. Chen, T. Asefa, and M. Chhowalla, "Covalent functionalization of monolayered transition metal dichalcogenides by phase engineering," *Nature chemistry*, vol. 7, no. 1, pp. 45–49, 2015. Publisher: Nature Publishing Group UK London.

[72] J. Heising and M. G. Kanatzidis, "Exfoliated and restacked MoS_2 and WS_2: Ionic or neutral species? Encapsulation and ordering of hard electropositive cations," *Journal of the American Chemical Society*, vol. 121, no. 50, pp. 11720–11732, 1999. Publisher: ACS Publications.

[73] G. Socrates, *Infrared and Raman characteristic group frequencies: tables and charts*. John Wiley & Sons, 2004.

[74] Y. Tao, X. Xie, W. Lv, D.-M. Tang, D. Kong, Z. Huang, H. Nishihara, T. Ishii, B. Li, D. Golberg, and others, "Towards ultrahigh volumetric capacitance: graphene derived highly dense but porous carbons for supercapacitors," *Scientific reports*, vol. 3, no. 1, p. 2975, 2013. Publisher: Nature Publishing Group UK London.

[75] A. Freytag, S. Sánchez-Paradinas, S. Naskar, N. Wendt, M. Colombo, G. Pugliese, J. Poppe, C. Demirci, I. Kretschmer, D. W. Bahnemann, and others, "Versatile aerogel fabrication by freezing and subsequent freeze-drying of colloidal nanoparticle solutions," *Angewandte Chemie International Edition*, vol. 55, no. 3, pp. 1200–1203, 2016. Publisher: Wiley Online Library.

[76] S. Ye, J. Feng, and P. Wu, "Highly elastic graphene oxide–epoxy composite aerogels via simple freeze-drying and subsequent routine curing," *Journal of Materials Chemistry A*, vol. 1, no. 10, pp. 3495–3502, 2013. Publisher: Royal Society of Chemistry.

[77] W. Wang, J. Motuzas, X. S. Zhao, and J. C. Diniz da Costa, "Improved CO2 sorption in freeze-dried amine functionalized mesoporous silica sorbent," *Industrial & Engineering Chemistry Research*, vol. 57, no. 16, pp. 5653–5660, 2018. Publisher: ACS Publications.

[78] W. Zhang, L. Zhang, H. Zhao, B. Li, and H. Ma, "A two-dimensional cationic covalent organic framework membrane for selective molecular sieving," *Journal of Materials Chemistry A*, vol. 6, no. 27, pp. 13331–13339, 2018. Publisher: Royal Society of Chemistry.

[79] I. Gadwal, G. Sheng, R. L. Thankamony, Y. Liu, H. Li, and Z. Lai, "Synthesis of sub-10 nm two-dimensional covalent organic thin film with sharp molecular sieving nanofiltration," *ACS applied materials & interfaces*, vol. 10, no. 15, pp. 12295–12299, 2018. Publisher: ACS Publications.

[80] Y. Marcus, "Ionic radii in aqueous solutions," *Chemical Reviews*, vol. 88, pp. 1475–1498, Dec. 1988. Publisher: American Chemical Society.

[81] A. Akbari, P. Sheath, S. T. Martin, D. B. Shinde, M. Shaibani, P. C. Banerjee, R. Tkacz, D. Bhattacharyya, and M. Majumder, "Large-area graphene-based nanofiltration membranes by shear alignment of discotic nematic liquid crystals of graphene oxide," *Nature communications*, vol. 7, no. 1, p. 10891, 2016. Publisher: Nature Publishing Group UK London.

[82] Y. Han, Y. Jiang, and C. Gao, "High-flux graphene oxide nanofiltration membrane intercalated by carbon nanotubes," *ACS applied materials & interfaces*, vol. 7, no. 15, pp. 8147–8155, 2015. Publisher: ACS Publications.

[83] R. Han and P. Wu, "High-performance graphene oxide nanofiltration membrane with continuous nanochannels prepared by the in situ oxidation of MXene," *Journal of materials chemistry A*, vol. 7, no. 11, pp. 6475–6481, 2019. Publisher: Royal Society of Chemistry.

[84] A. Goswami, A. Acharya, and A. Pandey, "Study of self-diffusion of monovalent and divalent cations in Nafion-117 ion-exchange membrane," *The Journal of Physical Chemistry B*, vol. 105, no. 38, pp. 9196–9201, 2001. Publisher: ACS Publications.

[85] G. Yan, M. Wang, G. T. Hill, S. Zou, and C. Liu, "Defining the challenges of Li extraction with olivine host: The roles of competitor and spectator ions," *Proceedings of the National Academy of Sciences*, vol. 119, no. 31, p. e2200751119, 2022. _eprint: https://www.pnas.org/doi/pdf/10.1073/pnas.2200751119.

[86] J. N. Israelachvili and P. M. McGuiggan, "Forces between surfaces in liquids," *Science*, vol. 241, no. 4867, pp. 795–800, 1988. Publisher: American Association for the Advancement of Science.

[87] A. Wallqvist and B. Berne, "Computer simulation of hydrophobic hydration forces on stacked plates at short range," *The Journal of Physical Chemistry*, vol. 99, no. 9, pp. 2893–2899, 1995. Publisher: ACS Publications.

[88] M. Chávez-Páez, K. Van Workum, L. De Pablo, and J. J. de Pablo, "Monte Carlo simulations of Wyoming sodium montmorillonite hydrates," *The Journal of chemical physics*, vol. 114, no. 3, pp. 1405–1413, 2001. Publisher: American Institute of Physics.

[89] W. Li, W. Wu, and Z. Li, "Controlling interlayer spacing of graphene oxide membranes by external pressure regulation," *Acs Nano*, vol. 12, no. 9, pp. 9309–9317, 2018. Publisher: ACS Publications.

[90] M. Zhang, K. Guan, Y. Ji, G. Liu, W. Jin, and N. Xu, "Controllable ion transport by surface-charged graphene oxide membrane," *Nature communications*, vol. 10, no. 1, p. 1253, 2019. Publisher: Nature Publishing Group UK London.

[91] J. Irving and J. G. Kirkwood, "The statistical mechanical theory of transport processes. IV. The equations of hydrodynamics," *The Journal of chemical physics*, vol. 18, no. 6, pp. 817–829, 1950. Publisher: American Institute of Physics.

[92] W. C. Swope, H. C. Andersen, P. H. Berens, and K. R. Wilson, "A computer simulation method for the calculation of equilibrium constants for the formation of physical clusters of molecules: Application to small water clusters," *The Journal of chemical physics*, vol. 76, no. 1, pp. 637–649, 1982. Publisher: American Institute of Physics.

[93] D. K. Mahalingam, S. Wang, and S. P. Nunes, "Graphene oxide liquid crystal membranes in protic ionic liquid for nanofiltration," *ACS Applied Nano Materials*, vol. 1, no. 9, pp. 4661–4670, 2018. Publisher: ACS Publications.

[94] J. D. Weeks, D. Chandler, and H. C. Andersen, "Role of repulsive forces in determining the equilibrium structure of simple liquids," *The Journal of chemical physics*, vol. 54, no. 12, pp. 5237–5247, 1971. Publisher: American Institute of Physics.

[95] H. J. Berendsen, J. R. Grigera, and T. P. Straatsma, "The missing term in effective pair potentials," *Journal of Physical Chemistry*, vol. 91, no. 24, pp. 6269–6271, 1987. Publisher: ACS Publications.

[96] J.-P. Ryckaert, G. Ciccotti, and H. J. Berendsen, "Numerical integration of the cartesian equations of motion of a system with constraints: molecular dynamics of n-alkanes," *Journal of Computational Physics*, vol. 23, pp. 327–341, Mar. 1977.

[97] B. Luan and R. Zhou, "Wettability and friction of water on a MoS_2 nanosheet," *Applied Physics Letters*, vol. 108, no. 13, 2016. Publisher: AIP Publishing.

[98] S. L. Mayo, B. D. Olafson, and W. A. Goddard, "DREIDING: a generic force field for molecular simulations," *Journal of Physical chemistry*, vol. 94, no. 26, pp. 8897–8909, 1990. Publisher: ACS Publications.

[99] I. S. Joung and T. E. Cheatham III, "Determination of alkali and halide monovalent ion parameters for use in explicitly solvated biomolecular simulations," *The journal of physical chemistry B*, vol. 112, no. 30, pp. 9020–9041, 2008. Publisher: ACS Publications.

[100] D. T. Limmer, C. Merlet, M. Salanne, D. Chandler, P. A. Madden, R. Van Roij, and B. Rotenberg, "Charge fluctuations in nanoscale capacitors," *Physical review letters*, vol. 111, no. 10, p. 106102, 2013. Publisher: APS.

[101] S. Nosé, "A molecular dynamics method for simulations in the canonical ensemble," *Molecular physics*, vol. 52, no. 2, pp. 255–268, 1984. Publisher: Taylor & Francis.

[102] W. G. Hoover, "Canonical dynamics: Equilibrium phase-space distributions," *Physical review A*, vol. 31, no. 3, p. 1695, 1985. Publisher: APS.

[103] W. Shinoda, M. Shiga, and M. Mikami, "Rapid estimation of elastic constants by molecular dynamics simulation under constant stress," *Physical Review B*, vol. 69, no. 13, p. 134103, 2004. Publisher: APS.

[104] G. J. Martyna, D. J. Tobias, and M. L. Klein, "Constant pressure molecular dynamics algorithms," *The Journal of chemical physics*, vol. 101, no. 5, pp. 4177–4189, 1994. Publisher: American Institute of Physics.

[105] M. Parrinello and A. Rahman, "Polymorphic transitions in single crystals: A new molecular dynamics method," *Journal of Applied physics*, vol. 52, no. 12, pp. 7182–7190, 1981. Publisher: American Institute of Physics.

[106] S. Plimpton, "Fast parallel algorithms for short-range molecular dynamics," *Journal of Computational Physics*, vol. 117, pp. 1–19, Mar. 1995.

[107] W. Humphrey, A. Dalke, and K. Schulten, "VMD: visual molecular dynamics," *Journal of molecular graphics*, vol. 14, no. 1, pp. 33–38, 1996. Publisher: Elsevier.

[108] T. Plachetka, "POV Ray: persistence of vision parallel raytracer," in *Proc. of Spring Conf. on Computer Graphics, Budmerice, Slovakia*, vol. 123, p. 129, 1998.

[109] G. Fiorin, M. L. Klein, and J. Hénin, "Using collective variables to drive molecular dynamics simulations," *Molecular Physics*, vol. 111, no. 22-23, pp. 3345–3362, 2013. Publisher: Taylor & Francis.

[110] A. Grossfield, "WHAM: the weighted histogram analysis method, version 2.0. 9," *Available at membrane. urmc. rochester. edu/content/wham. Accessed November*, vol. 15, p. 2013, 2013.

[111] S. Kumar, J. M. Rosenberg, D. Bouzida, R. H. Swendsen, and P. A. Kollman, "The weighted histogram analysis method for free-energy calculations on biomolecules. I. The method," *Journal of computational chemistry*, vol. 13, no. 8, pp. 1011–1021, 1992. Publisher: Wiley Online Library.

[112] B. Roux, "The calculation of the potential of mean force using computer simulations," *Computer physics communications*, vol. 91, no. 1-3, pp. 275–282, 1995. Publisher: Elsevier.

[113] L. Bocquet and E. Charlaix, "Nanofluidics, from bulk to interfaces," *Chemical Society Reviews*, vol. 39, no. 3, pp. 1073–1095, 2010. Publisher: The Royal Society of Chemistry.

[114] L. Bocquet, "Nanofluidics coming of age," *Nature Materials*, vol. 19, pp. 254–256, Mar. 2020.

[115] N. Kavokine, R. R. Netz, and L. Bocquet, "Fluids at the nanoscale: from continuum to subcontinuum transport," *Annual Review of Fluid Mechanics*, vol. 53, pp. 377–410, Jan. 2021. Publisher: Annual Reviews.

[116] L. Mogg, G.-P. Hao, S. Zhang, C. Bacaksiz, Y.-C. Zou, S. J. Haigh, F. M. Peeters, A. K. Geim, and M. Lozada-Hidalgo, "Atomically thin micas as proton-conducting membranes," *Nature Nanotechnology*, vol. 14, pp. 962–966, Oct. 2019.

[117] J. Cai, E. Griffin, V. H. Guarochico-Moreira, D. Barry, B. Xin, M. Yagmurcukardes, S. Zhang, A. K. Geim, F. M. Peeters, and M. Lozada-Hidalgo, "Wien effect in interfacial water dissociation through proton-permeable graphene electrodes," *Nature Communications*, vol. 13, p. 5776, Oct. 2022.

[118] C. Cheng, S. A. Iyengar, and R. Karnik, "Molecular size-dependent subcontinuum solvent permeation and ultrafast nanofiltration across nanoporous graphene membranes," *Nature Nanotechnology*, vol. 16, pp. 989–995, Sept. 2021.

[119] A. Razmjou, M. Asadnia, E. Hosseini, A. Habibnejad Korayem, and V. Chen, "Design principles of ion selective nanostructured membranes for the extraction of lithium ions," *Nature Communications*, vol. 10, p. 5793, Dec. 2019.

[120] Z. Wang, Q. Tu, A. Sim, J. Yu, Y. Duan, S. Poon, B. Liu, Q. Han, J. J. Urban, D. Sedlak, and B. Mi, "Superselective removal of lead from water by two-dimensional MoS_2 nanosheets and layer-stacked membranes," *Environmental Science & Technology*, vol. 54, pp. 12602–12611, Oct. 2020. Publisher: American Chemical Society.

[121] H. Zhang, X. Li, J. Hou, L. Jiang, and H. Wang, "Angstrom-scale ion channels towards single-ion selectivity," *Chem. Soc. Rev.*, vol. 51, no. 6, pp. 2224–2254, 2022. Publisher: The Royal Society of Chemistry.

[122] Y. Zhao, T. Tong, X. Wang, S. Lin, E. M. Reid, and Y. Chen, "Differentiating solutes with precise nanofiltration for next generation environmental separations: a review," *Environmental Science & Technology*, vol. 55, pp. 1359–1376, Feb. 2021. Publisher: American Chemical Society.

[123] R. Epsztein, R. M. DuChanois, C. L. Ritt, A. Noy, and M. Elimelech, "Towards single-species selectivity of membranes with subnanometre pores," *Nature Nanotechnology*, vol. 15, pp. 426–436, June 2020.

[124] Y. Zhang, D. Chen, W. He, J. Tan, Y. Yang, and Q. Yuan, "Bioinspired solid-state ion nanochannels: insight from channel fabrication and ion transport," *Advanced Materials Technologies*, vol. 8, p. 2202014, June 2023. Publisher: John Wiley & Sons, Ltd.

[125] F. Zarei, R. M. Moattari, S. Rajabzadeh, M. Bagheri, A. Taghizadeh, T. Mohammadi, and H. Matsuyama, "Preparation of thin film composite nano-filtration membranes for brackish water softening based on the reaction between functionalized UF membranes and polyethyleneimine," *Journal of Membrane Science*, vol. 588, p. 117207, Oct. 2019.

[126] Y. Zhao, X. Tong, and Y. Chen, "Fit-for-purpose design of nanofiltration membranes for simultaneous nutrient recovery and micropollutant removal," *Environmental Science & Technology*, vol. 55, pp. 3352–3361, Mar. 2021. Publisher: American Chemical Society.

[127] R. M. DuChanois, C. J. Porter, C. Violet, R. Verduzco, and M. Elimelech, "Membrane materials for selective ion separations at the water–energy nexus," *Advanced Materials*, vol. 33, p. 2101312, Sept. 2021. Publisher: John Wiley & Sons, Ltd.

[128] P. Z. Sun, M. Yagmurcukardes, R. Zhang, W. J. Kuang, M. Lozada-Hidalgo, B. L. Liu, H.-M. Cheng, F. C. Wang, F. M. Peeters, I. V. Grigorieva, and A. K. Geim, "Exponentially selective molecular sieving through angstrom pores," *Nature Communications*, vol. 12, p. 7170, Dec. 2021.

[129] M. Macha, S. Marion, M. Tripathi, M. Thakur, M. Lihter, A. Kis, A. Smolyanitsky, and A. Radenovic, "High-throughput nanopore fabrication and classification using FIB irradiation and automated pore edge analysis," 2022.

[130] J. P. Thiruraman, P. Masih Das, and M. Drndić, "Irradiation of transition metal dichalcogenides using a focused ion beam: controlled single-atom defect creation," *Advanced Functional Materials*, vol. 29, p. 1904668, Dec. 2019. Publisher: John Wiley & Sons, Ltd.

[131] S. P. Koenig, L. Wang, J. Pellegrino, and J. S. Bunch, "Selective molecular sieving through porous graphene," *Nature Nanotechnology*, vol. 7, pp. 728–732, Nov. 2012.

[132] E. Griffin, L. Mogg, G.-P. Hao, G. Kalon, C. Bacaksiz, G. Lopez-Polin, T. Zhou, V. Guarochico, J. Cai, C. Neumann, A. Winter, M. Mohn, J. H. Lee, J. Lin, U. Kaiser, I. V. Grigorieva, K. Suenaga, B. Özyilmaz, H.-M. Cheng, W. Ren, A. Turchanin, F. M. Peeters, A. K. Geim, and M. Lozada-Hidalgo, "Proton and Li-ion permeation through graphene with eight-atom-ring defects," *ACS Nano*, vol. 14, pp. 7280–7286, June 2020. Publisher: American Chemical Society.

[133] P. R. Kidambi, G. D. Nguyen, S. Zhang, Q. Chen, J. Kong, J. Warner, A.-P. Li, and R. Karnik, "Facile fabrication of large-area atomically thin membranes by direct synthesis of graphene with nanoscale porosity," *Advanced Materials*, vol. 30, p. 1804977, Dec. 2018. Publisher: John Wiley & Sons, Ltd.

[134] S. Marion, M. Macha, S. J. Davis, A. Chernev, and A. Radenovic, "Wetting of nanopores probed with pressure," *Physical Chemistry Chemical Physics*, vol. 23, no. 8, pp. 4975–4987, 2021. Publisher: The Royal Society of Chemistry.

[135] L. Cantley, J. L. Swett, D. Lloyd, D. A. Cullen, K. Zhou, P. V. Bedworth, S. Heise, A. J. Rondinone, Z. Xu, S. Sinton, and J. S. Bunch, "Voltage gated inter-cation selective ion channels from graphene nanopores," *Nanoscale*, vol. 11, no. 20, pp. 9856–9861, 2019. Publisher: The Royal Society of Chemistry.

[136] M. Velický, "Electrolyte versus Dielectric Gating of Two-Dimensional Materials," *The Journal of Physical Chemistry C*, vol. 125, pp. 21803–21809, Oct. 2021. Publisher: American Chemical Society.

[137] Y. He, P. Tang, Z. Hu, Q. He, C. Zhu, L. Wang, Q. Zeng, P. Golani, G. Gao, W. Fu, Z. Huang, C. Gao, J. Xia, X. Wang, X. Wang, C. Zhu, Q. M. Ramasse, A. Zhang, B. An, Y. Zhang, S. Martí-Sánchez, J. R. Morante, L. Wang, B. K. Tay, B. I. Yakobson, A. Trampert, H. Zhang, M. Wu, Q. J. Wang, J. Arbiol, and Z. Liu, "Engineering grain boundaries at the 2D limit for the hydrogen evolution reaction," *Nature Communications*, vol. 11, p. 57, Jan. 2020.

[138] Y. Ouyang, C. Ling, Q. Chen, Z. Wang, L. Shi, and J. Wang, "Activating inert basal planes of MoS_2 for hydrogen evolution reaction through the formation of different intrinsic defects," *Chemistry of Materials*, vol. 28, pp. 4390–4396, June 2016. Publisher: American Chemical Society.

[139] A. Castellanos-Gomez, M. Buscema, R. Molenaar, V. Singh, L. Janssen, H. S. J. v. d. Zant, and G. A. Steele, "Deterministic transfer of two-dimensional materials by all-dry viscoelastic stamping," *2D Materials*, vol. 1, p. 011002, Apr. 2014. Publisher: IOP Publishing.

[140] Y. Jung, J. Shen, Y. Liu, J. M. Woods, Y. Sun, and J. J. Cha, "Metal seed layer thickness-induced transition from vertical to horizontal growth of MoS_2 and WS_2,"

Nano Letters, vol. 14, pp. 6842–6849, Dec. 2014. Publisher: American Chemical Society.

[141] D. Kong, H. Wang, J. J. Cha, M. Pasta, K. J. Koski, J. Yao, and Y. Cui, "Synthesis of MoS_2 and $MoSe_2$ films with vertically aligned layers," *Nano Letters*, vol. 13, pp. 1341–1347, Mar. 2013. Publisher: American Chemical Society.

[142] C. Stern, S. Grinvald, M. Kirshner, O. Sinai, M. Oksman, H. Alon, O. E. Meiron, M. Bar-Sadan, L. Houben, and D. Naveh, "growth mechanisms and electronic properties of vertically aligned MoS_2," *Scientific Reports*, vol. 8, p. 16480, Nov. 2018.

[143] H. Qiu, T. Xu, Z. Wang, W. Ren, H. Nan, Z. Ni, Q. Chen, S. Yuan, F. Miao, F. Song, G. Long, Y. Shi, L. Sun, J. Wang, and X. Wang, "Hopping transport through defect-induced localized states in molybdenum disulphide," *Nature Communications*, vol. 4, p. 2642, Oct. 2013.

[144] S. Hu, M. Lozada-Hidalgo, F. C. Wang, A. Mishchenko, F. Schedin, R. R. Nair, E. W. Hill, D. W. Boukhvalov, M. I. Katsnelson, R. A. W. Dryfe, I. V. Grigorieva, H. A. Wu, and A. K. Geim, "Proton transport through one-atom-thick crystals," *Nature*, vol. 516, pp. 227–230, Dec. 2014.

[145] J. Feng, K. Liu, M. Graf, M. Lihter, R. D. Bulushev, D. Dumcenco, D. T. L. Alexander, D. Krasnozhon, T. Vuletic, A. Kis, and A. Radenovic, "Electrochemical reaction in single layer MoS_2: nanopores opened atom by atom," *Nano Letters*, vol. 15, pp. 3431–3438, May 2015. Publisher: American Chemical Society.

[146] J. P. Thiruraman, K. Fujisawa, G. Danda, P. M. Das, T. Zhang, A. Bolotsky, N. Perea-López, A. Nicolaï, P. Senet, M. Terrones, and M. Drndić, "Angstrom-size defect creation and ionic transport through pores in single-layer MoS_2," *Nano Letters*, vol. 18, pp. 1651–1659, Mar. 2018. Publisher: American Chemical Society.

[147] J. P. de Souza, C.-M. Chow, R. Karnik, and M. Z. Bazant, "Nonlinear ion transport mediated by induced charge in ultrathin nanoporous membranes," *Phys. Rev. E*, vol. 104, p. 044802, Oct. 2021. Publisher: American Physical Society.

[148] J. Feng, K. Liu, R. D. Bulushev, S. Khlybov, D. Dumcenco, A. Kis, and A. Radenovic, "Identification of single nucleotides in MoS_2 nanopores," *Nature Nanotechnology*, vol. 10, pp. 1070–1076, Dec. 2015.

[149] X. Qiu, H. Yu, M. Karunakaran, N. Pradeep, S. P. Nunes, and K.-V. Peinemann, "Selective separation of similarly sized proteins with tunable nanoporous block copolymer membranes," *ACS Nano*, vol. 7, pp. 768–776, Jan. 2013. Publisher: American Chemical Society.

[150] D. Nečas and P. Klapetek, "Gwyddion: an open-source software for SPM data analysis," *Open Physics*, vol. 10, no. 1, pp. 181–188, 2012.

[151] A. Gadaleta, C. Sempere, S. Gravelle, A. Siria, R. Fulcrand, C. Ybert, and L. Bocquet, "Sub-additive ionic transport across arrays of solid-state nanopores," *Physics of Fluids*, vol. 26, p. 012005, Jan. 2014. Publisher: American Institute of Physics.

[152] W. Chen, X. Gui, B. Liang, M. Liu, Z. Lin, Y. Zhu, and Z. Tang, "Controllable Fabrication of Large-Area Wrinkled Graphene on a Solution Surface," *ACS Applied Materials & Interfaces*, vol. 8, pp. 10977–10984, May 2016. Publisher: American Chemical Society.

[153] C. Lee, L. Joly, A. Siria, A.-L. Biance, R. Fulcrand, and L. Bocquet, "Large apparent electric size of solid-state nanopores due to spatially extended surface conduction," *Nano Letters*, vol. 12, pp. 4037–4044, Aug. 2012. Publisher: American Chemical Society.

[154] M. Graf, M. Lihter, M. Thakur, V. Georgiou, J. Topolancik, B. R. Ilic, K. Liu, J. Feng, Y. Astier, and A. Radenovic, "Fabrication and practical applications of molybdenum disulfide nanopores," *Nature Protocols*, vol. 14, pp. 1130–1168, Apr. 2019.

[155] R. C. Rollings, A. T. Kuan, and J. A. Golovchenko, "Ion selectivity of graphene nanopores," *Nature Communications*, vol. 7, p. 11408, Apr. 2016.

[156] S. Su, Y. Zhang, S. Peng, L. Guo, Y. Liu, E. Fu, H. Yao, J. Du, G. Du, and J. Xue, "Multifunctional graphene heterogeneous nanochannel with voltage-tunable ion selectivity," *Nature Communications*, vol. 13, p. 4894, Aug. 2022.

[157] J. Feng, K. Liu, M. Graf, D. Dumcenco, A. Kis, M. Di Ventra, and A. Radenovic, "Observation of ionic Coulomb blockade in nanopores," *Nature Materials*, vol. 15, pp. 850–855, Aug. 2016.

[158] J. W. Perram and P. J. Stiles, "On the nature of liquid junction and membrane potentials," *Physical Chemistry Chemical Physics*, vol. 8, no. 36, pp. 4200–4213, 2006. Publisher: The Royal Society of Chemistry.

[159] T. Yagasaki, M. Matsumoto, and H. Tanaka, "Lennard-Jones Parameters Determined to Reproduce the Solubility of NaCl and KCl in SPC/E, TIP3P, and TIP4P/2005 Water," *Journal of Chemical Theory and Computation*, vol. 16, pp. 2460–2473, Apr. 2020. Publisher: American Chemical Society.

[160] C. W. Bock, A. Kaufman, and J. P. Glusker, "Coordination of water to magnesium cations," *Inorganic Chemistry*, vol. 33, pp. 419–427, Feb. 1994. Publisher: American Chemical Society.

[161] I. N. Tsimpanogiannis, O. A. Moultos, L. F. M. Franco, M. B. d. M. Spera, M. Erdős, and I. G. Economou, "Self-diffusion coefficient of bulk and confined water: a critical review of classical molecular simulation studies," *Molecular Simulation*, vol. 45, pp. 425–453, Mar. 2019. Publisher: Taylor & Francis.

[162] J. P. Thiruraman, P. Masih Das, and M. Drndić, "Stochastic ionic transport in single atomic zero-dimensional pores," *ACS Nano*, vol. 14, pp. 11831–11845, Sept. 2020. Publisher: American Chemical Society.

[163] N. Kavokine, S. Marbach, A. Siria, and L. Bocquet, "Ionic Coulomb blockade as a fractional Wien effect," *Nature Nanotechnology*, vol. 14, pp. 573–578, June 2019.

[164] S. Mamatkulov, M. Fyta, and R. R. Netz, "Force fields for divalent cations based on single-ion and ion-pair properties," *The Journal of Chemical Physics*, vol. 138, p. 024505, Jan. 2013. Publisher: American Institute of Physics.

[165] L. Martínez, R. Andrade, E. G. Birgin, and J. M. Martínez, "PACKMOL: A package for building initial configurations for molecular dynamics simulations," *Journal of Computational Chemistry*, vol. 30, pp. 2157–2164, Oct. 2009. Publisher: John Wiley & Sons, Ltd.

[166] A. Kohlmeyer and J. Vermaas, "TopoTools: release 1.9," 2022.

[167] N. Michaud-Agrawal, E. J. Denning, T. B. Woolf, and O. Beckstein, "MDAnalysis: A toolkit for the analysis of molecular dynamics simulations," *Journal of Computational Chemistry*, vol. 32, pp. 2319–2327, July 2011. Publisher: John Wiley & Sons, Ltd.